

10-01-02

Need official stamp

MEMORANDUM TO: John A. Zwolinski, Director  
Division of Licensing and Project Management  
Office of Nuclear Reactor Regulation

FROM: Michael Mayfield, Director  
Division of Engineering  
Office of Nuclear Reactor Research

SUBJECT: STRUCTURAL ANALYSIS OF THE RUPTURE CAPACITY OF THE  
EXPOSED CLADDING AT DAVIS BESSE

Attached are three reports detailing our assessment of the rupture capacity of the exposed cladding and wastage area discovered at the Davis Besse nuclear power plant in February 2002:

- Kirk, M.T., "Structural Analysis of the Rupture Capacity of the 308 Stainless Steel Cladding Remaining over the Wastage Cavity in the Head of the Davis Besse Reactor Pressure Vessel."
- Williams, P.T. and Bass, B.R., "Stochastic Failure Model of the Davis Besse RPV Head."
- Williams, P.T. and Bass, B.R., "Analysis of the Davis Besse RPV Head Wastage Area and Cavity."

The second and third reports were prepared by our contractors at the Oak Ridge National Laboratory; they contain a detailed description of all the finite element analysis that we have performed in support of NRR's assessment of Davis Besse. The first report was prepared by a member of my staff; it summarizes the results of the two ORNL reports, details all of the assumptions made in these analysis, and provides our assessment of the results. Collectively these documents satisfy NRR User Need NRR-2002-018 entitled "Complete final assessment of analysis relevant to Davis Besse design and safety margins" and the associated RES Operating Plan Milestone 1A1AACL. The calculations were performed prior to discovery of cracking in the cladding.

The following are the principle results for as found condition:

- The median failure pressure of cladding in as found condition is expected to be between 5700 and 7300 psi depending on the thickness of the cladding covering the wastage area. Recent dial gage measurements of the cladding thickness suggest that the expected median failure pressure is closer to the upper end of this range.
- Failure of the clad membrane at pressures up to the set-point pressure represents an extremely unlikely event. Failure probabilities are estimated to be in the  $10^{-7}$  to  $10^{-8}$  range.

Had the wastage condition not been discovered on February 16, 2002 and continued to grow, we (conservatively) estimate that between 4½ and 7½ more inches of corrosion wastage of the

Information in this record was deleted  
in accordance with the Freedom of Information  
Act, etc. 2003-0017  
EOIA-

J-17

RPV steel in all directions would have been needed to rupture the cladding at pressures between the operating pressure and the set point pressure. Available information on the rate of boric acid corrosion of structural steel taken from the literature suggests that these conditions could have been achieved within a year of continued operation. However, it should be noted that this estimate of the additional corrosion and time needed to produce cladding rupture at pressures between the operating pressure and the set point pressure is highly uncertain. Our estimates are intended to bound conservatively (i.e. be lower than) the conditions needed to actually rupture the cladding.

In our on-going research we continue to further refine these analysis. Our current focus is an assessment of the effect of cracks on the estimated rupture pressures presented herein. This study includes both analytical predictions as well as burst-disk experiments conducted on samples of 308 stainless steel cladding. This work will include more thorough investigation of uncertainties that effect the rupture pressure and will use information generated in on-going investigation of the materials from Davis-Besse being conducted at Framatome and at the Argonne National Laboratory.

I would appreciate any comments or suggestions you would care to offer regarding these reports. Should you require additional information, please contact Mark Kirk ([MTK@nrc.gov](mailto:MTK@nrc.gov)) of my staff on 415-6015.

Attachments: As stated

cc: R. Bass, ORNL  
P. Williams, ORNL

Distribution:

W. Cullen	S. Long	G. DeMoss	J. Strosnider/A. Thadani
W. Norris	M. Johnson	W. Bateman	D. Jackson
A. Hiser	R. Barrett	MEB r/f	DET r/f

DOCUMENT NAME: g:\kirk\Davis Besse Transmittal Letter

OAR In ADAMS? (Y or N) Y ADAMS ACCESSION NO.: \_\_\_\_\_ TEMPLATE NO. RES- 006  
Publicly Available? (Y or N) Y DATE OF RELEASE TO PUBLIC \_\_\_\_\_ SENSITIVE? \_\_\_\_\_

To receive a copy of this document, indicate in the box: "C" = Copy without enclosures "E" = Copy with enclosures "N" = No copy

\* See previous Concurrences

OFFICE	MEB/DET	MEB/DET	MEB/DET	RES/DET
NAME	M.T. Kirk*	D.A. Jackson*	N. C. Chokshi	M. Mayfield
DATE	10/ /02	10/ /02	10/ /02	10/ /02

# Structural Analysis of the Rupture Capacity of the 308 Stainless Steel Cladding Remaining over the Wastage Cavity in the Head of the Davis Besse Reactor Pressure Vessel

Mark Kirk

This document, along with the two attached reports, collectively satisfy RES OpPlan Milestone 1A1AACL and NRR User Need NRR-2002-018 entitled "*Complete Final Assessment of Analysis Relevant to Davis Besse Design and Safety Margins*"

30<sup>th</sup> September 2002

## Executive Summary

Pursuant to the licensee's commitments to NRC Bulletin 2001-01, the Davis-Besse Nuclear Power Station began a refueling outage on February 16, 2002, that included inspection of the vessel head penetrations with an emphasis on the inspection of control rod drive mechanism (CRDM) nozzles. These inspections identified axial indications in three CRDM nozzles that were experiencing pressure-boundary leakage. Upon completing boric acid removal on March 7, 2002, the licensee conducted a visual examination of the area and identified a cavity in the RPV head on the downhill side of CRDM Nozzle 3. Followup characterization by ultrasonic testing (UT) indicated wastage of the low alloy steel RPV head material adjacent to the nozzle. The wastage area was found to extend approximately 5 inches downhill of the RPV head from the penetration for CRDM Nozzle 3, with a width of approximately 4 to 5 inches at its widest part. At the time of shutdown for the February 16, 2002 refueling outage only the stainless steel cladding maintained the pressure boundary of the primary reactor circuit over an area of approximately 20 square inches.

In support of an assessment by Office of Nuclear Reactor Regulation (NRR) of the significance of this cavity to the structural integrity of the reactor pressure vessel, the Office of Nuclear Reactor Research (RES) was tasked to perform structural analysis of the head of the RPV at Davis Besse. In this report we summarize the results of various finite element models of the corrosion wastage discovered at the Davis Besse nuclear power plant on February 16, 2002. These analyses have focused on estimating the rupture capacity of the cladding covering the wastage cavity that is no longer backed by reactor pressure vessel steel. The information presented herein supports the following conclusions concerning the cavity as it existed on February 16, 2002 when Davis Besse was shut down:

- The median failure pressure of this cladding in this condition is expected to be between 5700 and 7300 psi depending on the thickness of the cladding covering the wastage area. Recent dial gage measurements of the cladding thickness suggest that the expected median failure pressure is closer to the upper end of this range.
- Failure of the clad membrane in this condition at pressures up to the set-point pressure represents an extremely unlikely event. Failure probabilities are estimated to be in the  $10^{-7}$  to  $10^{-8}$  range.

Had the wastage condition not been discovered on February 16, 2002 and continued to grow, we (conservatively) estimate that between 4½ and 7½ more inches of corrosion wastage of the RPV steel in all directions would have been needed to rupture the cladding at pressures between the operating pressure and the set point pressure.

In our on-going research we continue to further refine these analysis. Our current focus is an assessment of the effect of cracks on the estimated rupture pressures presented herein. This study includes both analytical predictions as well as burst-disk experiments conducted on samples of 308 stainless steel cladding.

# Table of Contents

	<u>Page</u>
<b><u>Executive Summary</u></b> .....	<b>1-2</b>
<b><u>Table of Contents</u></b> .....	<b>1-3</b>
<b><u>List of Figures</u></b> .....	<b>1-4</b>
<b><u>List of Tables</u></b> .....	<b>1-5</b>
<b><u>1. Background</u></b> .....	<b>6</b>
<b><u>2. Modeling Methodology and Assumptions</u></b> .....	<b>8</b>
2.1 <u>Preliminary Analysis Results, and Modeling Philosophy</u> .....	8
2.2 <u>Finite Element Analysis Model</u> .....	8
2.3 <u>Assumptions</u> .....	9
2.3.1 <u>Assumptions Concerning Variables</u> .....	9
2.3.1.1 <u>Variables Modeled Accurately</u> .....	11
2.3.1.2 <u>Variables Modeled Conservatively</u> .....	12
2.3.1.2.1 <u>Geometric Variables</u> .....	12
2.3.1.2.2 <u>Material Variables</u> .....	14
2.3.1.3 <u>Variables Not Modeled</u> .....	16
2.3.1.3.1 <u>Surface relief of the cladding</u> .....	16
2.3.1.3.2 <u>Thermal gradient across the cladding</u> .....	16
2.3.1.3.3 <u>Residual stresses in the cladding</u> .....	17
2.3.1.3.4 <u>Flaws in the cladding, and cladding toughness properties</u> .....	17
2.3.2 <u>Assumptions Concerning Failure Model</u> .....	18
2.3.3 <u>Summary</u> .....	19
<b><u>3. Analysis Results: Rupture Pressures and Probabilities</u></b> .....	<b>20</b>
3.1 <u>As-Found Condition (Condition at February 16, 2002 Shutdown)</u> .....	20
3.2 <u>Potential Future States</u> .....	20
<b><u>4. Summary and On-Going Work</u></b> .....	<b>25</b>
<b><u>5. References</u></b> .....	<b>26</b>

## List of Figures

	<u>Page</u>
<u>Figure 1.1.</u> <u>Illustration of the location of the wastage cavity in the head of the Davis Besse reactor pressure vessel. ....</u>	7
<u>Figure 1.2.</u> <u>Diagrams and photos of the Davis Besse wastage area at nozzle three: (a) Sketch of thru-thickness extent provided in April 2002 by the licensee [FENOC 4/02], (b) View of the cavity from the outer radius once the Nozzle 3 plug was removed from the head, (c) Close-up view of the "nose" of the wastage cavity, (d) Dental mold of the wastage cavity made by Framatome [FENOC 9/02a]. ....</u>	7
<u>Figure 2.1.</u> <u>Finite element global and submodels of the Davis Besse wastage area. The displacements at the vertical side boundaries of the submodel are driven by the global model. Both models are exposed to the same pressure loading. ....</u>	10
<u>Figure 2.2.</u> <u>Tensile properties adopted for RPV steel (left) and for Alloy 600 (right). ....</u>	11
<u>Figure 2.3.</u> <u>Comparison of the exposed cladding area measured by the dental mold impression taken in September 2002 [FENOC 9/02a] and the representation of the exposed cladding area adopted in the finite element analysis that was based on measurements reported in April 2002 [FENOC 4/02]. ....</u>	13
<u>Figure 2.4.</u> <u>Measurements of cladding thickness based on dial gage measurements reported by FENOC in September 2002 (left: measurement data, right: computer generated contour map) [FENOC 9/02b]. ....</u>	14
<u>Figure 2.5.</u> <u>Comparison of 308 stainless steel tensile data with the stress-strain relationship assumed in the ORNL/NRC finite element model. ....</u>	15
<u>Figure 2.6.</u> <u>Comparison of 308 stainless steel tensile data obtained by testing the cladding material removed from Davis Besse with the stress-strain relationship assumed in the ORNL/NRC finite element model. ....</u>	15
<u>Figure 2.7.</u> <u>Photograph and computer generated representation of the surface relief of the exposed cladding (RCS side) in and around the Nozzle 3 wastage area. ....</u>	16
<u>Figure 2.8.</u> <u>PNNL flaw distribution for welded stainless steel cladding (thick red line). ....</u>	17
<u>Figure 2.9.</u> <u>PNNL flaw distribution scaled to give the expected number of flaws based on the size of the Davis Besse wastage cavity (this scaling assumes that the wastage cavity has ½ m of weld bead, an assumption validated by the data in Figure 2.3). ....</u>	18
<u>Figure 2.10.</u> <u>Cumulative distribution functions for the ratios of burst pressure (BP) measured experimentally by Riccardella to the pressure at numerical instability (<math>P_{NI}</math>) in an ABAQUS finite element analysis. ....</u>	19
<u>Figure 3.1.</u> <u>Growth patterns assumed in the analysis of wastage cavities larger than that which existed at Davis Besse on February 16, 2002. ....</u>	21
<u>Figure 3.2.</u> <u>Summary of the effect of wastage cavity size and shape on rupture capacity of the clad membrane: (a) pressures at numerical instability, <math>P_{NI}</math>, calculated by ABAQUS finite-element submodels of postulated footprints are compared to burst pressures in circular diaphragms predicted by the theory of Chakrabarty and Alexander (1970), and (b) stochastic failure model scaled from the theory of Chakrabarty and Alexander (1970). ....</u>	22
<u>Figure 3.3.</u> <u>Corrosion rate data for steel subjected to a continuously replenished boric acid solution at a temperature near 212°F collected by Cullen [MEB 9/02]. ....</u>	23
<u>Figure 3.4.</u> <u>Estimates of the additional time needed to enlarge the Davis Besse cavity sufficiently so that rupture of the cladding would be expected to occur at or slightly above the operating pressure. ....</u>	24

## List of Tables

	<u>Page</u>
<u>Table 2.1.</u> <u>List of all variables that can effect predicted rupture capacity.</u> .....	9
<u>Table 2.2.</u> <u>Variable classification strategy.</u> .....	9
<u>Table 2.3.</u> <u>Description of how variables that effect predicted rupture capacity were modeled.</u> .....	11
<u>Table 3.1.</u> <u>Cavity sizes needed to produce rupture of the cladding membrane at the operating and set point pressures.</u> .....	23

# 1. Background

Pursuant to the licensee's commitments to NRC Bulletin 2001-01, the Davis-Besse Nuclear Power Station began a refueling outage on February 16, 2002, that included inspection of the vessel head penetrations with an emphasis on the inspection of control rod drive mechanism (CRDM) nozzles. These inspections identified axial indications in three CRDM nozzles that were experiencing pressure-boundary leakage. Upon completing boric acid removal on March 7, 2002, the licensee conducted a visual examination of the area and identified a cavity in the RPV head on the downhill side of CRDM Nozzle 3. Followup characterization by ultrasonic testing (UT) indicated wastage of the low alloy steel RPV head material adjacent to the nozzle. The wastage area was found to extend approximately 5 inches downhill of the RPV head from the penetration for CRDM Nozzle 3, with a width of approximately 4 to 5 inches at its widest part. Figure 1.1 illustrates the location of the cavity in the RPV head while Figure 1.2 provides several views of the wastage cavity itself. At the time of shutdown for the February 16, 2002 refueling outage only the stainless steel cladding maintained the pressure boundary of the primary reactor circuit over an area of approximately 20 square inches.

In support of an assessment by Office of Nuclear Reactor Regulation (NRR) of the significance of this cavity to the structural integrity of the reactor pressure vessel the Office of Nuclear Reactor Research (RES) was tasked to perform structural analysis of the head of the RPV at Davis Besse. These analyses, carried out for RES by the Heavy-Section Steel Technology Program at Oak Ridge National Laboratory, are detailed in the following two reports:

- Williams, P.T. and Bass, B.R., "Stochastic Failure Model of the Davis Besse RPV Head," August 23, 2002, ORNL/NRC/LTR-????.
- Williams, P.T. and Bass, B.R., "Analysis of the Davis Besse RPV Head Wastage Area and Cavity," October ??, 2002, ORNL/NRC/LTR-????.

These analyses include both deterministic and probabilistic assessments of the pressure that can be retained by the cladding in the wastage region. The first report concerns the wastage condition that existed at Davis Besse on February 16, 2002 while the second report concerns failure pressures associated with certain postulated future states that might have existed had operation not stopped on February 16, 2002.

This document provides a summary of the technical findings of both ORNL reports, and uses these findings to provide a bounding assessment of the additional duration over which Davis Besse could have operated before cladding rupture was likely at either the set-point or the operating pressure.

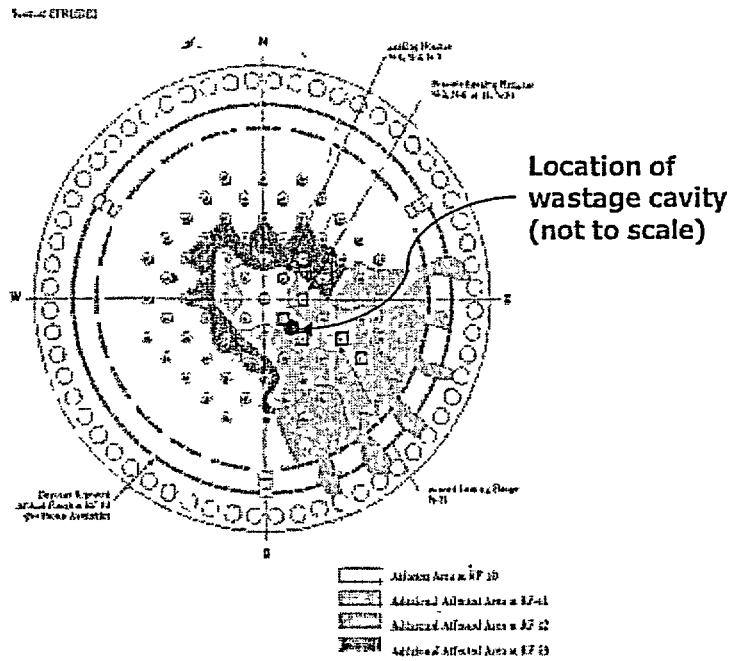


Figure 1.1. Illustration of the location of the wastage cavity in the head of the Davis Besse reactor pressure vessel.

Ex 4

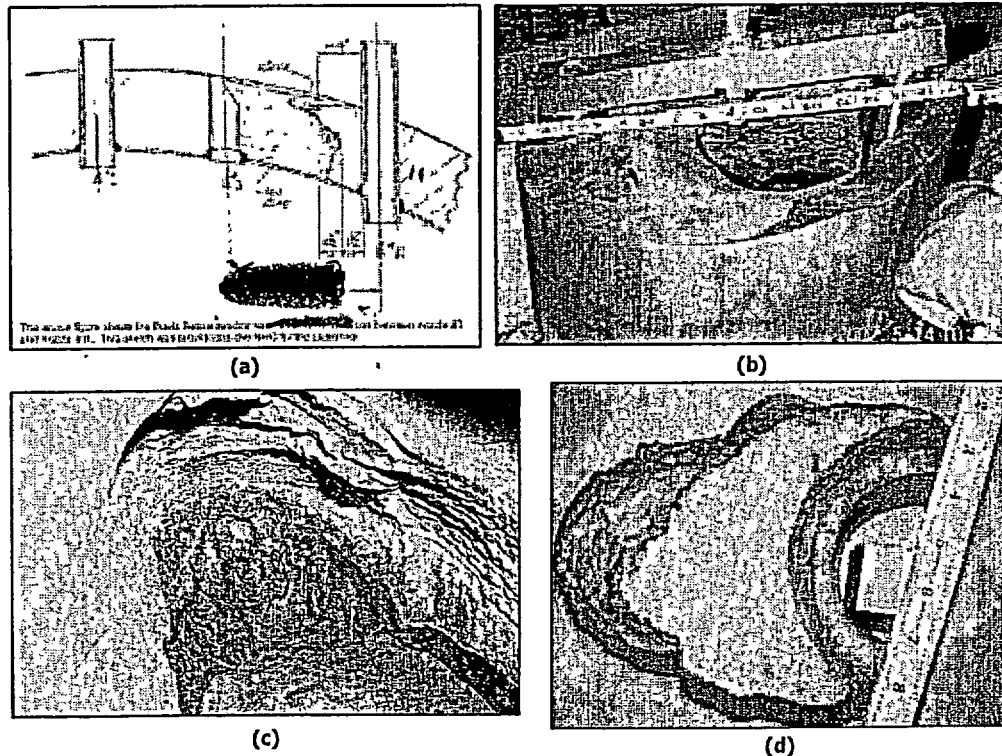


Figure 1.2. Diagrams and photos of the Davis Besse wastage area at nozzle three: (a) Sketch of thru-thickness extent provided in April 2002 by the licensee [FENOC 4/02], (b) View of the cavity from the outer radius once the Nozzle 3 plug was removed from the head, (c) Close-up view of the "nose" of the wastage cavity, (d) Dental mold of the wastage cavity made by Framatome [FENOC 9/02a].

## 2. Modeling Methodology and Assumptions

### 2.1 Preliminary Analysis Results, and Modeling Philosophy

Soon after discovery of the wastage cavity at Davis Besse in March of 2002, RES tasked ORNL to provide a preliminary analysis of the rupture capacity of the cladding that remained over the wastage cavity to maintain the primary pressure boundary. This analysis [Williams 4-02] showed that rupture of the cladding was not expected until a pressure of approximately 3000 psi, a pressure exceeding both the operating pressure (2165 psi) and the set-point pressure (2500 psi). A subsequent refinement of the failure criteria used by Williams was based on the close correspondence of the pressure at which numerical instability occurred in the finite element to analysis relative to the pressure at which rupture occurred in a series of burst disk experiments having exposure areas, membrane thicknesses, and materials similar to the conditions existing at Davis Besse [Riccardella 72]. Considerably higher rupture pressures (above 7000 psi) were predicted based on this refined failure criteria.

After these preliminary analyses were completed, NRR began a process of significance determination to assess the risk posed to the public by the condition at Davis Besse. To provide input to this analysis NRR requested that RES re-cast their early models [Williams 4-02] in a probabilistic framework, taking account of uncertainties that influence the predicted rupture pressures. Because Davis Besse reflects a fixed condition, many variables that effect the predicted rupture pressure are not uncertain but are, in principal and in fact, knowable. This, combined with the fact that the detailed knowledge needed to support a full probabilistic analysis was unavailable at the time the results of the analyses requested by NRR were needed (Summer 2002), prompted RES and ORNL to bound conservatively (rather than represent as uncertain) a number of variables in these analyses. In view of the very high margin against rupture revealed by the preliminary analysis, this approach was considered prudent, expedient, and not so excessively conservative as to present a distorted perspective on the likelihood of failing the primary pressure boundary at Davis Besse.

In the remainder of this Section we discuss both the finite element model of the Davis Besse head as well as the assumptions made in constructing this model.

### 2.2 Finite Element Analysis Model

This analysis features a complete geometric representation of the Davis Besse head subjected to internal pressure at a temperature of 600°F. A global model of the complete head and all of the CRDM penetrations establishes the displacement boundary conditions on a submodel of the region around nozzle 3 (see Figure 2.1). This model/submodel approach was employed to capture the effects of geometric complexity at both a large scale (the CRDM penetrations) and at a small scale (the wastage cavity itself) on the stress and deformation conditions in the exposed cladding. This model defined the geometric and boundary conditions for an elastic-plastic analysis using the commercial finite element

software ABAQUS. Complete details of this analysis methodology is available in the attached documents [Williams 9-02a, Williams 9-02b].

## 2.3 Assumptions

### 2.3.1 Assumptions Concerning Variables

In Table 2.1 we detail all of the variables known to affect the predicted rupture capacity of the un-backed cladding. Table 2.2 provides a classification scheme for these variables. The columns in Table 2.2 distinguishes variables that are in principal knowable, and are therefore deterministic for the purposes of this calculation, from variables that have values that are inherently uncertain. The rows in Table 2.2 describe how each of these variables was treated in our model. In Table 2.3 we overlay the classification scheme of Table 2.2 on the variables in Table 2.1. This coding provides a systematic context to discuss the assumptions that underlie our analysis.

Table 2.1. List of all variables that can effect predicted rupture capacity.

<b>Geometry</b>	<b>Loading</b>	<b>Material</b>
G1. Overall design of head	L1. Internal pressure	M1. Constitutive behavior of RPV steel
G2. Geometry of wastage cavity	L2. Thermal gradient across cladding	M2. Constitutive behavior of cladding
G3. Area of cladding exposed by wastage	L3. Welding residual stresses	M3. Constitutive behavior of Alloy 600
G4. Thickness of cladding		M4. Fracture toughness & tearing resistance of cladding
G5. Surface relief of cladding		
G6. Reinforcement of unbacked cladding provided by the J-groove weld		
G7. Flaws in cladding		

Table 2.2. Variable classification strategy.

<b>Modeling Approach</b>	<b>Variable Type</b>	
	<b>Deterministic</b>	<b>Uncertain</b>
Modeled accurately	XXX	XXX
Modeled as uncertain	N/A	XXX
Modeled conservatively (and deterministically)	XXX	XXX
Not modeled	XXX	XXX

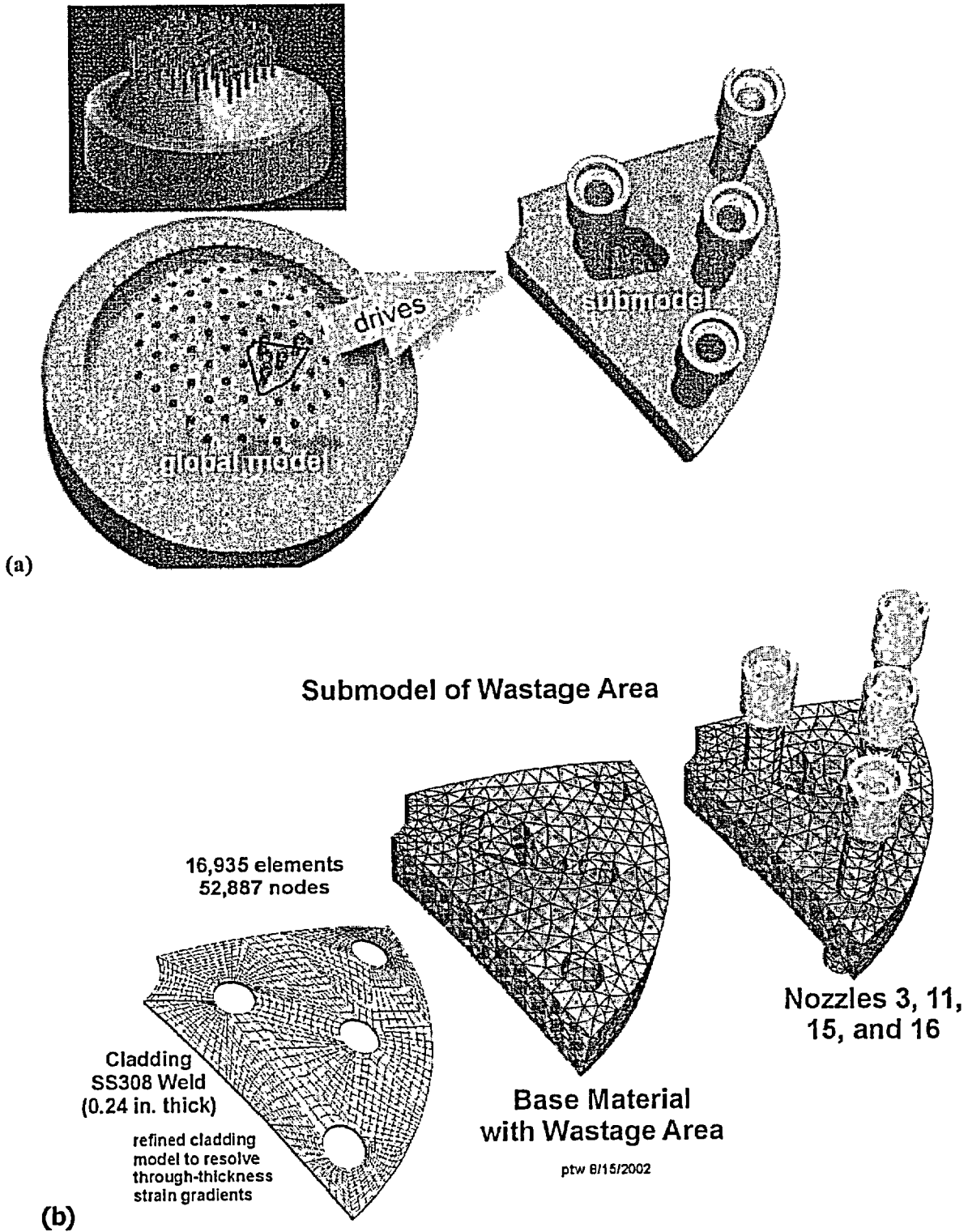


Figure 2.1. Finite element global and submodels of the Davis Besse wastage area. The displacements at the vertical side boundaries of the submodel are driven by the global model. Both models are exposed to the same pressure loading.

Table 2.3. Description of how variables that effect predicted rupture capacity were modeled.

Geometry	Loading	Material
G1. Overall design of head	L1. Internal pressure	M1. Constitutive behavior of RPV steel
G2. Geometry of wastage cavity	L2. Thermal gradient across cladding	M2. Constitutive behavior of cladding
G3. Area of cladding exposed by wastage	L3. Welding residual stresses	M3. Constitutive behavior of Alloy 600
G4. Thickness of cladding		M4. Fracture toughness & tearing resistance of cladding
G5. Surface relief of cladding		
G6. Reinforcement of un-backed cladding provided by the J-groove weld		
G7. Flaws in cladding		

**2.3.1.1 Variables Modeled Accurately**

Both the overall design of the head (G1) and the internal pressure loading (L1) have been modeled accurately relative to the physical conditions existing in the Davis Besse plant.

Despite the fact that the constitutive properties of both the RPV steel (M1) and the Alloy 600 material (M3) have inherent to them some variability, these properties were represented deterministically to the finite element model using the typical properties illustrated in Figure 2.1. This approximation is not expected to degrade the fidelity of the rupture pressure predicted for the cladding because given the configuration of the Davis Besse wastage cavity both the RPV steel and the Alloy 600 will remain predominately in the elastic range throughout loading.

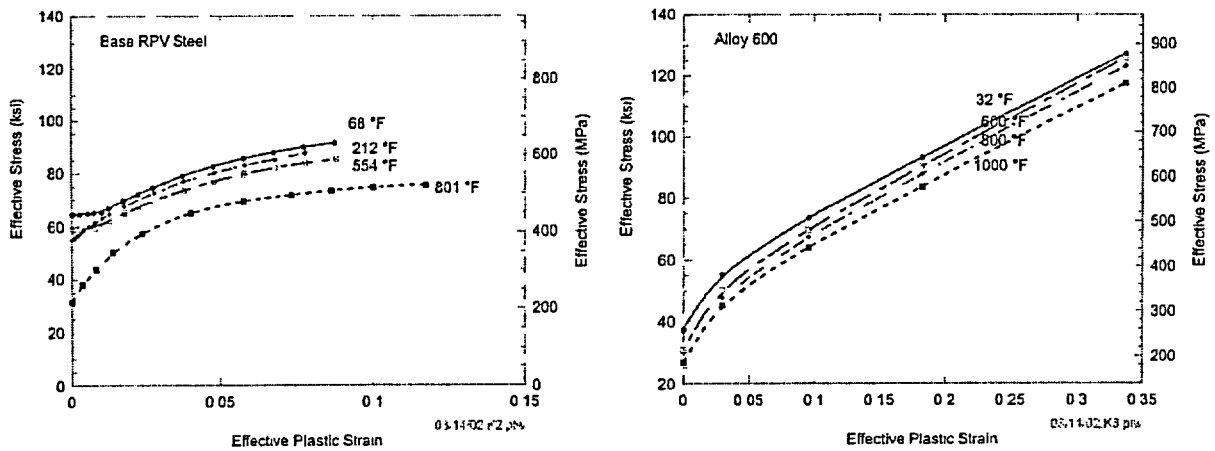


Figure 2.1. Tensile properties adopted for RPV steel (left) and for Alloy 600 (right).

### 2.3.1.2 Variables Modeled Conservatively

#### 2.3.1.2.1 Geometric Variables

We attempted to represent conservatively to our finite element model all geometric variables associated with the wastage cavity {its geometry (G2), the area of cladding exposed by the wastage cavity (G3), the thickness of the cladding (G4), and the reinforcement of the un-backed cladding provided by the J-groove weld (G6)} because at the time we constructed our model no fully detailed and accurate information regarding any of these variables was available. Information reported by FENOC on April 14, 2002 provided the basis for the following conservative representations.

- Information on the geometry of the wastage cavity, the area of exposed cladding, and the reinforcement of the cladding by the J-groove weld were available only from hand drawn sketches presented in Figure 13 of the April 14, 2002 FENOC report [FENOC 4/02]. These sketches were based on visual inspections and measurements made while the cavity was still part of the RPV head, so exposure times needed to be limited. Lacking more definitive information the decision was made to include the following conservative features in the finite element model:
  - The intersection between the cladding and the RPV wall was modeled as a sharp angles, not gradual transitions, and
  - The reinforcing effect of the J-groove weld was not modeled.

To determine the area of cladding that was no longer backed by RPV steel, ORNL digitized the hand-drawn sketches of the cavity provided in Figure 13 of FENOC's April 14, 2002 [FENOC 4/02]. Additionally, because there was uncertainty in these measurements the decision was made to increase the dimensions of this exposed area by ¼-in. normal to the outer profile of the cavity. Figure 2.1 compares the area of exposed cladding as it is represented in our finite element model with the dental mold of the cavity reported by FENOC in September 2002 [FENOC 9/02a]. This comparison demonstrates that the assumptions made regarding the exposed cladding area, the geometry of the cavity, and regarding exclusion of the J-groove weld are *ALL* conservative relative to the actual configuration of the Davis Besse wastage cavity.

- Information on the thickness and surface relief of the exposed cladding area were available only from hand drawn sketches presented in Figure 14 of FENOC's April 14, 2002 report. These sketches were based on a UT inspections made on a ½-in. grid spacing while the cavity was still part of the RPV head, so exposure times needed to be limited. These measurements showed that the exposed cladding varied in thickness from 0.24- to 0.35-in. Lacking more definitive information the decision was made to model the cladding as a sheet of uniform thickness equal to the minimum measured value (0.24-in.). Additionally, an analysis was performed using the specified nominal cladding thickness (3/16-in.) to account conservatively for uncertainties in the FENOC's measurements.

More recent dial gage measurements made after the wastage cavity was removed from the RPV head provide a more accurate representation of the cladding thickness in the wastage region [FENOC 9/02b]. These measurements (see Figure 2.2) show a cladding thickness ranging from 0.20- to 0.31-in. with an average value of 0.26-in. While the reported minimum cladding thickness of 0.20-in. falls below the earlier reported minimum of 0.24-in. that was used in the finite element model, examination of the contour plot in Figure 2.2 reveals that only a very small percentage of the exposed cladding area is thinner than 0.24-in. This, combined with the conservative treatment of cavity geometry, total wastage area, and J-groove weld reinforcement documented by Figure 2.1 suggest that

the overall representation of the wastage cavity and its surroundings to the finite element model can be regarded as conservative.

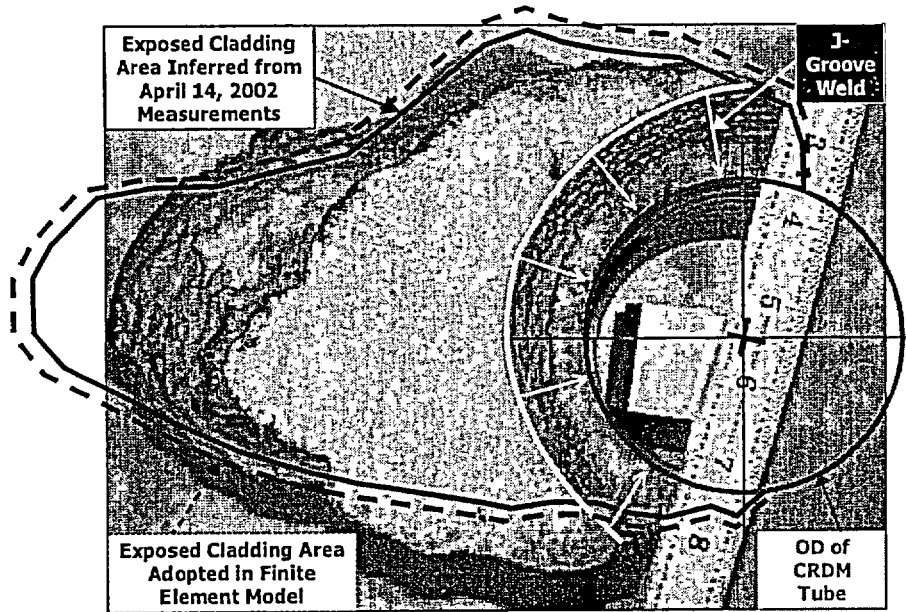
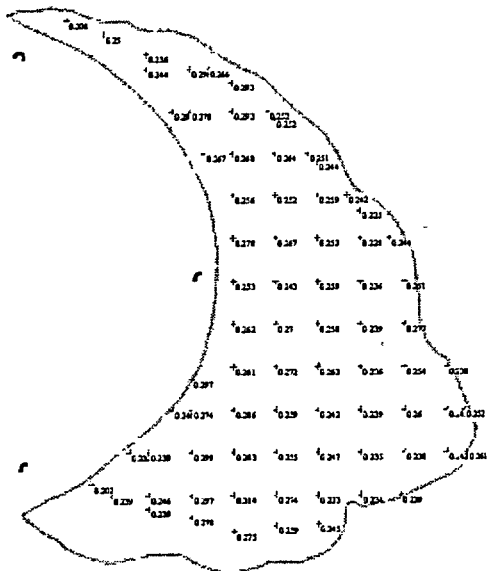


Figure 2.1. Comparison of the exposed cladding area measured by the dental mold impression taken in September 2002 [FENOC 9/02a] and the representation of the exposed cladding area adopted in the finite element analysis that was based on measurements reported in April 2002 [FENOC 4/02].



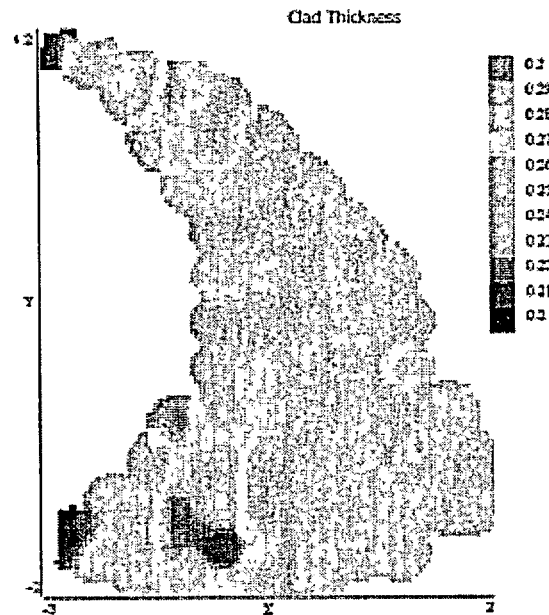


Figure 2.2. Measurements of cladding thickness based on dial gage measurements reported by FENOC in September 2002 (left: measurement data, right: computer generated contour map) [FENOC 9/02b].

### 2.3.1.2.2 Material Variables

We attempted to represent conservatively to our finite element model the constitutive behavior of the 308 stainless steel cladding (M2). Figure 2.1 compares stress-strain data for 308 stainless steel welds (not cladding) from [Ghadiali 96] with the bounding curve adopted in our finite element analysis. Despite the scatter evident in the tensile data, the decision was made to represent the cladding stress-strain properties deterministically for the following reasons:

- While the data in Figure 2.1 is for 308 stainless steel welds, it is not for 308 stainless steel cladding deposited on ferritic steel. Differences in welding procedures and weld dilution between standard welding and cladding practices were therefore not reflected by these data. Rather than speculate about what these effects might be, it was felt more appropriate to take a bounding approach.
- As mentioned earlier, preliminary calculations showed the expected margin against cladding rupture to be very high. It was therefore felt that the results of this bounding characterization of the cladding tensile properties would not degrade this margin in any significant way.

In Figure 2.2 we compare the cladding stress-strain curve assumed in our finite element analysis with tensile property data reported recently by FENOC based on two tests of the Davis Besse cladding material [FENOC 9/02c]. This comparison demonstrates the appropriateness of the tensile properties assumed in our finite element model of the Davis Besse wastage cavity.

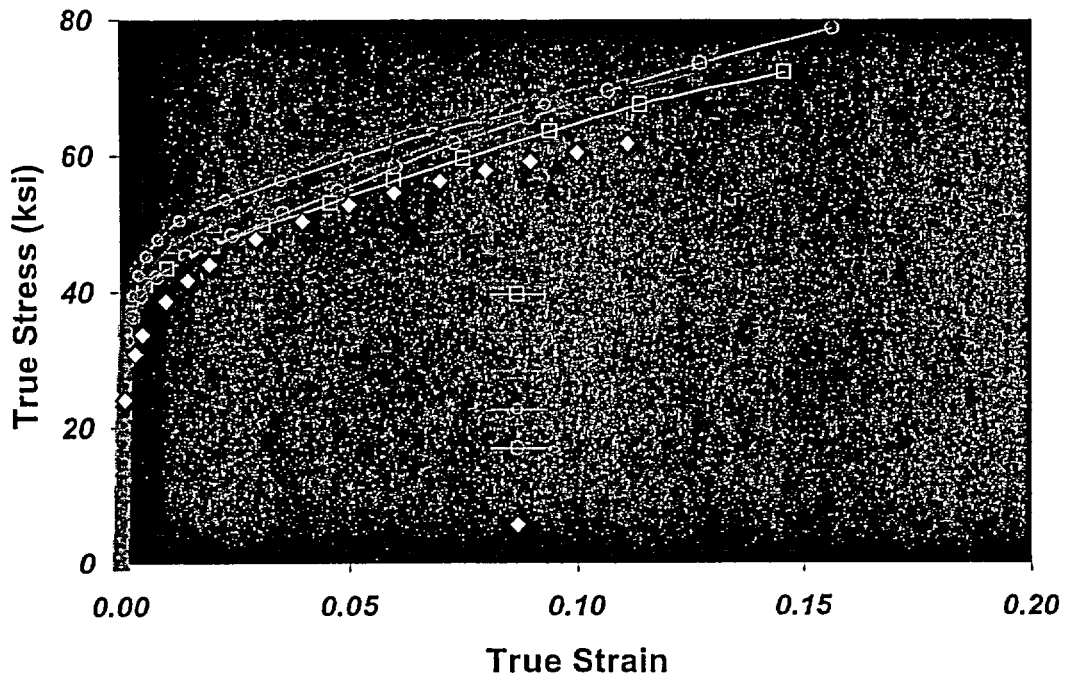


Figure 2.1. Comparison of 308 stainless steel tensile data with the stress-strain relationship assumed in the ORNL/NRC finite element model.

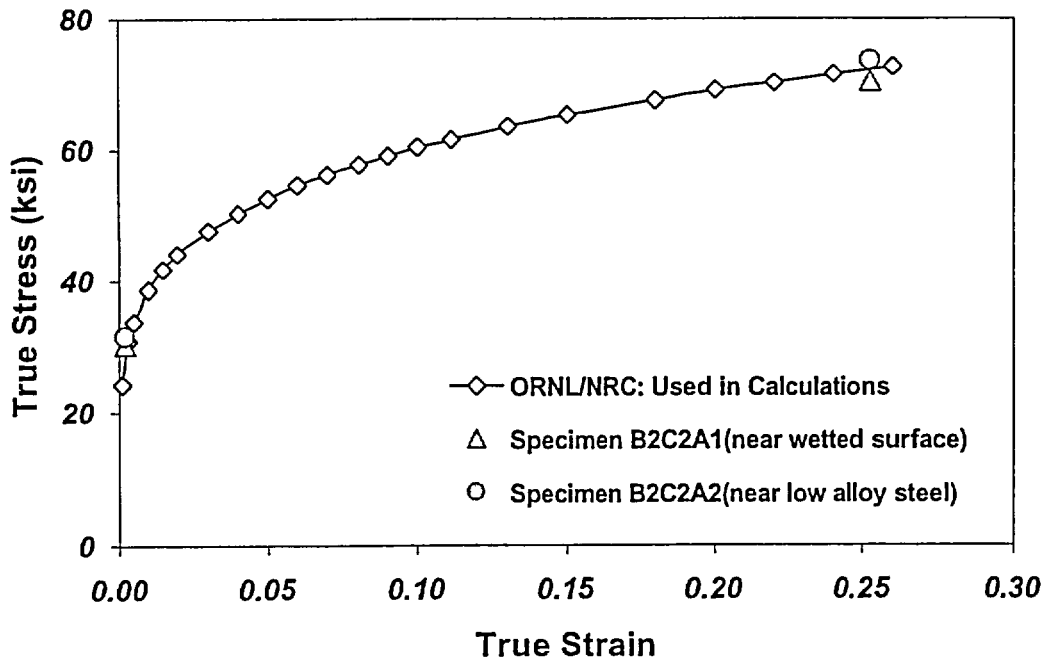


Figure 2.2. Comparison of 308 stainless steel tensile data obtained by testing the cladding material removed from Davis Besse with the stress-strain relationship assumed in the ORNL/NRC finite element model.

### 2.3.1.3 Variables Not Modeled

As detailed in Table 2.3, the following variables that could influence the predicted rupture pressure were not modeled:

- G5: Surface relief of the cladding
- L2: Thermal gradient across the cladding
- L3: Residual stresses in the cladding
- G7 & M4: Flaws in the cladding, and cladding toughness properties

The justification for ignoring each of these variables will be discussed in the following sections.

#### 2.3.1.3.1 Surface relief of the cladding

Weld deposited cladding can have some surface relief (e.g., re-entrant corners between adjacent weld beads) that could produce stress concentrations that could reduce the rupture capacity of the cladding. However, in normal cladding practice the size of this surface relief is usually quite small and, consequently, is not expected to produce significant stress concentrations. The decision was therefore made to represent the cladding over the wastage cavity as a sheet of uniform thickness. To take some account of surface relief effects uniform thicknesses of the minimum measured value (0.24-in.) and of the nominal specified value (3/16-in.) were selected for analysis.

Figure 2.1 shows information that has recently become available regarding cladding surface relief [FENOC 9/02b]. This information attests to the appropriateness of the assumptions made in constructing our finite element model.

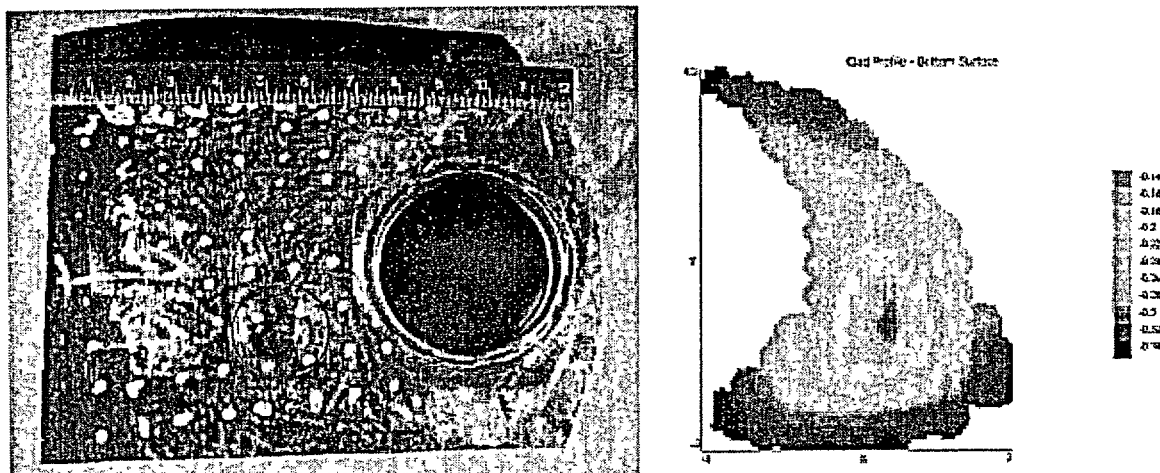


Figure 2.1. Photograph and computer generated representation of the surface relief of the exposed cladding (RCS side) in and around the Nozzle 3 wastage area.

#### 2.3.1.3.2 Thermal gradient across the cladding

The temperature on the inner cladding surface (inside the RCS) was 600°F, while the temperature on the outer cladding surface (in the wastage cavity) had to be less because this cavity was not pressurized. Good information regarding the temperature inside the cavity was not (and is not still) available largely because the conditions inside the wastage cavity are still a matter of great speculation. Even if one

assumes the cavity is filled with boiling water at atmospheric pressure (T=212°F) there is very likely to exist a steam bubble layer on the cladding surface in the wastage cavity that insulates the cladding from the boiling water. Because of this insulating effect it was therefore considered that the thermal gradient would not produce significant strains in the cladding relative to those produced by RCS pressure.

### 2.3.1.3.3 Residual stresses in the cladding

During the time period these calculations were being performed, insufficient information was available to permit incorporation of the effects of welding residual stresses into our finite element model. In view of the significant overpressure needed to rupture the clad membrane determined in the preliminary analysis, the effects of residual stresses were judged to be of second order importance and were, therefore, ignored.

### 2.3.1.3.4 Flaws in the cladding, and cladding toughness properties

The effect of pre-existing crack-like defects was not considered in our finite element analysis for the following two reasons:

1. While present, flaws in weld deposited stainless steel cladding tend to be quite small. This assumption is substantiated by work on flaw distributions in RPV materials conducted over the last several years by the Pacific Northwest National Laboratory for the NRC Office of Nuclear Regulatory Research (see Figure 2.1) [Simonen 02]. When scaled to reflect the size of the Davis Besse wastage cavity (see Figure 2.2) these data show that only a few very small flaws are expected in the wastage area, and that there is at most a 50% change of finding a flaw that has a depth of at least 10% of the cladding thickness.
2. Stainless steel is by its nature a very tough and ductile material that has a very high work hardening capacity. These characteristics combine to mitigate the effects of small flaws.

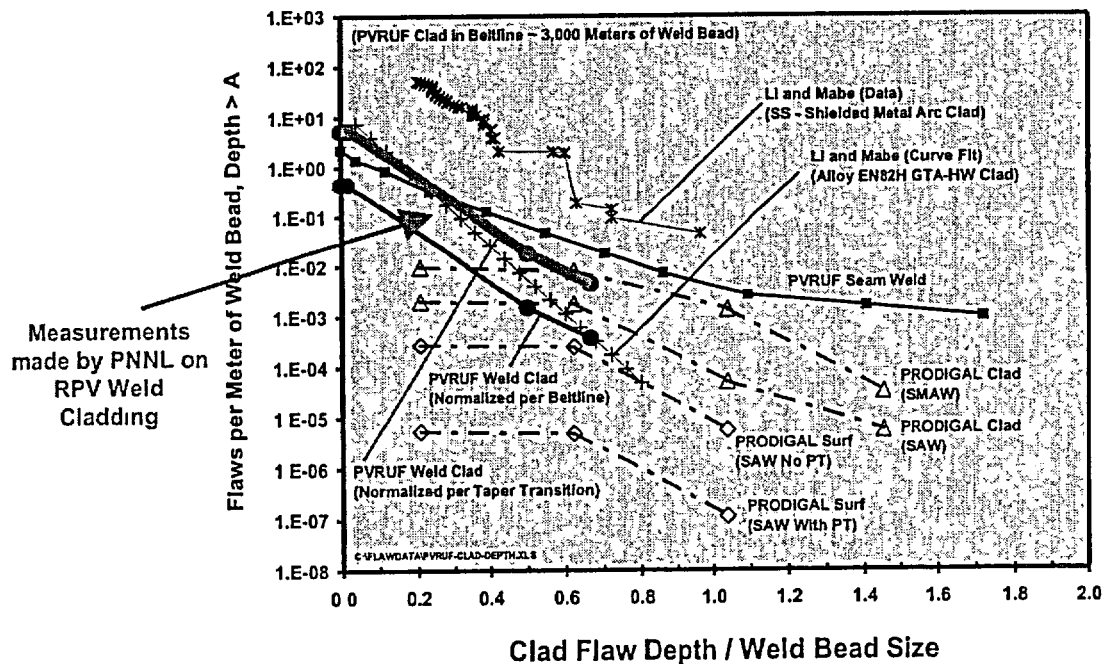


Figure 2.1. PNNL flaw distribution for welded stainless steel cladding (thick red line).

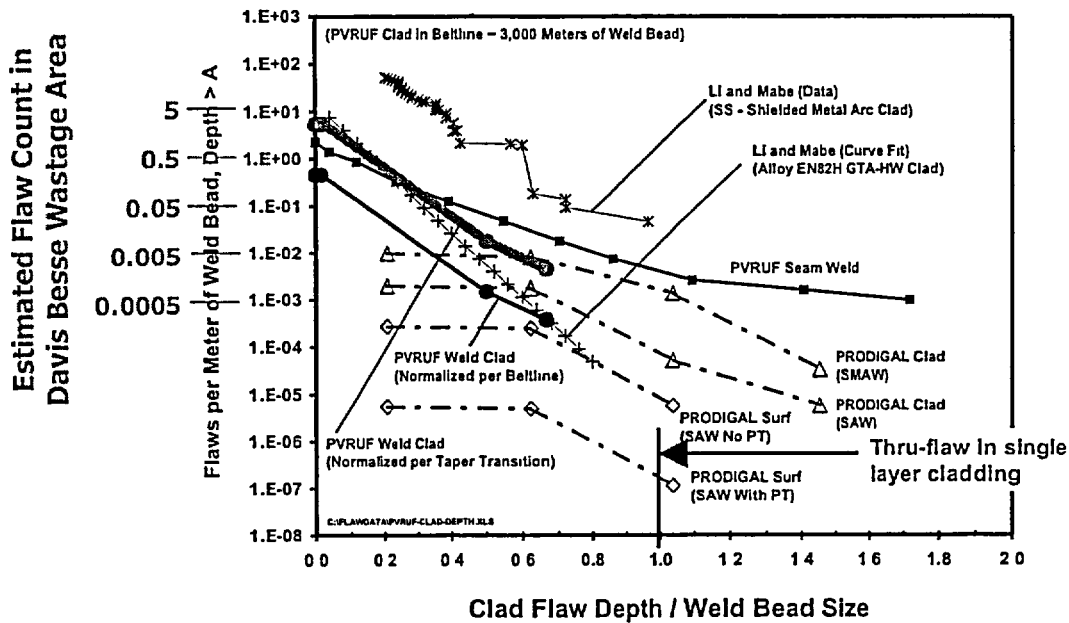


Figure 2.2. PNNL flaw distribution scaled to give the expected number of flaws based on the size of the Davis Besse wastage cavity (this scaling assumes that the wastage cavity has ½ m of weld bead, an assumption validated by the data in Figure 2.1).

### 2.3.2 Assumptions Concerning Failure Model

Finite element computations do not predict “failure” unless a damaging constitutive relationship is used (e.g. the Gurson model is often used to predict the failure of metals by ductile tearing [Gurson 77]). Within the timeframe available for performing this analysis it was not considered feasible to introduce the complexities inherent to such an approach. Additionally, no material constants were available to characterize the 308 stainless steel in the way needed by the Gurson model. Consequently, we employed a continuum constitutive model and adopted a failure criteria assessed external to the finite element analysis itself.

To calibrate our failure criteria we identified a series of nine pressurized burst-disk experiments in the literature [Riccardella 72]. These experiments included materials, thicknesses, and areas exposed to pressure that very close to those those that existed in the Davis Besse wastage cavity. By performing finite element analyses of each of these nine experiments we determined that the median instability pressure of the burst disks was fell 10% below the experimentally measured burst pressures. As illustrated in Figure 2.1 the finite element analysis predicted the experimental burst pressures quite well: the 5% / 95% confidence bound on the ratio { Experimental Burst Pressure / Pressure at Numerical Instability} is 0.9 to 1.35. The cumulative distribution function in Figure 2.1 quantifies both the bias and the uncertainty in predictions based on ABAQUS finite element analysis of the exposed cladding that covers the wastage cavity at Davis Besse.

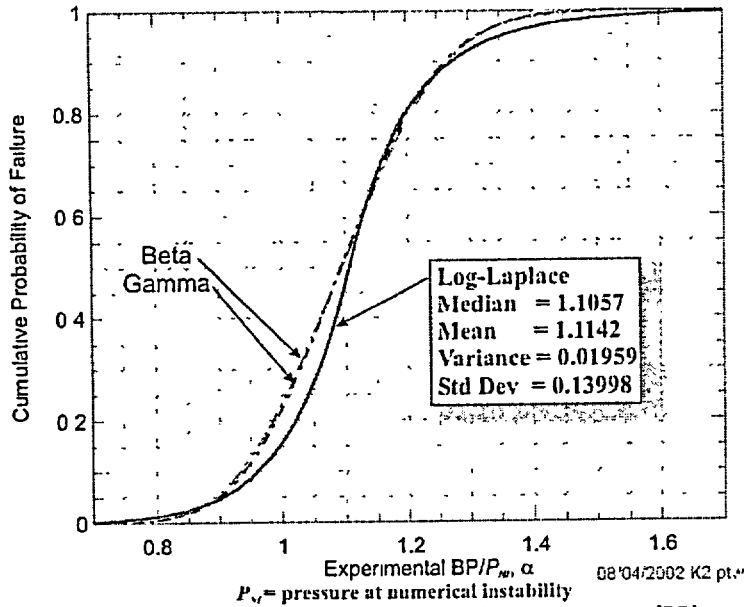


Figure 2.1. Cumulative distribution functions for the ratios of burst pressure (BP) measured experimentally by Riccardella to the pressure at numerical instability ( $P_{NI}$ ) in an ABAQUS finite element analysis.

### 2.3.3 Summary

In order to complete these analyses in a timely fashion it was necessary to make a number of assumptions regarding both the input variables and the failure model, as detailed in Sections 2.3.1 and 2.3.2, respectively. Assessment of the appropriateness of these assumptions relative to information that has become available since our analysis has been completed demonstrates that these assumptions are either accurate or conservative. Consequently, we expect the results of the analyses described in Section 3 to be either accurate or conservative predictions of the pressure it would take to rupture the cladding covering the Davis Besse wastage cavity.

## 3. Analysis Results: Rupture Pressures and Probabilities

### 3.1 As-Found Condition (Condition at February 16, 2002 Shutdown)

The attached report

Williams, P.T. and Bass, B.R., "Stochastic Failure Model of the Davis Besse RPV Head," August 23, 2002, ORNL/NRC/LTR-????.

provides all the details of our analysis of the rupture capacity of the Davis Besse head in the condition that existed on February 16, 2002. Based on the assumptions detailed in Section 2.3 these analyses predict a 50<sup>th</sup> percentile failure pressure of  $\approx 7300$  psi. This failure pressure is for a uniform cladding thickness of 0.24-in. (the minimum cladding thickness reported by FENOC in April 2002). If the uniform cladding thickness were 3/16-in (the nominal specified thickness, a value lower than any of the more accurate dial gage measurements of the cladding in September 2002) this 50<sup>th</sup> percentile failure pressure would be  $\approx 5700$  psi. Both of these 50<sup>th</sup> percentile failure pressures exceed considerably both the operating pressure (2165 psi) and the set point pressure (2500 psi) at Davis Besse. Consequently, we used the cumulative distribution function of Figure 2.1 to estimate the failure probabilities at these lower pressures, complete with consideration of the uncertainties in our analysis. On this basis the failure probability for a uniform cladding thickness of 0.24-in. was determined to be  $\approx 7 \times 10^{-8}$  at the operating pressure and  $\approx 4 \times 10^{-7}$  at the set point pressure. These very low failure probabilities coupled with the fact that the assumptions detailed in Section 2.3 are either accurate or conservative support the conclusion that failure of the clad membrane in the condition that existed at Davis Besse February 16, 2002 was an exceedingly unlikely event.

### 3.2 Potential Future States

The attached report

Williams, P.T. and Bass, B.R., "Analysis of the Davis Besse RPV Head Wastage Area and Cavity," October ??, 2002, ORNL/NRC/LTR-????.

provides all the details of our analysis of wastage cavities larger than the cavity that existed at Davis Besse on February 16, 2002. Figure 3.1 illustrates the growth patterns considered in our analysis. The different patterns in Figure 3.1 were modeled to (a) examine the effects of the edge of the wastage cavity interacting with the edge of the finite element sub-model, and to (b) examine the effect of cavity shape on the rupture capacity of the stainless steel cladding. The specific growth pattern that would have occurred had operation continued is the topic of continued debate, and depends on the mechanism responsible for cavity growth. In this study we neither postulate nor support any particular cavity growth mechanism, but rather examine the question of what the rupture capacity of the clad membrane would have been had the wastage cavity somehow enlarged to a particular size.

Figure 3.2 summarizes the results of our analysis for the growth patterns in Figure 3.1. The estimated rupture capacity for these growth patterns (shown as discrete points on Figure 3.2) compare well with the rupture capacity of a circular membrane (shown as a curve on Figure 3.2) estimated using a closed-form plasticity solution [Chakrabarty 1970]. This agreement suggests that the cavity shape exerts a second-order influence on the rupture capacity of the unbacked cladding relative to the more significant influence of the area of unbacked cladding.

In Table 3.1 we combine the Chakrabarty and Alexander theory that gives a closed form solution for the rupture capacity of circular diaphragms with the stochastic failure model of Figure 2.1 that was based on the burst disk experiments performed by Riccardella to provide an approximate and *bounding* analysis of how much larger the cavity could have become before rupture of the cladding was likely at or slightly above the operating pressure (2165 psi). In addition to the information in Figure 3.2 and in Figure 2.1 this analysis depends on the following information and assumptions:

1. An estimate of 24 sq.-in. for the exposed cladding area (this includes the area of the J-groove weld) based on the photograph in Figure 2.1.
2. An assumption that the original shape of the corrosion cavity is circular, and that corrosion makes the cavity grow outward as a series of concentric circles. This assumption is obviously incorrect and is adopted *only* for the purposes of obtaining a *bounding* estimate of the cavity growth needed to result in rupture of the cladding at pressures near the operating pressure (a corrosion cavity growing as a series of concentric circles exposes the greatest amount of clad area for the least amount of radial growth).

Within the limits imposed by these assumptions, the information in Table 3.1 indicates how much larger the cavity could have become before rupture of the cladding was likely at or slightly above the operating pressure (2165 psi). To use these cavity sizes to estimate how long corrosion could have continued at Davis Besse before rupture occurred, some estimate of the corrosion growth rate is necessary. In a recent review, Cullen postulated that the conditions in the Davis Besse wastage cavity can best be represented by a solution that is constantly replenished at a temperature near 212°F [MEB 9/02]. For these conditions Cullen collected the data from the literature reproduced in Figure 3.3. These data show a significant effect of boric acid concentration on the corrosion growth rate. Since the boric acid concentration in the Davis Besse cavity remains to be determined, we present in Figure 3.4 estimates of the additional corrosion time needed to rupture the cladding over the Davis Besse cavity for the range of corrosion growth rates given in Figure 3.3.

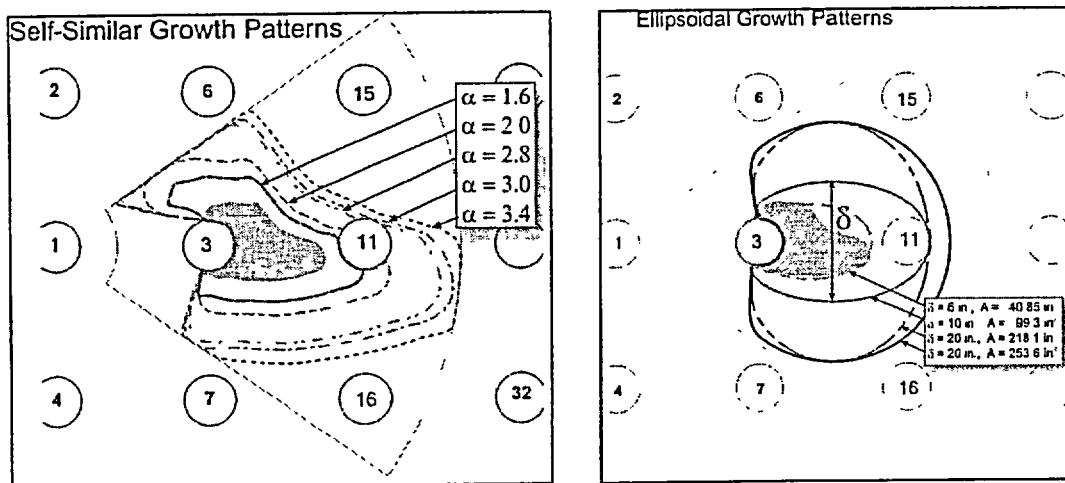
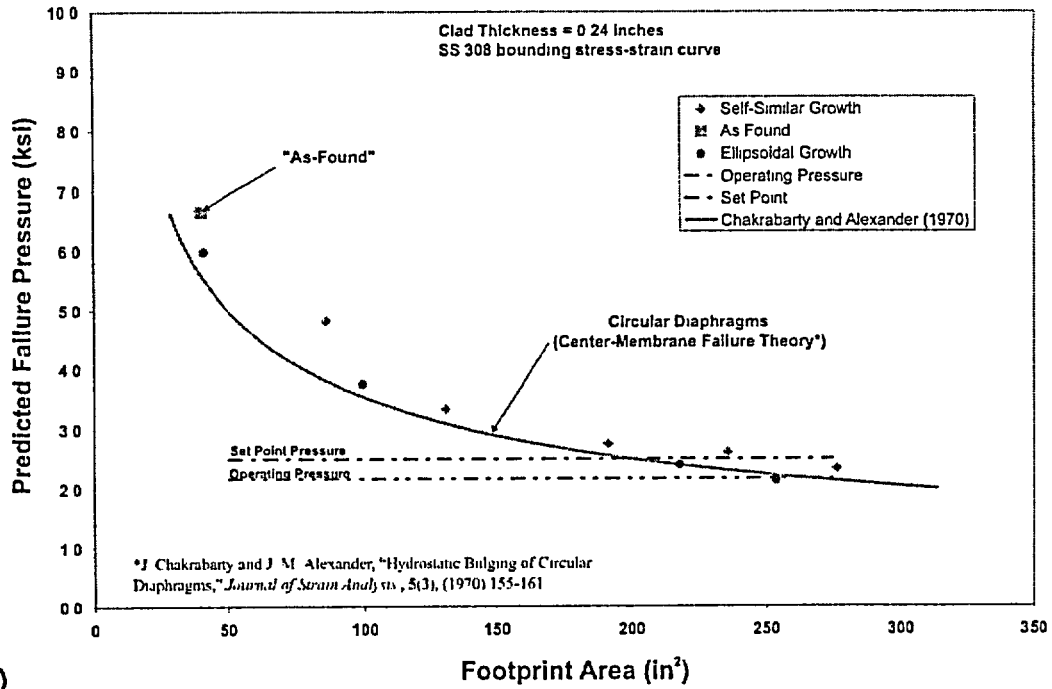
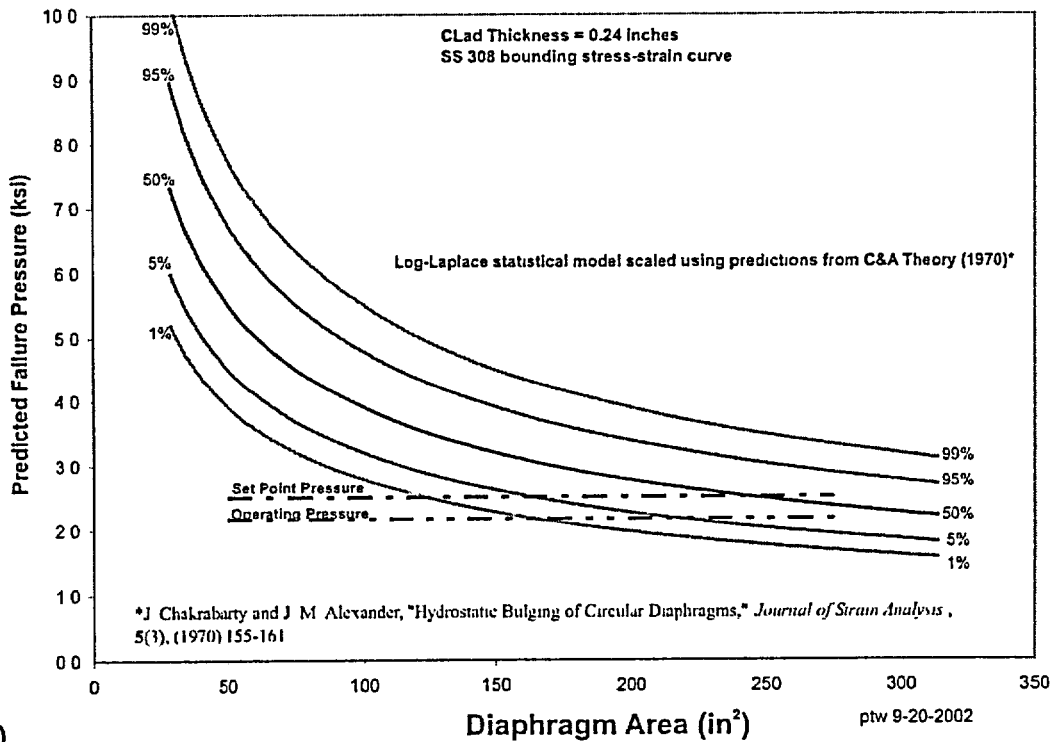


Figure 3.1. Growth patterns assumed in the analysis of wastage cavities larger than that which existed at Davis Besse on February 16, 2002.



(a)



(b)

Figure 3.2. Summary of the effect of wastage cavity size and shape on rupture capacity of the clad membrane: (a) pressures at numerical instability,  $P_{NI}$ , calculated by ABAQUS finite-element submodels of postulated footprints are compared to burst pressures in circular diaphragms predicted by the theory of Chakrabarty and Alexander (1970), and (b) stochastic failure model scaled from the theory of Chakrabarty and Alexander (1970).

Table 3.1. Cavity sizes needed to produce rupture of the cladding membrane at the operating and set point pressures.

Condition		Area [sq-in]	Diameter [in]	Growth Needed to Rupture Cladding [in]
As Found Cavity		24	5.5	#N/A
Operating Pressure (2165 psi)	5% Failure Probability	218	16.7	5.6
	50% Failure Probability	325	20.3	7.4
Set Point Pressure (2500 psi)	5% Failure Probability	163	14.4	4.4
	50% Failure Probability	244	17.6	6.0

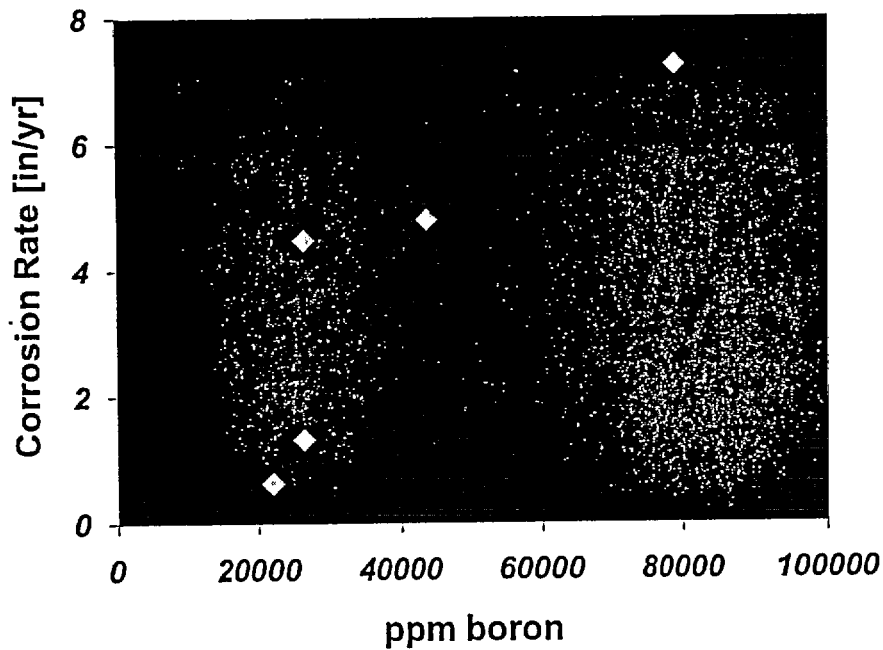


Figure 3.3. Corrosion rate data for steel subjected to a continuously replenished boric acid solution at a temperature near 212°F collected by Cullen [MEB 9/02].

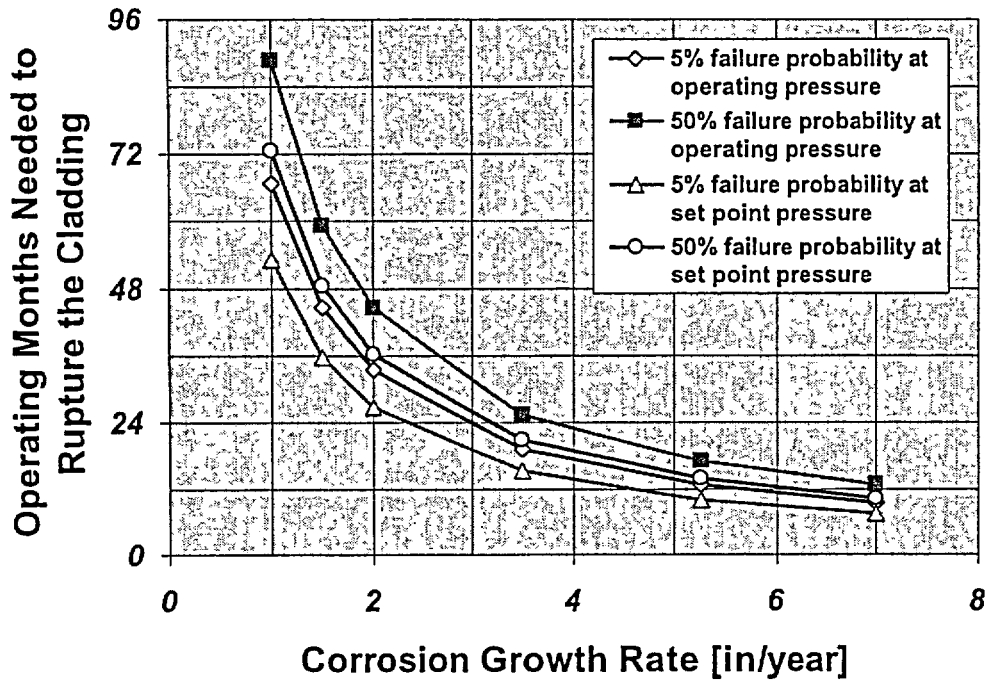


Figure 3.4. Estimates of the additional time needed to enlarge the Davis Besse cavity sufficiently so that rupture of the cladding would be expected to occur at or slightly above the operating pressure.

## 4. Summary and On-Going Work

In this report we have summarized the results of various finite element models of the corrosion wastage discovered at the Davis Besse nuclear power plant on February 16, 2002. These analyses have focused on estimating the rupture capacity of the cladding covering the wastage cavity that is no longer backed by reactor pressure vessel steel. The information presented herein supports the following conclusions concerning the cavity as it existed on February 16, 2002 when Davis Besse was shut down:

- The median failure pressure of this cladding in this condition is expected to be between 5700 and 7300 psi depending on the thickness of the cladding covering the wastage area. Recent dial gage measurements of the cladding thickness suggest that the expected median failure pressure is closer to the upper end of this range.
- Failure of the clad membrane in this condition at pressures up to the set-point pressure represents an extremely unlikely event. Failure probabilities are estimated to be in the  $10^{-7}$  to  $10^{-8}$  range.

Had the wastage condition not been discovered on February 16, 2002 and continued to grow, we (conservatively) estimate that between 4½ and 7½ more inches of corrosion wastage of the RPV steel in all directions would have been needed to rupture the cladding at pressures between the operating pressure and the set point pressure.

In our on-going research we continue to further refine these analyses. Our current focus is an assessment of the effect of cracks on the estimated rupture pressures presented herein. This study includes both analytical predictions as well as burst-disk experiments conducted on samples of 308 stainless steel cladding.

## 5. References

- Chakrabarty 70 J. Chakrabarty and J. M. Alexander, "Hydrostatic Bulging of Circular Diaphragms," *J. Strain Anal.* 5(3), (1970) 155-161.
- FENOC 4/02 Root Cause Analysis Report: Significant Degradation of the Reactor Pressure Vessel Head, CR 2002-0891, 4-15-2002.
- FENOC 9/02a Dental mold reference
- FENOC 9/02b Davis-Besse Reactor Head Sample Characterization, Phase 3 Status Report, 9/19/02.
- FENOC 9/02c Tensile data reference
- Ghadiali 96 Ghadiali, N., and Wilkowski, G.M., "Fracture Mechanics Database for Nuclear Piping Materials (PIFRAC)," in *Fatigue and Fracture – 1996 – Vol. 2*, PVP Col. 324, July 1996, pp. 77-84.
- Gurson 77 Gurson, A.L., "Continuum theory of ductile rupture by void nucleation and growth: Part I-yield criteria and flow rules for porous ductile media," *J. Eng. Mat. Tech.*, Vol. 9, 1977, pp. 2-15.
- MEB 9/02 Memorandum Chokshi to Bateman (Cullen's Report), September 30, 2002.
- Riccardella 72 P. C. Riccardella, "Elasto-Plastic Analysis of Constrained Disk Burst Tests," Paper No. 72-PVP-12, presented at the ASME Pressure Vessels and Piping Conference, September 17-21, 1972, New Orleans, LA.
- Simonen 02 Simonen, F.A., Doctor, S.R., Schuster, G.J., and Heasler, P.G., "A Generalized Procedure for Generating Flaw Related Inputs for the FAVOR Code," NUREG/CR-????, *in review*.
- Williams 4/02 Williams, P.T. and Bass, B.R., "Analysis of Davis Besse RPV Head with Detailed Submodel of Wastage Area: Summary of Current Status of Analysis," April 30, 2002.
- Williams 9/02a Williams, P.T. and Bass, B.R., "Stochastic Failure Model of the Davis Besse RPV Head," August 23, 2002, ORNL/NRC/LTR-????.
- Williams 9/02b Williams, P.T. and Bass, B.R., "Analysis of the Davis Besse RPV Head Wastage Area and Cavity," October ??, 2002, ORNL/NRC/LTR-????.

**Contract Program or  
Project Title:** Heavy-Section Steel Technology (HSST) Program

**Subject of this Document:** Stochastic Failure Model for the Davis-Besse RPV Head

**Type of Document:** Letter Report

**Authors:** P. T. Williams  
B. R. Bass

**Date of Document:** September 2002

**Responsible NRC Individual  
and NRC Office or Division** M. T. Kirk  
Division of Engineering Technology  
Office of Nuclear Regulatory Research

Prepared for the  
U. S. Nuclear Regulatory Commission  
Washington, D.C. 20555-0001  
Under Interagency Agreement DOE 1886-N653-3Y  
NRC JCN No. Y6533

OAK RIDGE NATIONAL LABORATORY  
Oak Ridge, Tennessee 37831-8056  
managed and operated by  
UT-Battelle, LLC for the  
U. S. DEPARTMENT OF ENERGY  
under Contract No. DE-AC05-00OR22725

# **Stochastic Failure Model for the Davis-Besse RPV Head**

P. T. Williams  
B. R. Bass

Oak Ridge National Laboratory  
Oak Ridge, Tennessee

Manuscript Completed -- September 2002  
Date Published --

Prepared for the  
U.S. Nuclear Regulatory Commission  
Office of Nuclear Regulatory Research  
Under Interagency Agreement DOE 1886-N653-3Y

NRC JCN No. Y6533

OAK RIDGE NATIONAL LABORATORY  
Oak Ridge, Tennessee 37831-8063  
managed and operated by  
UT-Battelle, LLC for the  
U. S. DEPARTMENT OF ENERGY  
under Contract No. DE-AC05-00OR22725

**CAUTION**

This document has not been given final patent clearance and is for internal use only. If this document is to be given public release, it must be cleared through the site Technical Information Office, which will see that the proper patent and technical information reviews are completed in accordance with the policies of Oak Ridge National Laboratory and UT-Battelle, LLC

This report was prepared as an account of work sponsored by an agency of the United States government. Neither the United States government nor any agency thereof, nor any of their employees, makes any warranty, express or implied, or assumes any legal liability or responsibility for the accuracy, completeness, or usefulness of any information, apparatus, product, or process disclosed, or represents that its use would not infringe privately owned rights. Reference herein to any specific commercial product, process, or service by trade name, trademark, manufacturer, or otherwise, does not necessarily constitute or imply its endorsement, recommendation, or favoring by the United States government or any agency thereof. The views and opinions of authors expressed herein do not necessarily state or reflect those of the United States government or any agency thereof.

# Stochastic Failure Model for the Davis-Besse RPV Head

P. T. Williams and B. R. Bass  
Oak Ridge National Laboratory  
P. O. Box 2009  
Oak Ridge, TN, 37831-8056

## Abstract

The development of a set of six stochastic models is described in this report in which the uncertainties associated with predictions of burst pressure for circular diaphragms using computational or analytical methods are estimated. It is postulated that the trends seen in predicting the burst pressure with nine experimental disk-burst tests (using materials, geometries, and pressure loadings relevant to the Davis-Besse analysis) will be representative of the computational predictions of the burst pressure in the Davis-Besse wastage-area problem. Given a computational prediction of the pressure at numerical instability,  $P_{NI}$ , for a specific configuration of the wastage area, the scaled stochastic models provide estimates of the failure pressure with a specific associated probability.

The stochastic models were developed from the following technical bases:

- (1) *experimental data* obtained during disk-burst tests with loadings, geometries, and materials relevant to the Davis-Besse pressure loading, wastage-area footprint, and cladding,
- (2) nonlinear, large-deformation, elastic-plastic *discrete-element analyses* of the disk-burst tests,
- (3) nonlinear, finite-strain, elastic-plastic *finite-element analyses* performed for the current study, and
- (4) a *theoretical criterion* for plastic instability in a circular diaphragm under pressure loading, applied to the disk-burst tests.

Among the twenty-six continuous distributions investigated, six passed all of the heuristic and *Goodness of Fit* tests applied in the analysis. The six distributions, ranked in relative order, are: (1) Log-Laplace, (2) Beta, (3) Gamma, (4) Normal, (5) Random Walk, and (6) Inverse Gaussian. Due to the small sample size ( $n = 26$ ) used in the stochastic model development, no definitive claim can be made that one distribution is significantly superior to the other five; however, the Log-Laplace is shown to have the highest ranking given the available data, and it produces the highest failure probabilities when extrapolating to service pressures well below the range of the data, e.g., to the nominal operating pressure or safety-valve set-point pressure. It is, therefore, recommended that the Log-Laplace stochastic model be applied in future studies for the Davis-Besse wastage-area problem.

As an example application, estimates are provided for a bounding calculation of the "as-found" Davis-Besse wastage area. The bounding calculation predicted a  $P_{NI}$  value of 6.65 ksi. From the Log-Laplace stochastic model, the corresponding median failure pressure is 7.35 ksi. The Log-Laplace model also estimates a cumulative probability of failure of  $4.14 \times 10^{-7}$  at the operating pressure of 2.165 ksi and  $2.15 \times 10^{-6}$  at the safety-valve set-point pressure of 2.5 ksi. Using all six distributions, the average probability of failure is  $6.91 \times 10^{-8}$  at 2.165 ksi,  $3.60 \times 10^{-7}$  at 2.5 ksi, and 0.2155 at 6.65 ksi.

# 1. Introduction

## 1.1. Objective

This report presents stochastic models of failure for the stainless steel cladding in the wastage area of the Davis-Besse Nuclear Power Station reactor pressure vessel (RPV) head. For a given internal pressure, the statistical models provide estimates of the cumulative probability (*probability of nonexceedance*) that the exposed cladding will have failed at a lower pressure. The failure mode addressed by this model is *incipient tensile plastic instability* (i.e., plastic collapse) of the cladding.

## 1.2. Background

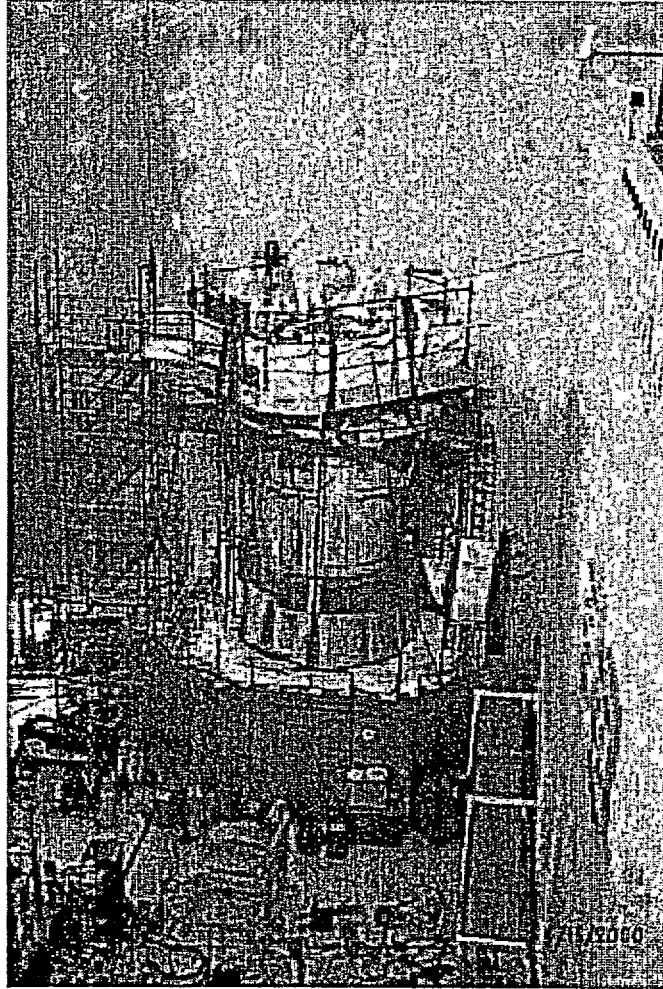
The following was taken from ref. [1].

On February 16, 2002, the Davis-Besse facility began a refueling outage that included inspection of the vessel head penetration (VHP) nozzles, which focused on the inspection of control rod drive mechanism (CRDM) nozzles, in accordance with the licensee's commitments to NRC Bulletin 2001-01, "Circumferential Cracking of Reactor Pressure Vessel Head Penetration Nozzles," which was issued on August 3, 2001. These inspections identified axial indications in three CRDM nozzles, which had resulted in pressure boundary leakage. Specifically, these indications were identified in CRDM nozzles 1, 2, and 3, which are located near the center of the RPV head. ... Upon completing the boric acid removal on March 7, 2002, the licensee conducted a visual examination of the area, which identified a large cavity in the RPV head on the downhill side of CRDM nozzle 3. Followup characterization by the ultrasonic testing indicated wastage of the low alloy steel RPV head material adjacent to the nozzle. The wastage area was found to extend approximately 5 inches downhill on the RPV head from the penetration for CRDM nozzle 3, with a width of approximately 4 to 5 inches at its widest part.

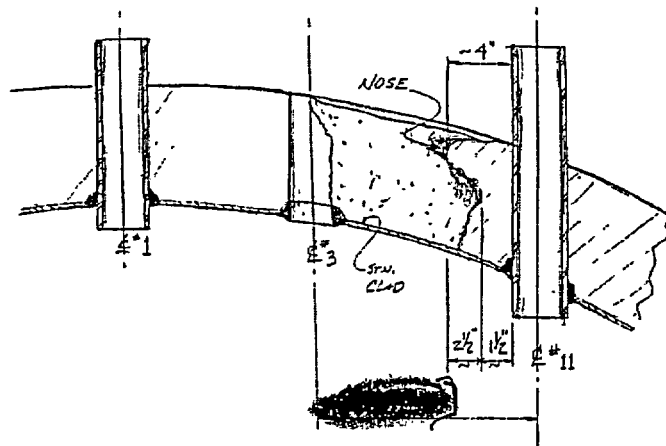
See Fig. 1. for a photograph of the Davis-Besse RPV, a schematic of a typical nuclear power reactor, and a sketch and photographs of the wastage area.

## 1.3. Scope

In support of the investigation by the United States Nuclear Regulatory Commission's (NRC) Office of Nuclear Regulatory Research, the Heavy-Section Steel Technology Program at Oak Ridge National Laboratory has developed statistical models for a specific failure mode for the exposed stainless steel cladding in the cavity of the Davis-Besse RPV head. Section 2 reviews the technical bases employed in the development of the models; Section 3 presents the details of the stochastic models; Section 4 demonstrates an application of the proposed candidate Log-Laplace model to the results of a bounding calculation for the "as found" condition of the wastage area; and Section 5 provides a summary and conclusions.



Davis Besse Reactor Vessel Head Degradation Head Cutaway View



EX 4

The above figure shows the Davis Besse reactor vessel head degradation between nozzle #3 and nozzle #11. This sketch was provided to the NRC by the Licensee.

Fig. 1. (a) Davis-Besse Nuclear Power Station RPV and (b) sketch of RPV head degradation.

## Typical Pressurized Water Reactor

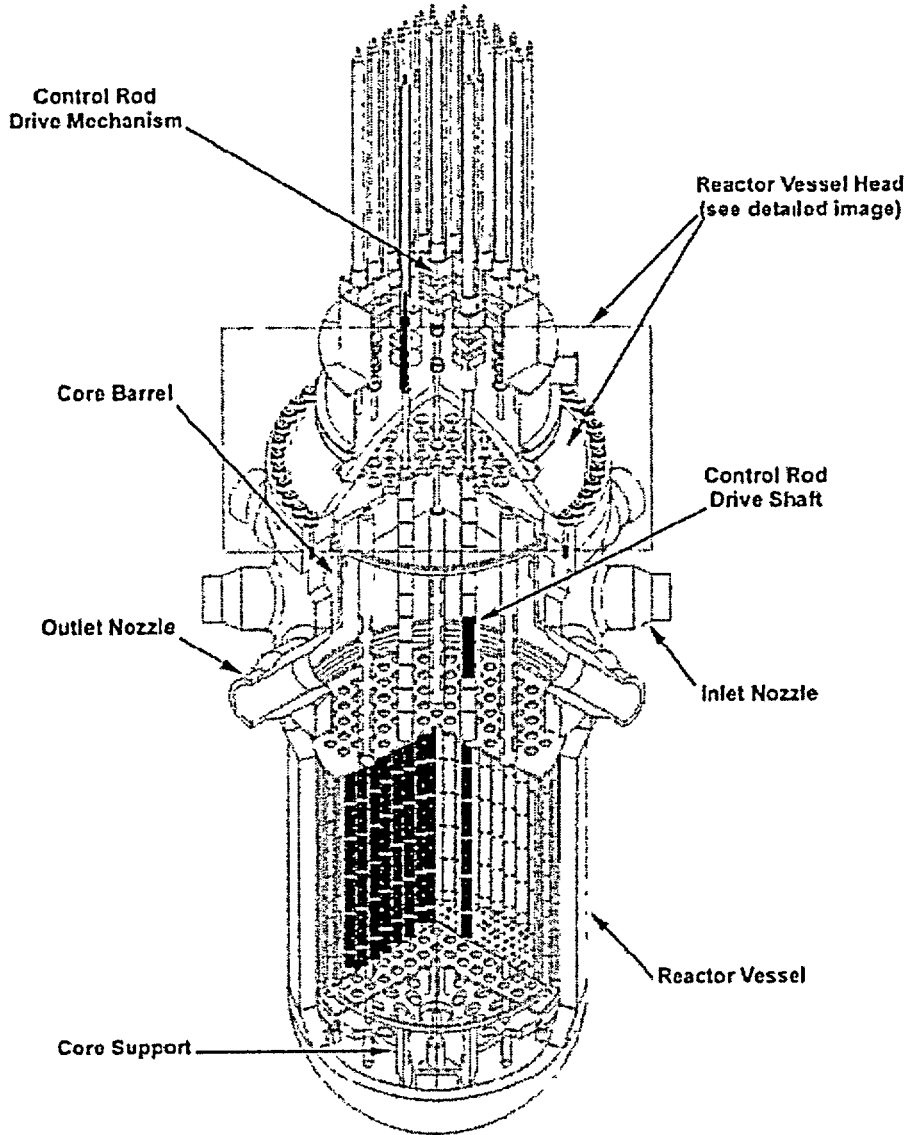


Fig. 1 (continued) (c) schematic of a typical nuclear power reactor showing the relationship of the CRDM nozzles to the RPV head.

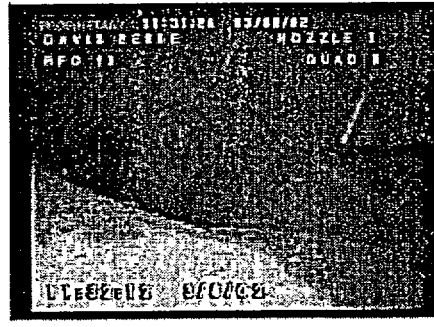
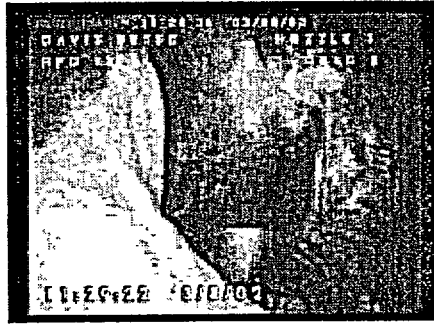


Fig. 1. (continued) (d) photographs of the wastage area with Nozzle 3 removed.

## 2. Technical Bases

The technical bases employed in the construction of the stochastic models are:

- (1) *experimental data* obtained during disk-burst tests reported by Riccardella [2] with loadings, geometries, and materials relevant to the Davis-Besse pressure loading, wastage-area footprint, and cladding,
- (2) nonlinear, large-deformation, elastic-plastic *discrete-element analyses* of the disk-burst tests also reported in [2] (GAPL-3 discrete-element code[3]),
- (3) nonlinear, finite-strain, elastic-plastic *finite-element analyses* performed for the current study (ABAQUS finite-element code[4]) of the nine disk-burst test specimens reported in [2], and
- (4) a *theoretical criterion* for plastic instability in a circular diaphragm under pressure loading, due to Hill [5] with extensions by Chakrabarty and Alexander [6] (as cited in [7]), applied to the disk-burst tests.

### 2.1. Experimental – Disk-Burst Tests

In the early 1970s, constrained disk-burst tests were carried out under the sponsorship of the *PVRC Subcommittee on Effective Utilization of Yield Strength* [8]. This test program employed a range of materials and specimen geometries that were relevant to components in a nuclear power plant steam supply system<sup>1</sup>. The geometries of the three test specimens analyzed in [2] are shown in Fig. 2, the test matrix is shown in Table 1, and the properties of the three materials are presented in Table 2. The nine disk-burst tests produced three center failures and six edge failures over a range of burst pressures from 3.75 to 15 ksi as shown in Table 1.

**Table 1. Test Matrix for Disk-burst Tests [2]**

Test Number	Material	Geometry	Fillet Radius (in.)	Diaphragm Thickness (in.)	Effective Diaphragm Radius (in.)	Experimental Results	
						Burst Pressure (ksi)	Location of Failure
1	SS 304	A	0.375	0.250	2.625	15	Edge
2		B	0.125	0.125	2.875	6.8	Center
3		C	0.375	0.125	2.625	7.7	Center
4	A533B	A	0.375	0.250	2.625	11	Edge
5		B	0.125	0.125	2.875	5.3	Edge
6		C	0.375	0.125	2.625	6.7	Center
7	ABS-C	A	0.375	0.250	2.625	9.8	Edge
8		B	0.125	0.125	2.875	3.75	Edge
9		C	0.375	0.125	2.625	4.94	Edge

<sup>1</sup> The three materials are representative of reactor core support structures and piping, the reactor pressure vessel, and plant component support structures [2].

Table 2. Property Data for Materials in Disk-burst Tests [2]

Material	Yield Strength	Ultimate	Strain at	True Stress	True Ultimate	Log Strain	Power Law Fit	
	0.2% offset (ksi)	Strength (ksi)	Ultimate (-)	0.2% offset (ksi)	Stress (ksi)	at Ultimate (-)	K (ksi)	n (-)
SS304	34	84	0.54	34.07	129.36	0.432	162.41	0.27
A-533B	74	96	0.17	74.15	112.32	0.157	139.41	0.12
ABS-C	39	64	0.31	39.08	83.84	0.270	105.20	0.17

\*The power-law parameters in Table 2 were fitted for the current study where  $\bar{\sigma} = K\bar{\varepsilon}^n$  and  $\bar{\sigma}$ ,  $\bar{\varepsilon}$  are the effective true stress and effective total true strain, respectively.

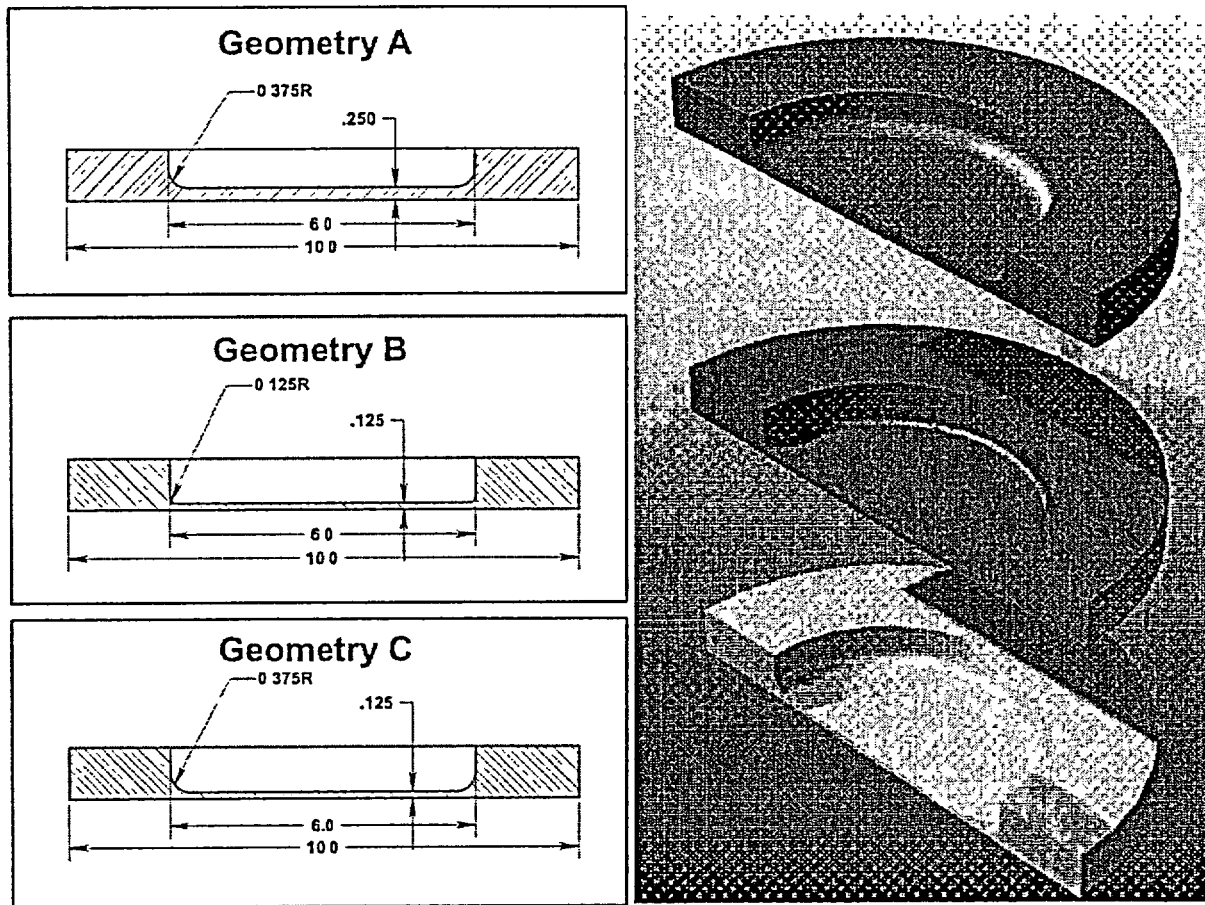


Fig. 2. Geometric descriptions of the three disk-burst specimens used in [1] (all dimensions are inches). Images on the right are Photoworks®-rendered views of 1/2-symmetry solid models of the three specimens.

## 2.2. Computational – Axisymmetric Discrete-Element and Finite-Element Models

The results of a computational study were presented in [2] in which the nine tests were simulated using the GAPL-3 computer code [3]. GAPL-3 applied the *discrete-element* method using a two-layered system of elements: one layer for the strain-displacement field and a second layer for the stress field to perform an elasto-plastic large-deformation analysis of stresses, strains, loads, and displacements of thin plates or axisymmetric shells with pressure loading. At each incremental load step, the code iterated to resolve both geometric and material nonlinearities, thus establishing a condition of static equilibrium. The GAPL-3 code did not account for the reduction in thickness of the diaphragm with increasing load, and, therefore, was unable to demonstrate the “tailing up” of the experimental center-deflection histories. As discussed in [2], the thin-shell approximation of the GAPL-3 code is not strictly valid in the fillet region. The GAPL-3 model did include a plastic-hinge type of strain redistribution, but the strain concentration effect due to the fillet radius was not accounted for, since the predicted strain distribution in the cross-section of the fillet was linear by assumption. These approximations in the analysis were driven by the limitations of the computer resources available at the time of the study in 1972.

The current study reanalyzed all nine disk-burst tests using the ABAQUS [4] finite-element code. With current computing power, many of the simplifying assumptions required in 1972 could be removed to provide a more detailed analysis. The fundamental assumptions made in the current study are:

- (1) the material is assumed to be homogenous and isotropic before and throughout plastic deformation;
- (2) the material is assumed to be free of pre-existing defects;
- (3) the volume of the material undergoing plastic deformation is assumed to be constant (i.e., incompressible with a Poisson’s ratio,  $\nu = 0.5$ ), for linear-elastic deformation  $\nu = 0.3$ ;
- (4) the hydrostatic component of the stress tensor has no effect on yielding; and
- (5) the plastic deformation follows incremental  $J_2$  flow theory (Mises yield criterion) with its associated flow rule (Levy-Mises) and isotropic strain hardening.

The finite-element meshes shown in Fig. 3 were developed using 8-node quadratic, axisymmetric, solid elements with reduced integration (ABAQUS element type CAX8R). The material property data given in Table 2 were used to fit power-law constitutive models for the plastic region of the three materials (see Fig. 4). The analyses applied a nonlinear finite-strain procedure with an incrementally increasing pressure load applied from zero up to the load at which numerical instabilities caused ABAQUS to abort the execution.

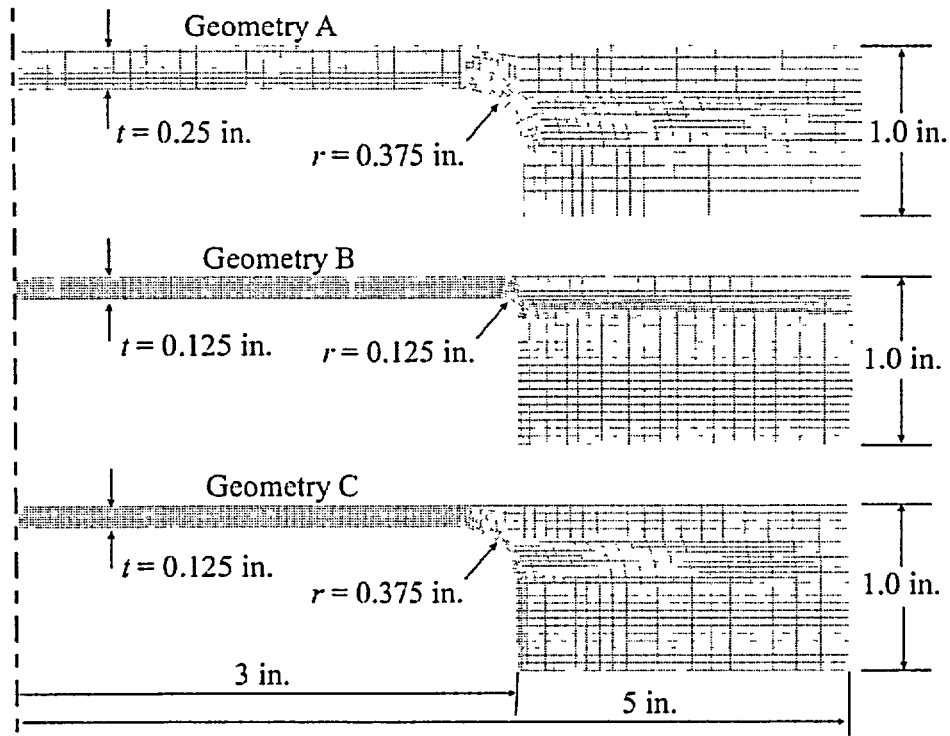


Fig. 3. Axisymmetric finite-element meshes used in the analyses of disk-burst tests reported in [2]. Quadratic 8-node axisymmetric (CAX8R) elements with reduced integration were used in a nonlinear finite-strain elastic-plastic analysis of the three disk-burst geometries with three materials.

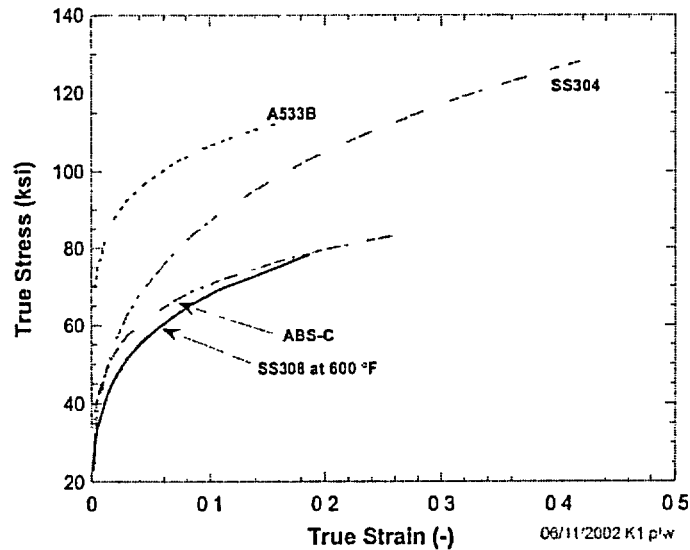


Fig. 4. True stress vs true strain curves of the three materials used in the disk-burst tests compared to SS308 at 600 °F. These three test material curves were developed using a power-law strain-hardening model fitted to yield and ultimate strength/strain data for each material given in [2]. (See Table 2).

### 2.3. Theory – Hill's Plastic Instability Theory

A plastic instability theory due to Hill [5] for a pressurized circular diaphragm constrained at the edges is presented in [7]. Figure 5 shows the geometry of the diaphragm, both undeformed and deformed, along with the nomenclature used in the development of the theory.

The geometry of deformation is assumed to be a spherical dome or bulge of radius,  $R$ . The undeformed ring element (defined by its position, width, and thickness,  $(r_0, \delta r_0, h_0)$ , respectively) is assumed to deform to an axisymmetric shell element with surface length,  $\delta L$ , deformed thickness,  $h$ , radial position,  $r$ , and angle  $\phi$ . The nonuniform thickness of the dome reaches its minimum at the pole with polar height  $H$ . For a spherical coordinate system with its origin at the center of the dome, the principal strains for the thin-shell (i.e., the strains are assumed constant through the thickness) element are

$$\varepsilon_\theta = \ln\left(\frac{r}{r_0}\right); \quad \varepsilon_\phi = \ln\left(\frac{\delta L}{\delta r_0}\right); \quad \varepsilon_h = \ln\left(\frac{h}{h_0}\right) \quad (1)$$

A geometric relationship exists between the radius and chord of a circle such that

$$R = \frac{H^2 + a^2}{2H} \quad (2)$$

where  $a$  is the effective radius of the undeformed diaphragm. Using Eqs. (1) - (2) and the geometry shown in Fig. 5, ref. [7] derives the following relations for the meridional,  $\varepsilon_\phi$ , and hoop,  $\varepsilon_\theta$ , strains at any point on the spherical bulge

$$\varepsilon_\phi(z|H, a) = \varepsilon_\theta(z|H, a) = \ln\left[1 + \left(\frac{zH}{a^2}\right)\right] \quad (3)$$

where the geometric parameter  $z$  is shown in Fig. 5. Applying the constant volume assumption, i.e.,  $\varepsilon_\phi + \varepsilon_\theta + \varepsilon_h = 0$ , produces the following equation for the radial ("thickness") strain

$$\varepsilon_h(z|H, a) = -2\varepsilon_\phi(z|H, a) = \ln\left[\frac{1}{1 + (zH/a^2)}\right]^2 \quad (4)$$

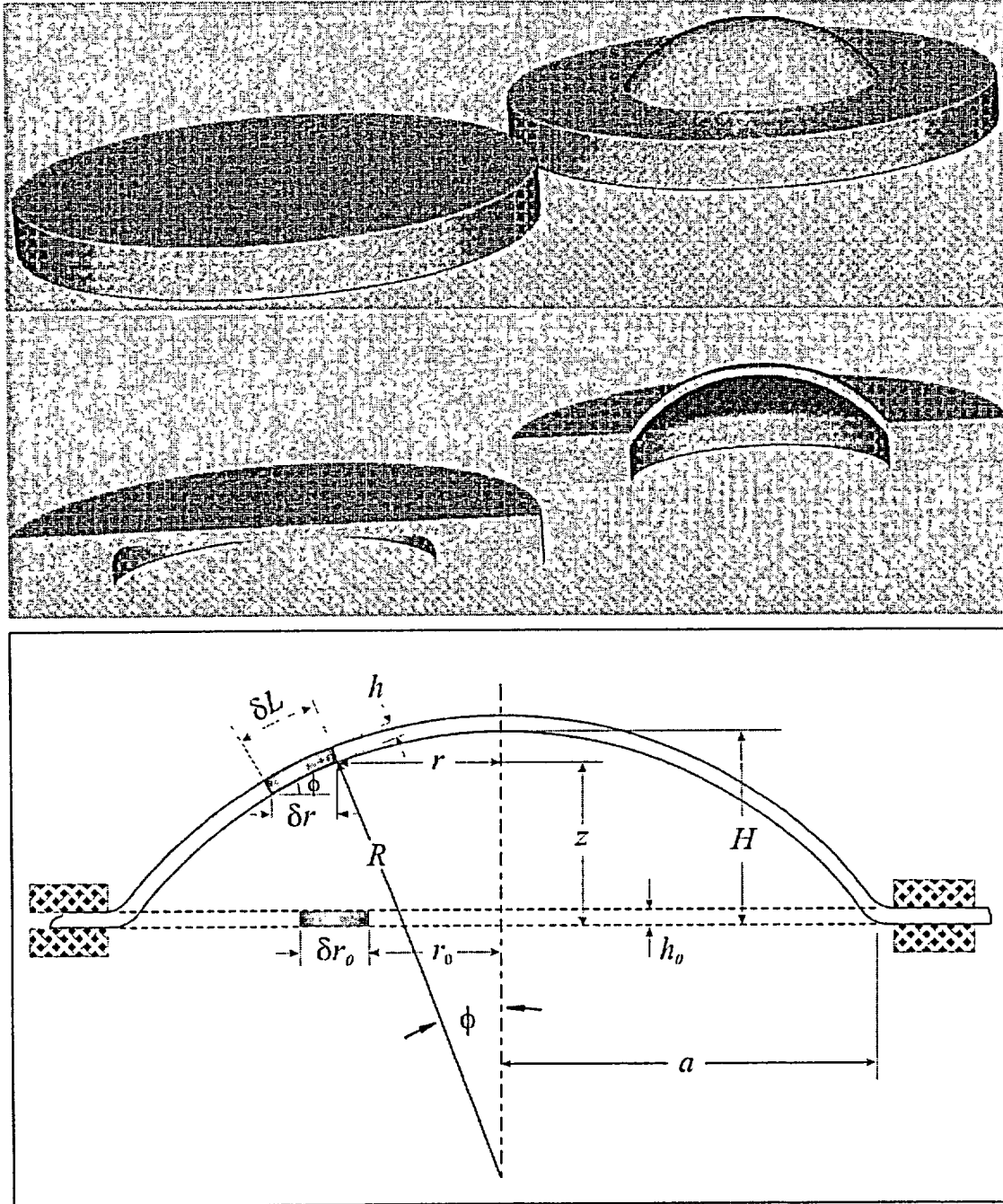


Fig. 5. Spherical geometry of deformation assumed in Hill's [5] plastic instability theory.

The effective strain then becomes

$$\bar{\varepsilon}(\varepsilon_\phi, \varepsilon_\theta, \varepsilon_h) \equiv \sqrt{\frac{2}{3}} \sqrt{(\varepsilon_\phi - \varepsilon_\theta)^2 + (\varepsilon_\phi - \varepsilon_h)^2 + (\varepsilon_\theta - \varepsilon_h)^2} = -\varepsilon_h(z|H, a) = 2 \ln \left[ 1 + \left( \frac{zH}{a^2} \right) \right] \quad (5)$$

The maximum radial strain, therefore, occurs at the pole of the spherical bulge. Applying the thin-walled assumption (which is not made in the computational finite-element model) for an axisymmetric shell element, the equilibrium relation between the meridional,  $\sigma_\phi$ , and hoop,  $\sigma_\theta$ , membrane stresses and the internal pressure,  $p_i$ , loading is

$$\frac{\sigma_\phi}{R_\phi} + \frac{\sigma_\theta}{R_\theta} = \frac{p_i}{h} \quad (6)$$

For a spherical dome,  $R_\phi = R_\theta = R$ , and a state of equibiaxial stress is assumed to prevail near the pole of the dome with the principal stresses being

$$\sigma_\phi = \sigma_\theta = \frac{p_i R}{2h}; \quad \sigma_r = 0 \quad (7)$$

and the effective stress,  $\bar{\sigma} = \frac{1}{\sqrt{2}} \sqrt{(\sigma_\phi - \sigma_\theta)^2 + (\sigma_\phi - \sigma_r)^2 + (\sigma_\theta - \sigma_r)^2}$ , is

$$\bar{\sigma} = \sigma_\phi = \sigma_\theta = \frac{p_i R}{2h} \quad (8)$$

To establish an instability criterion, a surface can be constructed in pressure, effective stress, and deformation/strain space by expressing Eq. (8) as a total differential of the form

$$\begin{aligned} R p_i &= 2 h \bar{\sigma} \\ R d p_i + p_i d R &= 2 h d \bar{\sigma} + 2 \bar{\sigma} d h \\ \frac{d p_i}{p_i} &= \frac{d \bar{\sigma}}{\bar{\sigma}} + \frac{d h}{h} - \frac{d R}{R} \end{aligned} \quad (9)$$

An unstable condition exists at a point of maximum pressure on the surface where  $d p_i = 0$ . The condition is unstable because any perturbation from this position always involves a reduction in load (pressure), even in a rising stress field. The instability criterion for a deformed bulge of radius  $R$  is, therefore, established by the following relation between stress and the deformed geometry for any point on the dome

$$\frac{d\bar{\sigma}}{\bar{\sigma}} = \frac{dR}{R} - \frac{dh}{h} \quad (10)$$

or in terms of effective strain

$$\frac{1}{\bar{\sigma}} \frac{d\bar{\sigma}}{d\bar{\epsilon}} = 1 + \frac{1}{R} \frac{dR}{d\bar{\epsilon}} \quad (11)$$

If the instability condition is attained, it will first occur at the point of maximum effective strain at the top of the dome (at  $z = H$ ) such that Eq. (11) can be stated as

$$\frac{1}{\bar{\sigma}} \frac{d\bar{\sigma}}{d\bar{\epsilon}} = \frac{3}{2} - \frac{1}{4} \left( \frac{2}{\bar{\epsilon}} \right) \left( 1 + \frac{\bar{\epsilon}}{2} \right) \quad (12)$$

Applying a power-law constitutive form to relate effective stress to effective strain in the plastic region,

$$\bar{\sigma} = K \bar{\epsilon}^n \quad , \quad (13)$$

the effective strain at instability is, after a great deal of algebraic manipulation,

$$\bar{\epsilon}_{crit} = \frac{4}{11} (2n + 1) \quad (14)$$

where  $n$  is the power-law exponent in the constitutive equation, Eq. (13).

An alternative instability criterion was developed by Chakrabarty and Alexander [6] which was based on a Tresca yield surface. The critical effective strain was found to be

$$\bar{\epsilon}_{crit} = \frac{2(2-n)(1+2n)}{11-4n} \quad (15)$$

For a given material and diaphragm geometry ( $n, a, h_0$ ), the pressure at the instability condition (i.e., the burst pressure) can be determined by the following procedure:

- Calculate the effective critical strain.  $\bar{\epsilon}_{crit} = \frac{4}{11}(2n+1)$
- Calculate the corresponding effective critical stress.  $\bar{\sigma}_{crit} = K \bar{\epsilon}^n$
- Calculate the critical thickness.  $h_{crit} = h_0 \exp(-\bar{\epsilon}_{crit})$
- Calculate the polar height at the critical condition.  $H_{crit} = a \sqrt{\exp\left(\frac{\bar{\epsilon}_{crit}}{2}\right) - 1}$
- Calculate the corresponding bulge curvature radius.  $R_{crit} = \frac{H_{crit}^2 + a^2}{2H_{crit}}$
- Finally, calculate the predicted burst pressure.  $p_{burst} = \frac{2h_{crit}\bar{\sigma}_{crit}}{R_{crit}}$

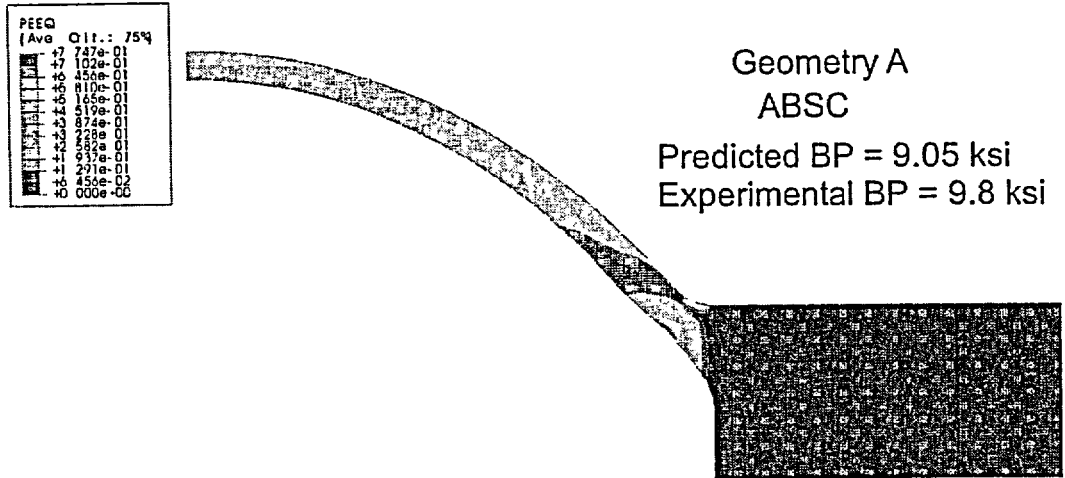
### 3. Stochastic Model Development

#### 3.1. Computational and Theoretical Model Results

Computational results using the GAPL-3 code were presented in [2]. Converged solutions were obtained for eight of the nine tests. Comparison of experimental and computational centerline deflections showed good agreement for the eight converged cases. In the nonconverged case (ABS-C, geometry C), some difficulty was reported in getting convergence at high pressures. In all cases the experimental data showed a “tailing up” as the pressure approached burst pressure, which the computational model was unable to capture. In general, the prediction of the burst pressure for the eight converged cases showed good agreement with the experimentally-determined burst pressures. Defining  $\alpha$  as the ratio of the experimental burst pressure to the computationally-predicted pressure at numerical instability, the mean for  $\alpha$  was 1.19 with a standard error for the mean of  $\pm 0.0484$  and a standard deviation for the sample of 0.137.

The finite-element models using ABAQUS were able to obtain burst pressures for all nine tests, where the *pressure at numerical instability*,  $P_{NI}$ , is defined as the pressure at which a breakdown occurs in the numerical procedure, causing the run to abort. For a nonlinear, finite-strain, static load step, ABAQUS uses automatic sizing of the load increment to maintain numerical stability. The number of iterations needed to find a converged solution for a load increment varies depending on the degree of nonlinearity in the system. If the solution has not converged within 16 iterations or if the solution appears to diverge, ABAQUS abandons the increment and starts again with the increment size set to 25% of its previous value. An attempt is then made at finding a converged solution with this smaller load increment. If the increment still fails to converge, ABAQUS reduces the increment size again. ABAQUS allows a maximum of five cutbacks in an increment before aborting the analysis. Therefore, ABAQUS will attempt a total of 96 iterations with six increments sizes before abandoning the solution. The initial load size for the failing increment was typically already very small due to difficulties in convergence with the previous and final successfully-converged load increment.

Equivalent plastic strain contours are shown in Fig. 4 for the geometry A (ABS-C carbon steel) specimen (Test No. 7) at the point of numerical instability. The experimental burst pressure for this specimen was 9.8 ksi, and numerical instability of the solution occurred at approximately 9.05 ksi, for an  $\alpha = 1.083$ . Highly localized plastic straining can be observed near the fillet, thus predicting an edge failure for this specimen which did in fact fail at its edge.



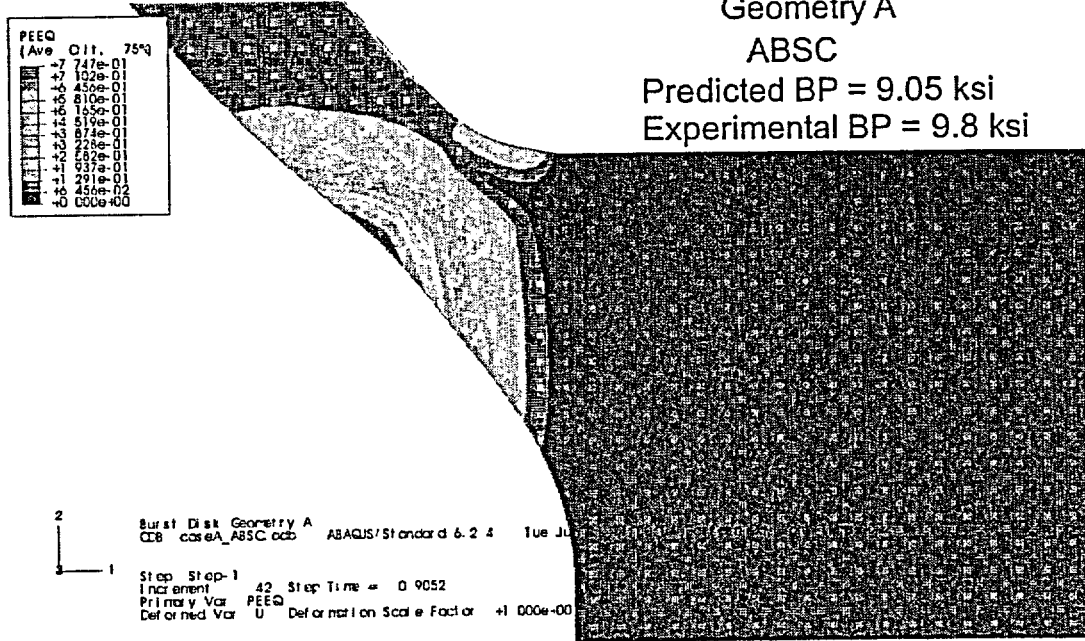
2  
1

Burst Disk Geometry A  
CEB caseA\_ABSC.cab ABAQUS/Standard 6.2.4 Tue Jun 11 11 00 04 Eastern Daylight Time 2002

Step Step-1  
Increment 42 Step Time = 0.9052  
Primary Var PEEQ  
Def or ned Var U Def or ned Var Scale Factor +1.000e+00

Ref. P. C. Riccardella, "Elasto-Plastic Analysis of Constrained Disk Burst Tests,"  
ASME Paper No 72-PVP-12, ASME Pressure Vessels and Piping Conference, New Orleans, LA, September 17-21, 1972.

(a)



2  
1

Burst Disk Geometry A  
CEB caseA\_ABSC.cab ABAQUS/Standard 6.2.4 Tue Jun 11 11 00 04 Eastern Daylight Time 2002

Step Step-1  
Increment 42 Step Time = 0.9052  
Primary Var PEEQ  
Def or ned Var U Def or ned Var Scale Factor +1.000e+00

(b)

Fig. 4. Equivalent plastic strain contours for the Geometry A (ABS-C carbon steel) specimen at the point of numerical instability. Highly localized plastic straining provides a precondition for plastic collapse at the edge of the specimen. (ABAQUS analysis results)

Figure 5 compares the predicted centerline deflection load histories with the experimentally-observed deflections at failure (estimated from Figs. 3 and 4 in [2]). The “tailing up” of the experimental deflection curves near the point of failure is predicted by the model, indicating that the computational simulations are capturing the final localized “necking” of the diaphragm. For the nine ABAQUS predictions, the mean for  $\alpha$  was 1.055 with a standard error for the mean of  $\pm 0.0331$  and a standard deviation for the sample of 0.0993.

The results of applying Hill’s failure criterion are presented in Table 3. The mean for  $\alpha$  was 1.058 with a standard error for the mean of  $\pm 0.0374$  and a standard deviation for the sample of 0.1123. The calculations were repeated using the theoretical critical strain of Chakrabarty and Alexander [6], Eq. (15), with the resulting burst pressures being essentially identical to those given in Table 3.

**Table 3. Application of Hill’s Instability Theory to Nine Disk-burst Tests**

Test	$K$ (ksi)	$n$	$a$ (in.)	$h_0$ (in.)	$\epsilon_{crit}$	$H_{crit}$ (in.)	$R_{crit}$ (in.)	$\sigma_{crit}$ (ksi)	$h_{crit}$ (in.)	$P_{NI}$ (ksi)	$P_{burst(exp)}$ (ksi)	$\alpha$
1	162.41	0.27	2.625	0.250	0.561	1.493	3.054	138.84	0.1427	12.98	15	1.156
2	162.41	0.27	2.875	0.125	0.561	1.635	3.345	138.84	0.0714	5.92	6.8	1.148
3	162.41	0.27	2.625	0.125	0.561	1.493	3.054	138.84	0.0714	6.49	7.7	1.187
4	139.41	0.12	2.625	0.250	0.449	1.316	3.276	126.96	0.1596	12.37	11	0.889
5	139.41	0.12	2.875	0.125	0.449	1.441	3.588	126.96	0.0798	5.65	5.3	0.938
6	139.41	0.12	2.625	0.125	0.449	1.316	3.276	126.96	0.0798	6.19	6.7	1.083
7	105.20	0.17	2.625	0.250	0.490	1.383	3.183	92.95	0.1532	8.95	9.8	1.095
8	105.20	0.17	2.875	0.125	0.490	1.514	3.486	92.95	0.0766	4.08	3.75	0.918
9	105.20	0.17	2.625	0.125	0.490	1.383	3.183	92.95	0.0766	4.47	4.94	1.104

A summary of all 26  $P_{NI}$  values is given in Table 4. Combining the 26 cases into a single sample gives a mean for  $\alpha$  of 1.098 with a standard error for the mean of  $\pm 0.0251$  and a standard deviation for the sample of 0.1281. Even though Hill’s theory is applicable only for center failures, the good agreement between the experiments (including those that failed at the edges) suggests that, for the edge-failure cases, the specimens were also close to a condition of plastic collapse at the center when they failed first at the edge.

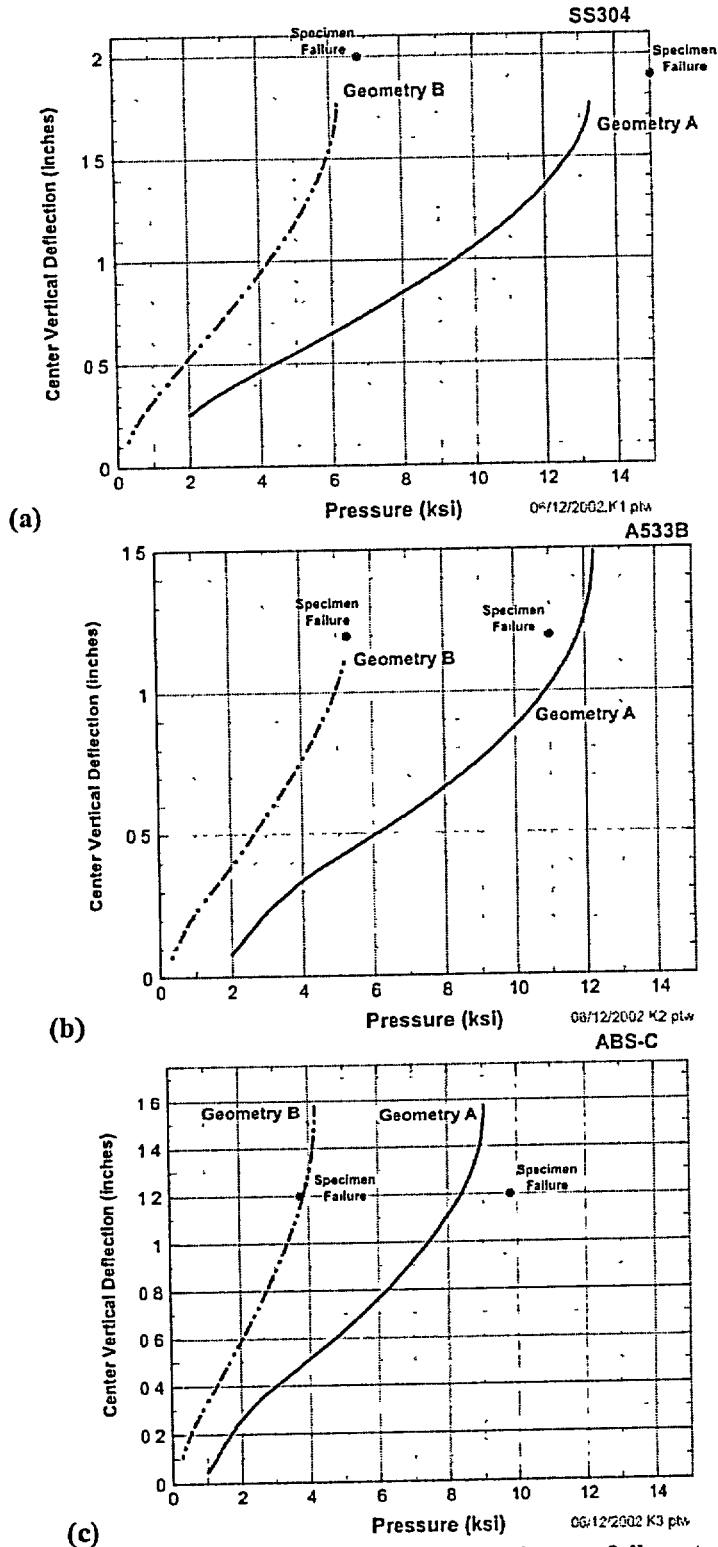
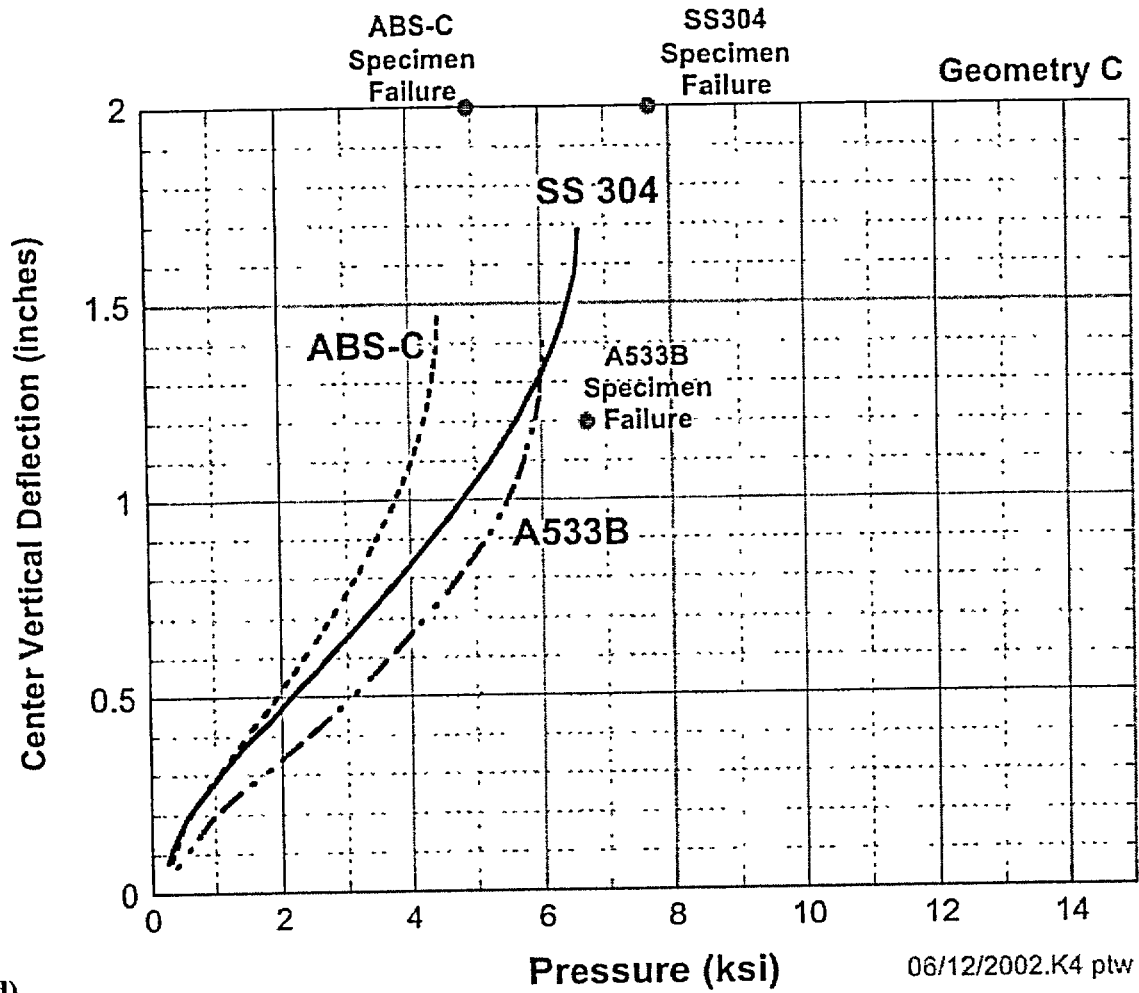


Fig. 5. Comparison of experimental centerline vertical deflections at failure to ABAQUS FEM vertical deflection histories at the center of the Geometry A and B specimens for (a) SS 304, (b) A533-B, and (c) ABS-C materials, and



(d) Fig. 5. (continued) (d) ABAQUS FEM vertical deflection histories at the center of Geometry C, all three materials compared to specimen failure.

**Table 4. Comparison of Experimental Burst Pressures to Three Predictions**

Test Number	Material	Geometry	Experimental		Riccardella's ASME Paper			Hill's Plastic Instability Theory			ABAQUS Solutions		
			Burst Pressure (BP) (ksi)	Location of Failure	Pressure at Instability ( $P_M$ ) (ksi)	Location of Failure	Exp. BP $P_M$	Pressure at Instability ( $P_M$ ) (ksi)	Location of Failure	Exp. BP $P_M$	Pressure at Instability ( $P_M$ ) (ksi)	Location of Failure	Exp. BP $P_M$
1	SS 304	A	15	Edge	12.3	Edge	1.22	12.98	Center	1.16	13.29	Edge	1.13
2		B	6.8	Center	4.8	Edge	1.42	5.92	Center	1.15	6.22	Edge	1.09
3		C	7.7	Center	7.4	Center	1.04	6.49	Center	1.19	6.59	Center	1.17
4	A533B	A	11	Edge	9.8	Edge	1.12	12.37	Center	0.89	12.26	Edge	0.90
5		B	5.3	Edge	4.2	Edge	1.26	5.65	Center	0.94	5.24	Edge	1.01
6		C	6.7	Center	6.8	Center	0.99	6.19	Center	1.08	6.03	Edge	1.11
7	ABS-C	A	9.8	Edge	8	Edge	1.23	8.95	Center	1.10	9.05	Edge	1.08
8		B	3.75	Edge	3	Edge	1.25	4.08	Center	0.92	4.19	Edge	0.89
9		C	4.94	Edge				4.47	Center	1.10	4.46	Edge/Center	1.11

### 3.2. Development of Stochastic Model of Failure

The development of several stochastic models is described in this section in which the uncertainties associated with predictions of burst pressure for circular diaphragms using computational or analytical methods are estimated. It is postulated that the trends observed in the ratios of experimentally-observed failure pressures in the nine disk-burst tests in [2] to calculated  $P_M$  values will be representative of the predictive accuracy of computational estimates of the burst pressure in the Davis-Besse wastage-area problem. Given a calculated  $P_M$  for a specific configuration of the wastage area, the scaled stochastic models will provide estimates of the cumulative probability that the true burst pressure will be less than a given service pressure, specifically providing a failure pressure with its associated probability. This postulated linkage of the test specimens to the Davis-Besse problem is obviously an approximation, since the wastage area footprints are not identical to the circular diaphragms used in the tests. The appropriateness of this linkage is in part, therefore, dependent on the ability of the finite-element models to capture, as accurately as is feasible and based on the best current knowledge, the actual geometry of the wastage area footprint. Accurate material properties are also an important input to the analysis.

Table 5 summarizes some descriptive statistics for the ratio,  $\alpha$ , of experimental burst pressure to the calculated pressure at numerical instability for the three predictive methods discussed in the previous section. Also shown in the table are the results of combining the three samples into one larger sample of 26 data points. This combined sample was used to develop the stochastic models with  $\alpha$  treated as a random variate. Combining the three sets into a single sample produced a sample size large enough to make a reasonably thorough statistical analysis of a range of continuous distributions feasible. Also given in Table 6 is a ranking of the 26 data points where the median rank order statistic is

$$P_{(i)} = \frac{i - 0.3}{n + 0.4} \quad (16)$$

The *Expert Fit*<sup>®</sup> [9] computer program was used to develop several stochastic models of the sample data presented in Table 6. Using a combination of heuristic criteria and *Goodness of Fit* statistics, twenty-six continuous distributions were tested with the results shown in ranked order in Table 7. The point-estimation procedures noted in Table 7 include *Maximum Likelihood (ML)*, *Method of Moments (MM)*, and *Quantile Estimates*. Table 8 compares three *Goodness of Fit* statistics (Anderson-Darling,  $\chi^2$ , and Kolmogorov-Smirnoff (*K-S*)) for the top six distributions. None of these distributions were rejected by the *Goodness of Fit* tests, and all received an absolute rating of *Good* by the *Expert Fit*<sup>®</sup> computer program. The remaining twenty distributions investigated were either rejected by one or more of the *Goodness of Fit* tests at some significance level and/or received a less than *Good* heuristic absolute rating by the

*Expert Fit*® software. Figure 6 shows a density/histogram overplot of the six candidate continuous distributions.

**Table 5. Descriptive Statistics for the Ratio of Experimental Burst Pressure to Predicted Burst Pressures**

Descriptive Statistics	Riccardella (1972)	Hill's Theory	ABAQUS	Combined
Sample Size	8	9	9	26
Mean	1.1902	1.0576	1.0549	1.0975
Standard Error	0.0484	0.0374	0.0331	0.0251
Median	1.2223	1.0953	1.0939	1.1057
Standard Deviation	0.1368	0.1123	0.0993	0.1281
Sample Variance	0.0187	0.0126	0.0099	0.0164
Kurtosis	-0.0506	-1.4799	-0.4349	0.2593
Skewness	0.0007	-0.5892	-0.9683	0.1714
Range	0.4314	0.2979	0.2739	0.5277
Minimum	0.9853	0.8889	0.8943	0.8889
Maximum	1.4167	1.1868	1.1682	1.4167
Confidence Level(95.0%)	0.1144	0.0863	0.0764	0.0517

**Table 6. Combined Sample Used in Development of Stochastic Model**

Rank	Method	Material	Geometry	$\alpha$	Order Statistic
1	Hill's Theory	A533B	A	0.8889	0.0265
2	ABAQUS Soln.	ABS-C	B	0.8943	0.0644
3	ABAQUS Soln.	A533B	A	0.8972	0.1023
4	Hill's Theory	ABS-C	B	0.9180	0.1402
5	Hill's Theory	A533B	B	0.9382	0.1780
6	Riccardella (1972)	A533B	C	0.9853	0.2159
7	ABAQUS Soln.	A533B	B	1.0119	0.2538
8	Riccardella (1972)	SS 304	C	1.0405	0.2917
9	ABAQUS Soln.	ABS-C	A	1.0827	0.3295
10	Hill's Theory	A533B	C	1.0829	0.3674
11	ABAQUS Soln.	SS 304	B	1.0939	0.4053
12	Hill's Theory	ABS-C	A	1.0953	0.4432
13	Hill's Theory	ABS-C	C	1.1042	0.4811
14	ABAQUS Soln.	ABS-C	C	1.1072	0.5189
15	ABAQUS Soln.	A533B	C	1.1104	0.5568
16	Riccardella (1972)	A533B	A	1.1224	0.5947
17	ABAQUS Soln.	SS 304	A	1.1288	0.6326
18	Hill's Theory	SS 304	B	1.1479	0.6705
19	Hill's Theory	SS 304	A	1.1560	0.7083
20	ABAQUS Soln.	SS 304	C	1.1682	0.7462
21	Hill's Theory	SS 304	C	1.1868	0.7841
22	Riccardella (1972)	SS 304	A	1.2195	0.8220
23	Riccardella (1972)	ABS-C	A	1.2250	0.8598
24	Riccardella (1972)	ABS-C	B	1.2500	0.8977
25	Riccardella (1972)	A533B	B	1.2619	0.9356
26	Riccardella (1972)	SS 304	B	1.4167	0.9735

\*  $\alpha$  = Experimental Burst Pressure/Pressure at Numerical Instability

**Table 7. Continuous Distributions Investigated – Ranked by Goodness of Fit**

Model	Parameters	Point Estimator	Parameter Values
1 - Log-Laplace	Location	Default	0
	Scale	ML estimate	1.1057
	Shape	ML estimate	11.45441
2 - Beta	Lower endpoint	MOM estimate	0.61449
	Upper endpoint	MOM estimate	1.78866
	Shape #1	MOM estimate	7.95564
	Shape #2	MOM estimate	11.38552
3 - Gamma	Location	Default	0
	Scale	ML estimate	0.01444
	Shape	ML estimate	76.01293
4 - Log-Logistic	Location	Default	0
	Scale	ML estimate	1.09586
	Shape	ML estimate	15.21867
5 - Normal	Mean	ML estimate	1.09747
	Standard Dev.	ML estimate	0.12811
6 - Weibull	Location	Default	0
	Scale	ML estimate	1.15383
	Shape	ML estimate	9.03948
7 - Lognormal	Location	Default	0
	Scale	ML estimate	0.08641
	Shape	ML estimate	0.11516
8 - Random Walk	Location	Default	0
	Scale	ML estimate	0.92335
	Shape	ML estimate	69.18788
9 - Inverse Gaussian	Location	Default	0
	Scale	ML estimate	1.09747
	Shape	ML estimate	82.23451
10 - Pearson Type V	Location	Default	0
	Scale	ML estimate	81.42582
	Shape	ML estimate	75.1846
11 - Inverted Weibull	Location	Default	0
	Scale	ML estimate	1.02827
	Shape	ML estimate	8.88835
12 - Weibull(E)	Location	Quantile estimate	0.88884
	Scale	ML estimate	0.21562
	Shape	ML estimate	1.15868
13 - Rayleigh(E)	Location	Quantile estimate	0.88884
	Scale	ML estimate	0.24352
14 - Erlang(E)	Location	Quantile estimate	0.88884
	Scale	ML estimate	0.20862
	Shape	ML estimate	1
15 - Gamma(E)	Location	Quantile estimate	0.88884
	Scale	ML estimate	0.21819
	Shape	ML estimate	0.95616
16 - Exponential(E)	Location	ML estimate	0.8889
	Scale	ML estimate	0.20857
17 - Pearson Type VI(E)	Location	Quantile estimate	0.88884
	Scale	Default	1
	Shape #1	ML estimate	1.00117

Model	Parameters	Point Estimator	Parameter Values
18 - Lognormal(E)	Shape #2	ML estimate	5.43892
	Location	Quantile estimate	0.88884
	Scale	ML estimate	-2.17414
19 - Random Walk(E)	Shape	ML estimate	1.86865
	Location	Quantile estimate	0.88884
	Scale	ML estimate	699.32509
20 - Pareto(E)	Shape	ML estimate	4.82644
	Location	ML estimate	0.8889
	Shape	ML estimate	4.8976
21 - Chi-Square	Location	Quantile estimate	0.88884
	d.f.	ML estimate	0.72313
22 - Wald	Location	Default	0
	Shape	ML estimate	48.03951
23 - Rayleigh	Location	Default	0
	Scale	ML estimate	1.10463
24 - Exponential	Location	Default	0
	Scale	ML estimate	1.09747
25 - Wald(E)	Location	Quantile estimate	0.88884
	Shape	ML estimate	1.43E-03
26 - Inverse Gaussian(E)	Location	Quantile estimate	8.89E-04
	Scale	ML estimate	0.20862
	Shape	ML estimate	1.44E-03

**Table 8. Continuous Distributions That Passed All Goodness of Fit Tests**

Rank	Model	Relative Score	Rating	Anderson-Darling	$\chi^2$ Statistic	K-S
1	Log-Laplace	98	Good	0.44952	2.15385	0.59218
2	Beta	93	Good	0.44697	4.92308	0.81037
3	Gamma	89	Good	0.46050	3.53846	0.81894
4	Normal	83	Good	0.39325	1.23077	0.74664
5	Random Walk	75	Good	0.50448	3.53846	0.85840
6	Inverse Gaussian	71	Good	0.50514	3.53846	0.85891

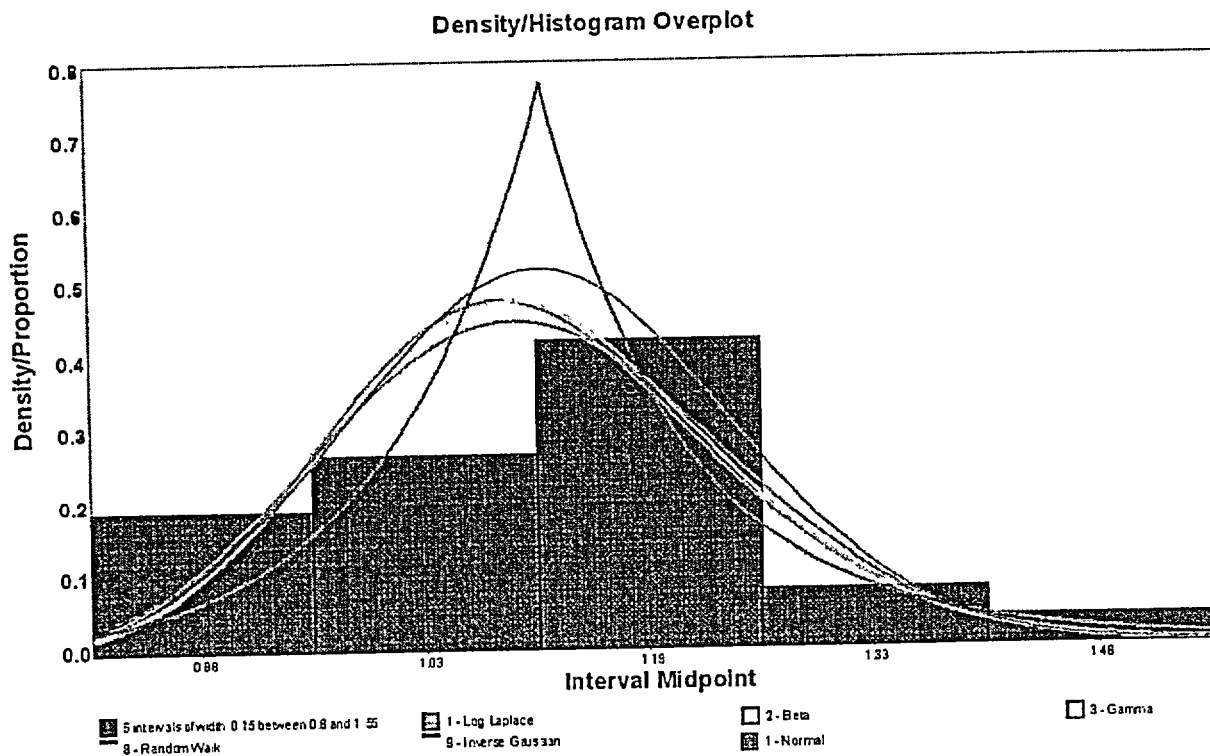


**Fig. 6. Overplot of probability densities with histogram for fitted stochastic models.**

The six distributions in Table 8 have the following analytical forms:

### Log-Laplace Distribution

The Log-Laplace distribution has the highest relative ranking among the twenty-six distributions investigated. The general three-parameter Log-Laplace continuous distribution has the following probability density function,  $f_{LP}$ , and cumulative distribution function,  $F_{LP}$ ,

$$f_{LP}(x|a,b,c) = \begin{cases} \frac{c}{2b} \left(\frac{x-a}{b}\right)^{c-1} & \text{for } a < x < b \\ \frac{c}{2b} \left(\frac{x-a}{b}\right)^{-c-1} & \text{for } x \geq b \end{cases} \quad \text{for } a \geq 0, (b,c) > 0$$

$$\Pr(X \leq x) = F_{LP}(x|a,b,c) = \begin{cases} \frac{1}{2} \left(\frac{x-a}{b}\right)^c & \text{for } a < x < b \\ 1 - \frac{1}{2} \left(\frac{x-a}{b}\right)^{-c} & \text{for } x \geq b \end{cases} \quad \text{for } a \geq 0, (b,c) > 0$$
(17)

where  $a$  is the location parameter,  $b$  is the scale parameter, and  $c$  is the shape parameter.

### Beta Distribution

The Beta distribution has the following probability density function,  $f_{Be}$ , and cumulative distribution function,  $F_{Be}$ ,

$$f_{Be}(x|a,b,\alpha_1,\alpha_2) = \begin{cases} \frac{\left(\frac{x-a}{b-a}\right)^{\alpha_1-1} \left[1 - \left(\frac{x-a}{b-a}\right)\right]^{\alpha_2-1}}{(b-a)B(\alpha_1,\alpha_2)} & \text{for } a < x < b \\ 0 & \text{otherwise} \end{cases}$$

$$F_{Be}(x|a,b,\alpha_1,\alpha_2) = \begin{cases} \int_a^x f_{Be}(\xi|a,b,\alpha_1,\alpha_2) d\xi & \text{for } a < x < b \\ 0 & \text{otherwise} \end{cases}$$
(18)

where  $B(\alpha_1,\alpha_2) = \int_0^1 u^{\alpha_1-1} (1-u)^{\alpha_2-1} du$ ,  $a$  is the lower endpoint,  $b$  is the upper endpoint,  $\alpha_1$  is the first shape parameter, and  $\alpha_2$  is the second shape parameter.

### Gamma Distribution

The Gamma distribution has the following probability density function,  $f_{Ga}$ , and cumulative distribution function,  $F_{Ga}$ ,

$$f_{Ga}(x|\alpha, \beta, \gamma) = \begin{cases} \frac{(x-\gamma)^{\alpha-1}}{\beta^\alpha \Gamma(\alpha)} \exp\left[-\left(\frac{x-\gamma}{\beta}\right)\right] & \text{for } x > \gamma \\ 0 & \text{otherwise} \end{cases} \quad (19)$$

$$F_{Ga}(x|\alpha, \beta, \gamma) = \begin{cases} \int_{\gamma}^x f_{Ga}(\xi|\alpha, \beta, \gamma) d\xi & \text{for } x > \gamma \\ 0 & \text{otherwise} \end{cases}$$

where  $\alpha$  is the shape parameter,  $\beta$  is the scale parameter,  $\gamma$  is the location parameter, and  $\Gamma(x) = \int_0^{\infty} \exp(-u)u^{x-1} du$ .

### Normal Distribution

The Normal distribution has the following probability density function,  $f_N$ , and cumulative distribution function,  $F_N$ ,

$$f_N(x|\mu, \sigma) = \frac{1}{\sqrt{2\pi\sigma^2}} \exp\left[\frac{-(x-\mu)^2}{2\sigma^2}\right] \quad \text{for all real numbers } x \quad (20)$$

$$F_N(x|\mu, \sigma) = \Phi(z) = \int_{-\infty}^z f_N(\xi|0,1)d\xi \quad \text{for } z = (x-\mu)/\sigma$$

where  $\mu$  is the mean (location parameter) and  $\sigma$  is the standard deviation (scale parameter).

### Random Walk Distribution

The Random Walk distribution has the following probability density function,  $f_{RW}$ , and cumulative distribution function,  $F_{RW}$

$$f_{RW}(x | \alpha, \beta, \gamma) = \begin{cases} \left( \frac{\alpha}{2\pi(x-\gamma)} \right)^{1/2} \exp \left\{ \frac{-\alpha[1-\beta(x-\gamma)]^2}{2\beta^2(x-\gamma)} \right\} & \text{for } x > \gamma \\ 0 & \text{otherwise} \end{cases} \quad (21)$$

$$F_{RW}(x | \alpha, \beta, \gamma) = \begin{cases} \Phi \left\{ - \left[ \frac{1}{\beta(x-\gamma)} - 1 \right] \sqrt{\alpha(x-\gamma)} \right\} - \\ \exp \left( \frac{2\alpha}{\beta} \right) \Phi \left\{ - \left[ \frac{1}{\beta(x-\gamma)} + 1 \right] \sqrt{\alpha(x-\gamma)} \right\} & \text{for } x > \gamma \\ 0 & \text{otherwise} \end{cases}$$

where  $\alpha$  is the shape parameter,  $\beta$  is the scale parameter,  $\gamma$  is the location parameter, and  $\Phi$  is defined in Eq. (20).

### Inverse Gaussian Distribution

The Inverse Gaussian distribution has the following probability density function,  $f_{IG}$ , and cumulative distribution function,  $F_{IG}$

$$f_{IG}(x | \alpha, \beta, \gamma) = \begin{cases} \left[ \frac{\alpha}{2\pi(x-\gamma)^3} \right]^{1/2} \exp \left[ \frac{-\alpha(x-\gamma-\beta)^2}{2\beta^2(x-\gamma)} \right] & \text{for } x > \gamma \\ 0 & \text{otherwise} \end{cases} \quad (22)$$

$$F_{IG}(x | \alpha, \beta, \gamma) = \begin{cases} \Phi \left[ \left( \frac{x-\gamma}{\beta} - 1 \right) \sqrt{\frac{\alpha}{x-\gamma}} \right] + \exp \left[ \frac{2\alpha}{\beta} \right] \Phi \left[ - \left( \frac{x-\gamma}{\beta} + 1 \right) \sqrt{\frac{\alpha}{x-\gamma}} \right] & \text{for } x > \gamma \\ 0 & \text{otherwise} \end{cases}$$

where  $\alpha$  is the shape parameter,  $\beta$  is the scale parameter,  $\gamma$  is the location parameter, and  $\Phi$  is defined in Eq. (20).

Figures 7 and 8 compare the probabilities and the cumulative distribution functions, respectively, of the top-three ranked models.

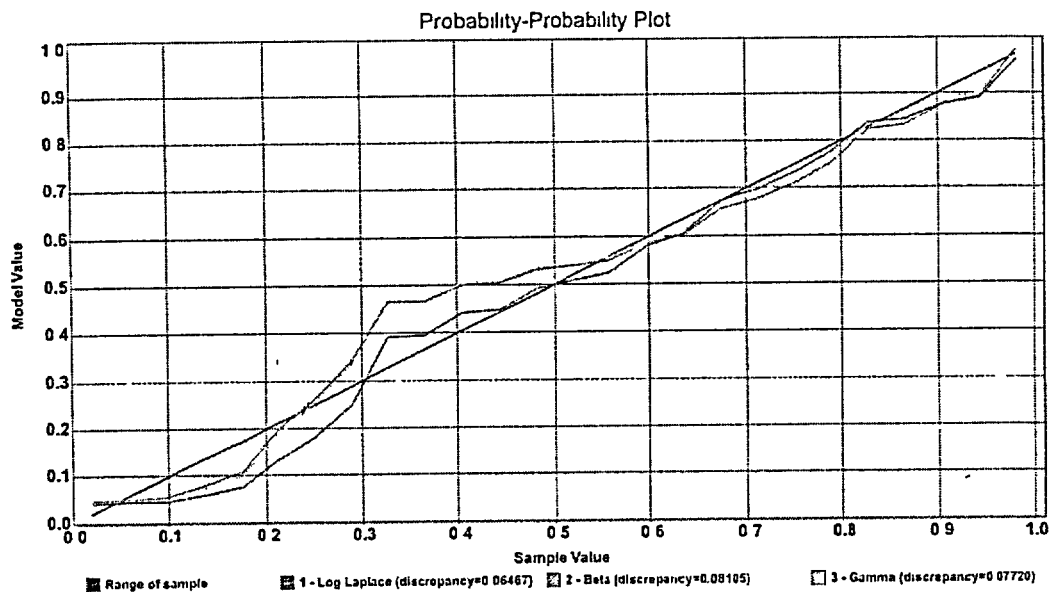


Fig. 7. Probability-probability plot comparing top three fitted distributions.

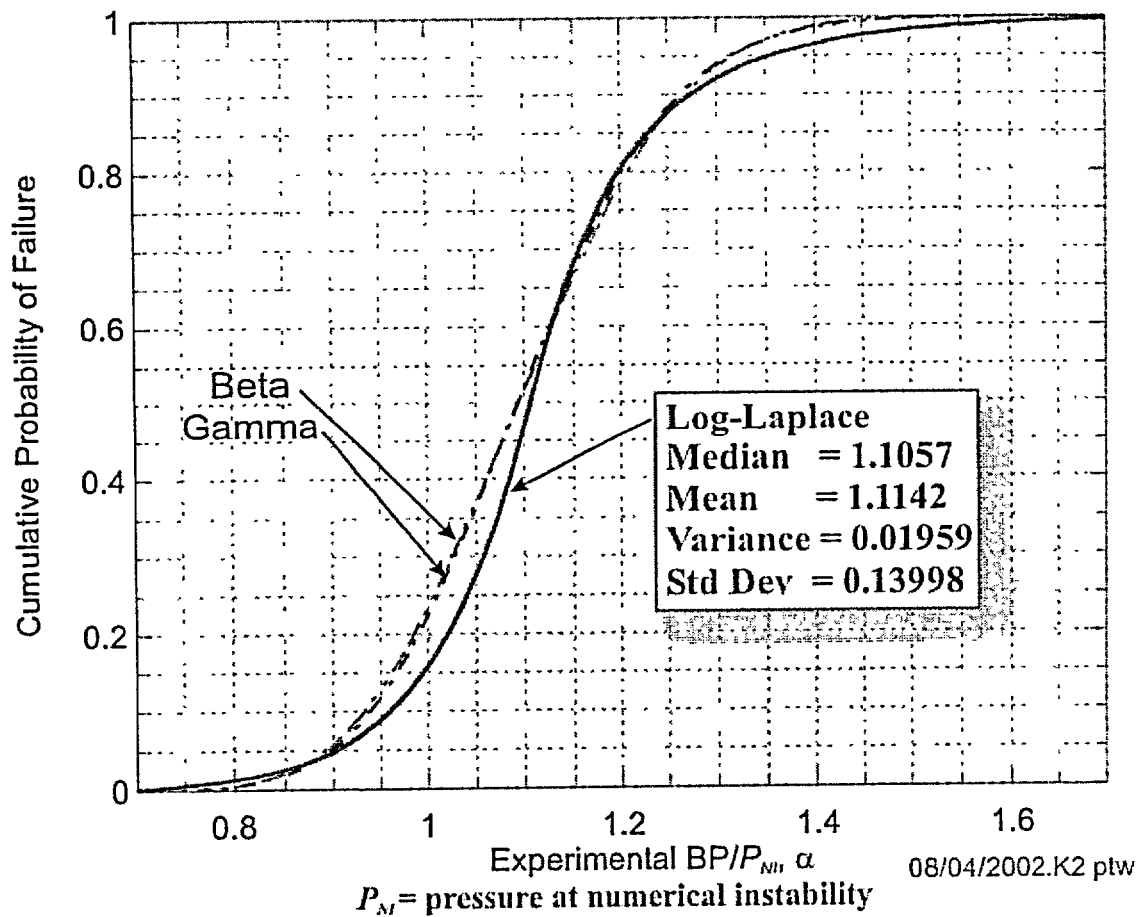


Fig. 8. Log-Laplace statistical failure model ( $n = 26$ ) compared to a beta and gamma cumulative distribution functions.

As a specific example from the *Expert Fit*<sup>®</sup> [9] analysis, the Log-Laplace stochastic model of failure has the following form

$$f_{LP}(\alpha | 0, 1.1057, 11.45441) = \begin{cases} 5.17971 \left( \frac{\alpha}{1.1057} \right)^{10.45441} & ; 0 < \alpha < 1.1057 \\ 5.17971 \left( \frac{\alpha}{1.1057} \right)^{-12.45441} & ; \alpha \geq 1.1057 \end{cases} \quad (23)$$

$$\Pr(X \leq \alpha) = F_{LP}(\alpha | 0, 1.1057, 11.45441) = \begin{cases} \frac{1}{2} \left( \frac{\alpha}{1.1057} \right)^{11.45441} & ; 0 < \alpha < 1.1057 \\ 1 - \frac{1}{2} \left( \frac{\alpha}{1.1057} \right)^{-11.45441} & ; \alpha \geq 1.1057 \end{cases}$$

where  $\alpha$  is the ratio of the true (but unknown) burst pressure to the calculated pressure at numerical instability,  $P_M$ . The percentile function is given by

$$Q_{LP}(p | 0, 1.1057, 11.45441) = \alpha_p = \begin{cases} \exp \left[ \ln(1.1057) + \frac{\ln(2p)}{11.45441} \right] & ; p \leq 0.5 \\ \exp \left[ \ln(1.1057) - \frac{\ln[2(1-p)]}{11.45441} \right] & ; p > 0.5 \end{cases} \quad \text{for } (0 < p < 1) \quad (24)$$

The stochastic models in Table 8 can be used to provide statistical estimates of the expected predictive accuracy of computational methods applied to burst pressure calculations for service pressures within the range of the data used to develop the model, i.e.,  $0.8889 \times P_M \leq SP \leq 1.4167 \times P_M$ , where,  $SP$ , is a service pressure, and  $P_M$  is the calculated pressure at numerical instability for the condition under investigation. Extrapolating significantly beyond the range of the data becomes somewhat problematic due to the small sample size of twenty-six data points. All six models in Table 8 are plausible candidates to describe the population from which the sample in Table 6 was drawn, but the relative ranking of these distributions may be sensitive to sample size. Due to the small sample size ( $n = 26$ ) used in the stochastic model development, no definitive claim can be made that one distribution is significantly superior to the other five; however, the Log-Laplace is shown to have the highest ranking given the available data, and it produces the highest failure probabilities when extrapolating to service pressures well below the range of the data, e.g., to the nominal operating pressure or safety-valve set-point pressure.

Table 9 provides an example of the sensitivity of the fitting process to the sample size for the case of the “as-found” cavity condition (to be discussed in the next section). Normal distributions were fitted to two samples from the predictions of the disk-burst tests: (1) the ABAQUS finite-element results ( $n = 9$ ) and

(2) the combined data set ( $n = 26$ ). The two stochastic models were then scaled by the calculated  $P_M$  of 6.65 ksi for the “as-found” condition. Extrapolating beyond the range of the data for the “as-found” case study produces approximately three orders-of-magnitude difference in estimated failure probability at the operating pressure of 2.165 ksi. This difference in estimated failure probability decreases as the service pressure increases towards the range of data used to develop the models.

**Table 9. Sensitivity of Cumulative Probability of Failure to Sample Size:  
“As-Found” Condition (see Sect. 4)**

Internal Pressure (ksi)	Normal Distribution	
	ABAQUS $n=9$	Combined $n=26$
6.65	0.2902	0.2233
2.155	1.04E-12	7.81E-10
2.165	1.17E-12	8.40E-10
2.200	1.53E-13	1.08E-09
2.225	2.02E-13	1.30E-09
2.250	2.68E-13	1.55E-09
2.275	3.53E-13	1.85E-09
2.300	4.66E-13	2.21E-09
2.325	6.13E-13	2.64E-09
2.350	8.05E-13	3.14E-09
2.375	1.06E-12	3.75E-09
2.400	1.39E-12	4.46E-09
2.425	1.81E-12	5.30E-09
2.450	2.37E-12	6.30E-09
2.475	3.09E-12	7.48E-09
2.500	4.03E-12	8.87E-09

#### 4. Application of Stochastic Model to Bounding Calculation

A bounding calculation was carried out for the “as-found” condition of the wastage area in the Davis-Besse head. The finite-element model used in the analysis is shown in Fig. 9. An adjusted stress-strain curve (see Fig. 10) was constructed to lower-bound the available data [10, 11] for the cladding material. The geometry of the wastage area footprint was taken from Fig. 13 in the *Root Cause Analysis Report* [12]. As an estimate of the uncertainty in the current wastage area measurements, the footprint was extended by approximately 0.25 inches (see Table 10 and Fig. 11 for a geometric description of the adjusted footprint). A uniform cladding thickness of 0.24 inches (the minimum cladding thickness value based on ultrasonic testing (UT) measurements on a ½ inch grid as depicted in Fig. 14 of ref. [12]) was assumed in the model. The finite-element model was then loaded with increasing pressure until the point of numerical instability at an internal pressure of 6.65 ksi (see Fig. 12) was attained. Decreasing the cladding thickness from 0.24 inches to 0.1825 inches (the minimum design allowable) resulted in a calculated pressure at numerical instability of 5.18 ksi. In the following, an example is provided of how the statistical distributions in Table 8 can be scaled and applied to the analysis of failure of the cladding in the wastage area.

As an example, the Log-Laplace statistical failure model can be scaled to provide estimates of cumulative probability of failure (or probability of nonexceedance) as a function of internal service pressure for the specific condition of the wastage area simulated by the finite-element analysis. The scaled Log-Laplace model (see Fig. 13) has the following form

$$f_{LP}(SP | P_{NI}) = \begin{cases} 5.17971 \left( \frac{SP}{1.1057 \times P_{NI}} \right)^{10.45441} & ; 0 < SP < 1.1057 \times P_{NI} \\ 5.17971 \left( \frac{SP}{1.1057 \times P_{NI}} \right)^{-12.45441} & ; SP \geq 1.1057 \times P_{NI} \end{cases} \quad (25)$$

$$\Pr(BP_{(true)} \leq SP) = F_{LP}(SP | P_{NI}) = \begin{cases} \frac{1}{2} \left( \frac{SP}{1.1057 \times P_{NI}} \right)^{11.45441} & ; 0 < SP < 1.1057 \times P_{NI} \\ 1 - \frac{1}{2} \left( \frac{SP}{1.1057 \times P_{NI}} \right)^{-11.45441} & ; SP \geq 1.1057 \times P_{NI} \end{cases}$$

where,  $SP$ , is the service pressure under consideration,  $P_{NI}$  is the calculated *pressure at numerical instability*, and  $BP_{(true)}$  is the unknown true burst pressure. To calculate as estimated burst (failure) pressure,  $BP_p$ , with probability,  $p$ , the scaled percentile function is applied

$$Q_{LP}(p | 0, 1.1057 \times P_{NI}, 11.45441) = \quad (26)$$

$$BP_p = \begin{cases} \exp \left[ \ln(1.1057 \times P_{NI}) + \frac{\ln(2p)}{11.45441} \right] & ; p \leq 0.5 \\ \exp \left[ \ln(1.1057 \times P_{NI}) - \frac{\ln[2(1-p)]}{11.45441} \right] & ; p > 0.5 \end{cases} \quad \text{for } (0 < p < 1)$$

**Table 10. Wastage-Area-Footprint Geometry Data**

Description	Scaling Factor	Area (in <sup>2</sup> )	Perimeter (in)	Centroid of Wastage Area Footprint		Moments of Inertia About the Centroid			Eigenvalue Extraction for Principal Moments and Directions			
				$x_c$ (in)	$y_c$ (in)	$I_x$ (in <sup>4</sup> )	$I_y$ (in <sup>4</sup> )	$I_{xy}$ (in <sup>4</sup> )	Principal Moments		Principal Directions	
									$I_1$ (in <sup>4</sup> )	$I_2$ (in <sup>4</sup> )	$\langle n_1, n_2 \rangle$	$\langle n_1', n_2' \rangle$
As-Found Footprint	1	35.36	30.36	16.4122	-0.1194	98.89	9699.33	-117.16	75.26	197.41	$\langle 0.9004, -0.4351 \rangle$	$\langle -0.4351, 0.9004 \rangle$
Adjusted Footprint for Bounding Calculation	0.25 in	40.06	31.78	16.4301	-0.1255	129.02	11031.81	-141.35	99.00	245.71	$\langle 0.8943, -0.4476 \rangle$	$\langle -0.4476, 0.8943 \rangle$

Footprint centroid is in global coordinates  
 Global coordinate system has its z-axis aligned with the vertical centerline of the vessel.  
 The x-y plane of the global coordinate system is a horizontal plane  
 with the x-axis along the line between the centerlines of Nozzles 3 and 11

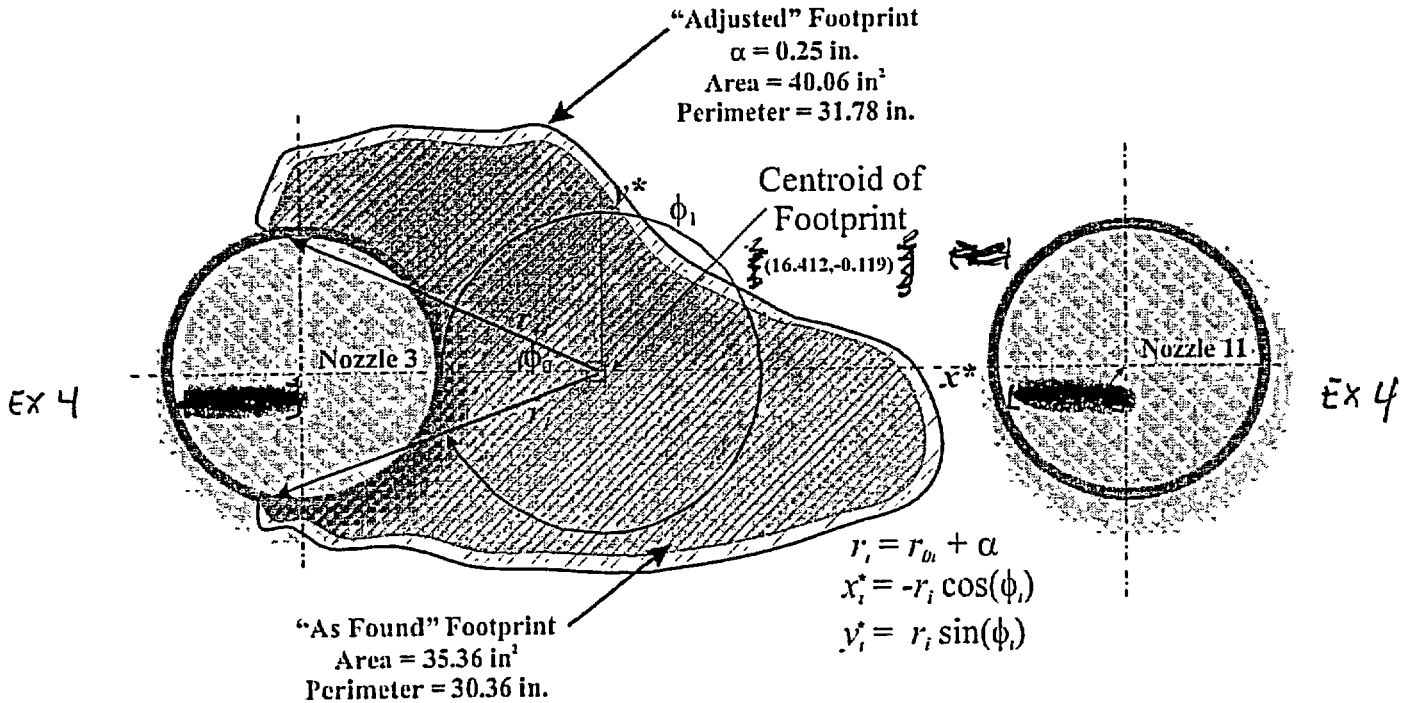
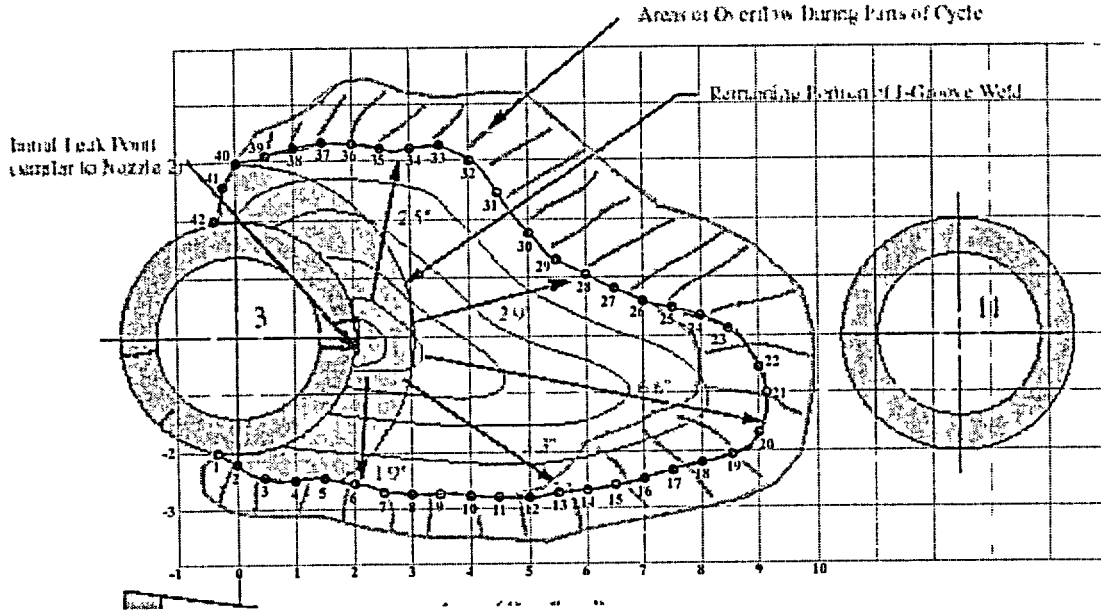


Table 10 (continued) Details of Wastage Area Footprint Before Adjustment for Bounding Calculation (Figure taken from Fig. 13 ref. [12])



Point	x"	y"	Point	x"	y"
0	-0.639	-1.895	24	8.000	0.334
1	-0.334	-2.280	25	7.500	0.483
2	0.000	-2.235	26	7.000	0.582
3	0.500	-2.492	27	6.500	0.829
4	1.000	-2.522	28	6.000	1.046
5	1.500	-2.482	29	5.500	1.303
6	2.000	-2.581	30	5.000	1.778
7	2.500	-2.730	31	4.500	2.460
8	3.000	-2.769	32	4.000	3.023
9	3.500	-2.759	33	3.500	3.300
10	4.000	-2.789	34	3.000	3.221
11	4.500	-2.819	35	2.500	3.250
12	5.000	-2.819	36	2.000	3.300
13	5.500	-2.759	37	1.500	3.349
14	6.000	-2.700	38	1.000	3.240
15	6.500	-2.621	39	0.500	3.122
16	7.000	-2.512	40	0.000	3.000
17	7.500	-2.364	41	-0.210	2.578
18	8.000	-2.216	42	-0.364	2.000
19	8.500	-2.087	43	-0.242	1.985
20	9.000	-1.712			
21	9.135	-1.000			
22	9.000	-0.555			
23	8.500	0.137			

Origin of local coordinate system located at centerline of Nozzle 3. (inches)

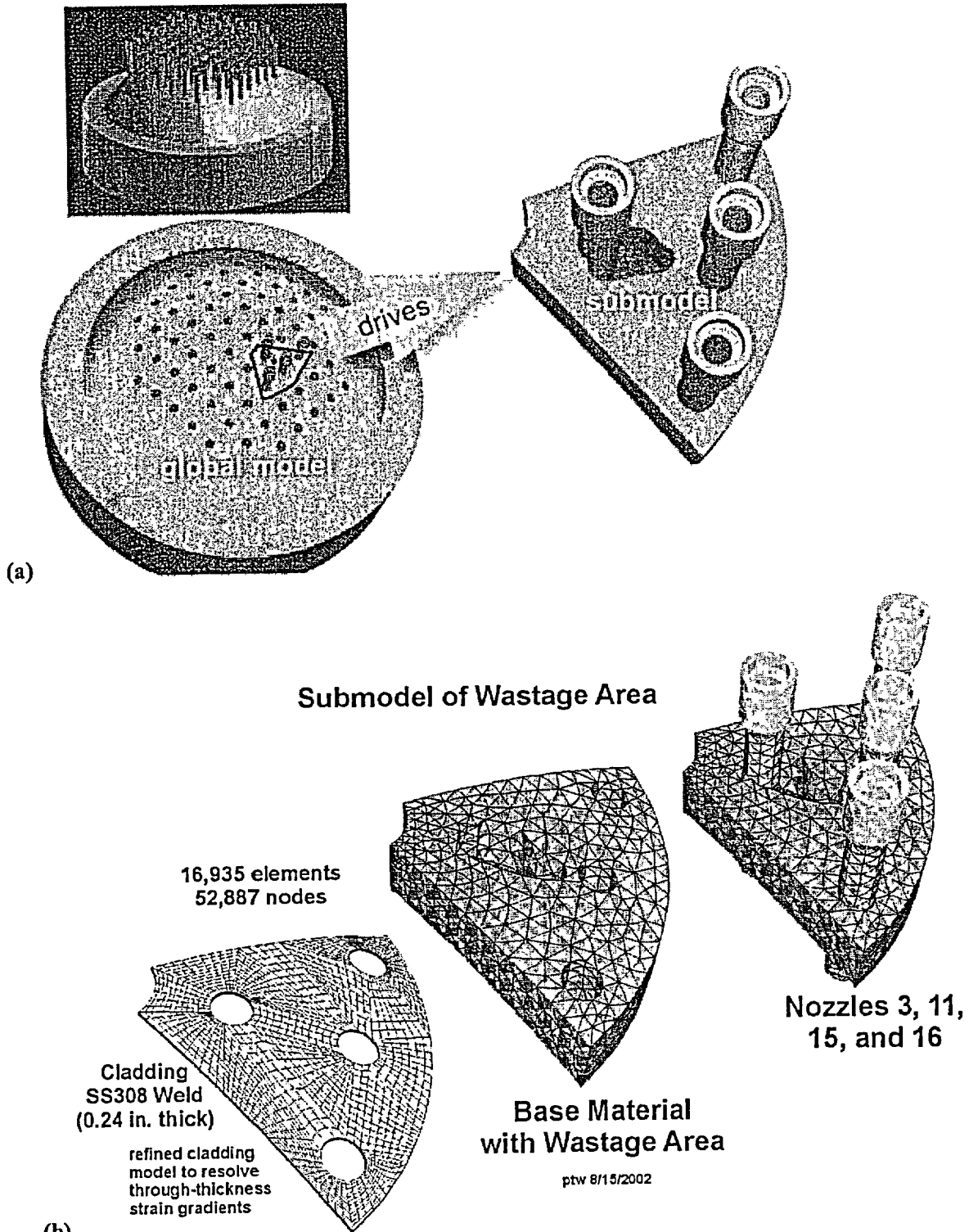


Fig. 9. Finite-element global and submodels of the Davis-Besse head and wastage area. The displacements at the vertical side boundaries of the submodel are driven by the global model. Both models are exposed to the same internal pressure loading.

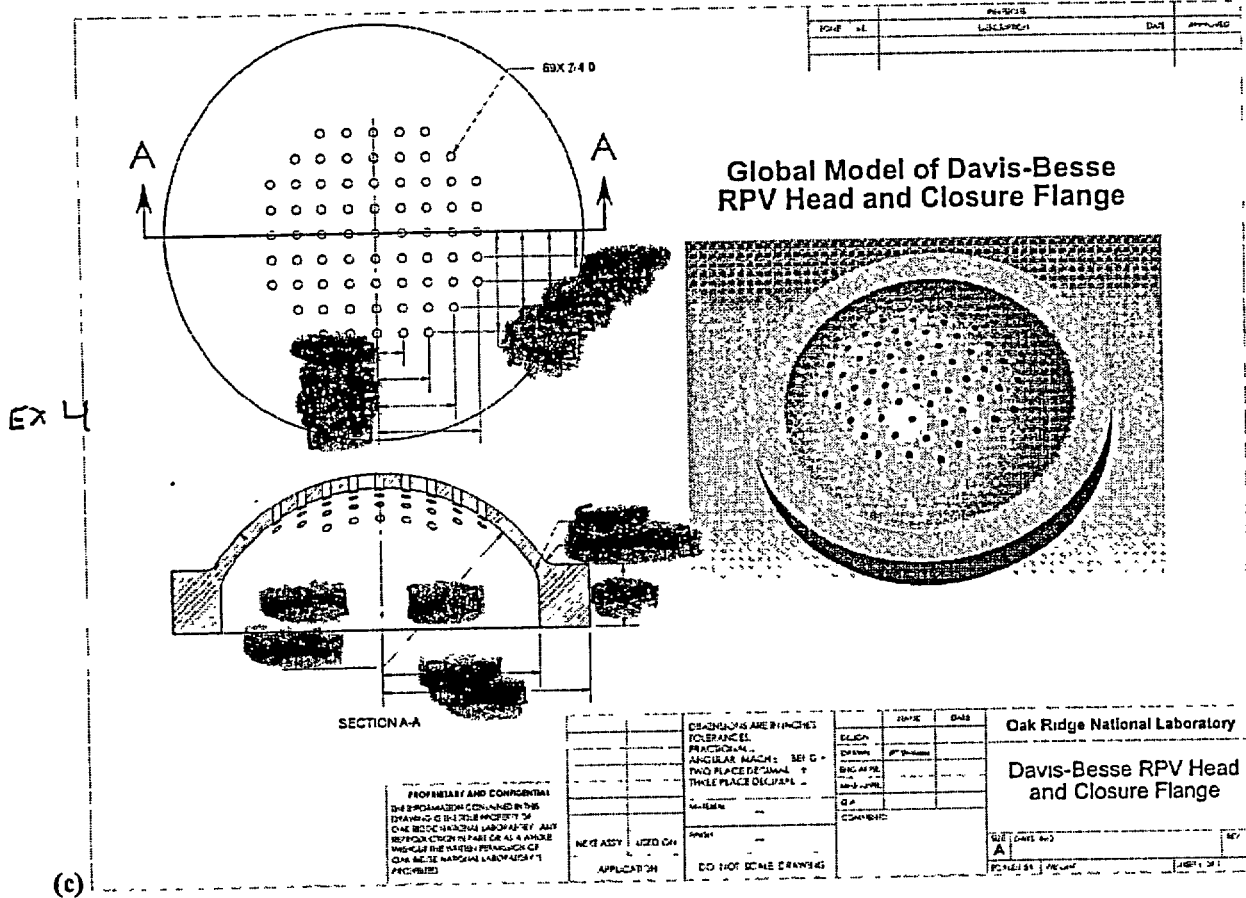
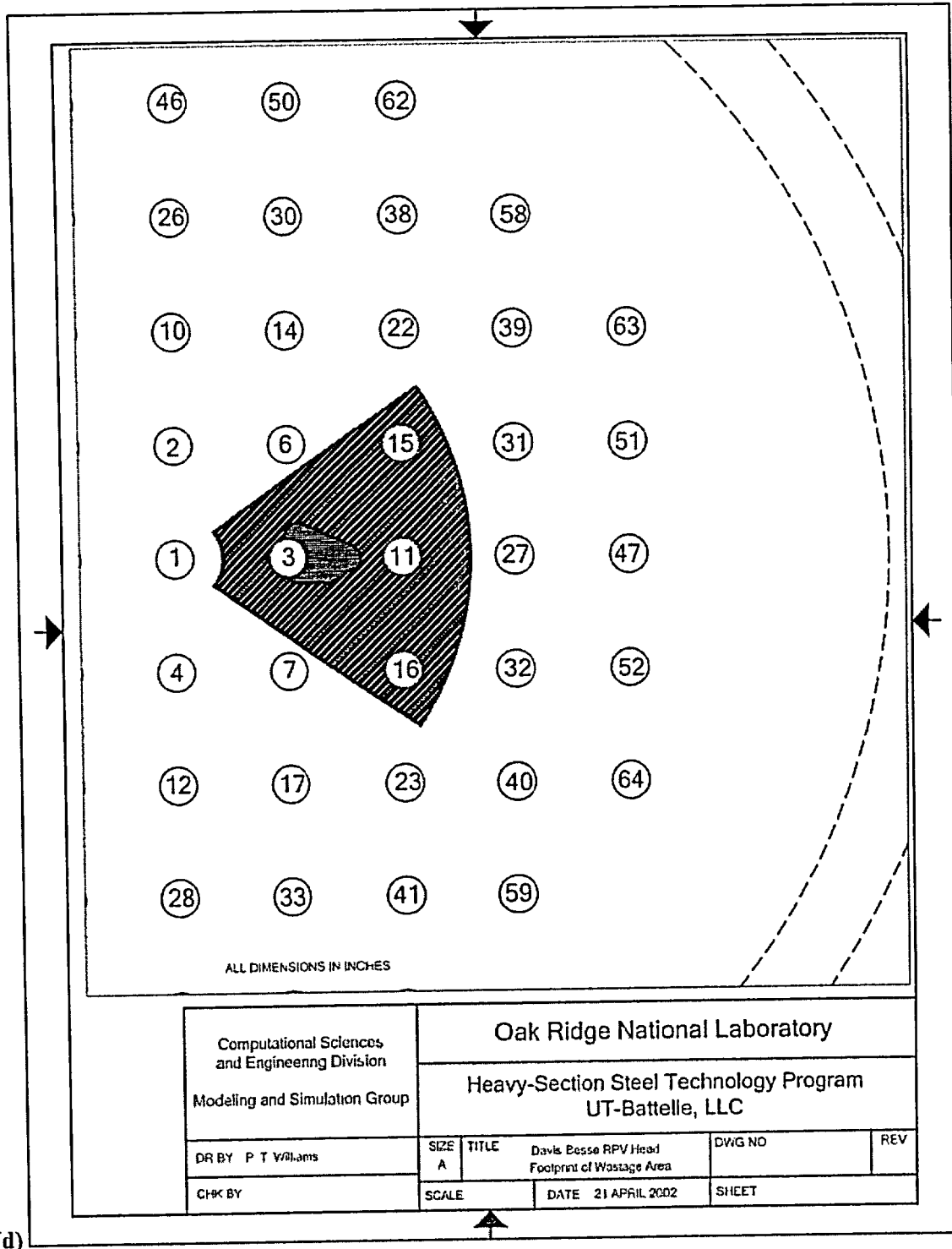


Fig 9. (continued) (c) geometry of RPV head and closure flange used in global model,



(d)

Fig 9. (continued) (d) relative location of submodel within full RPV head,

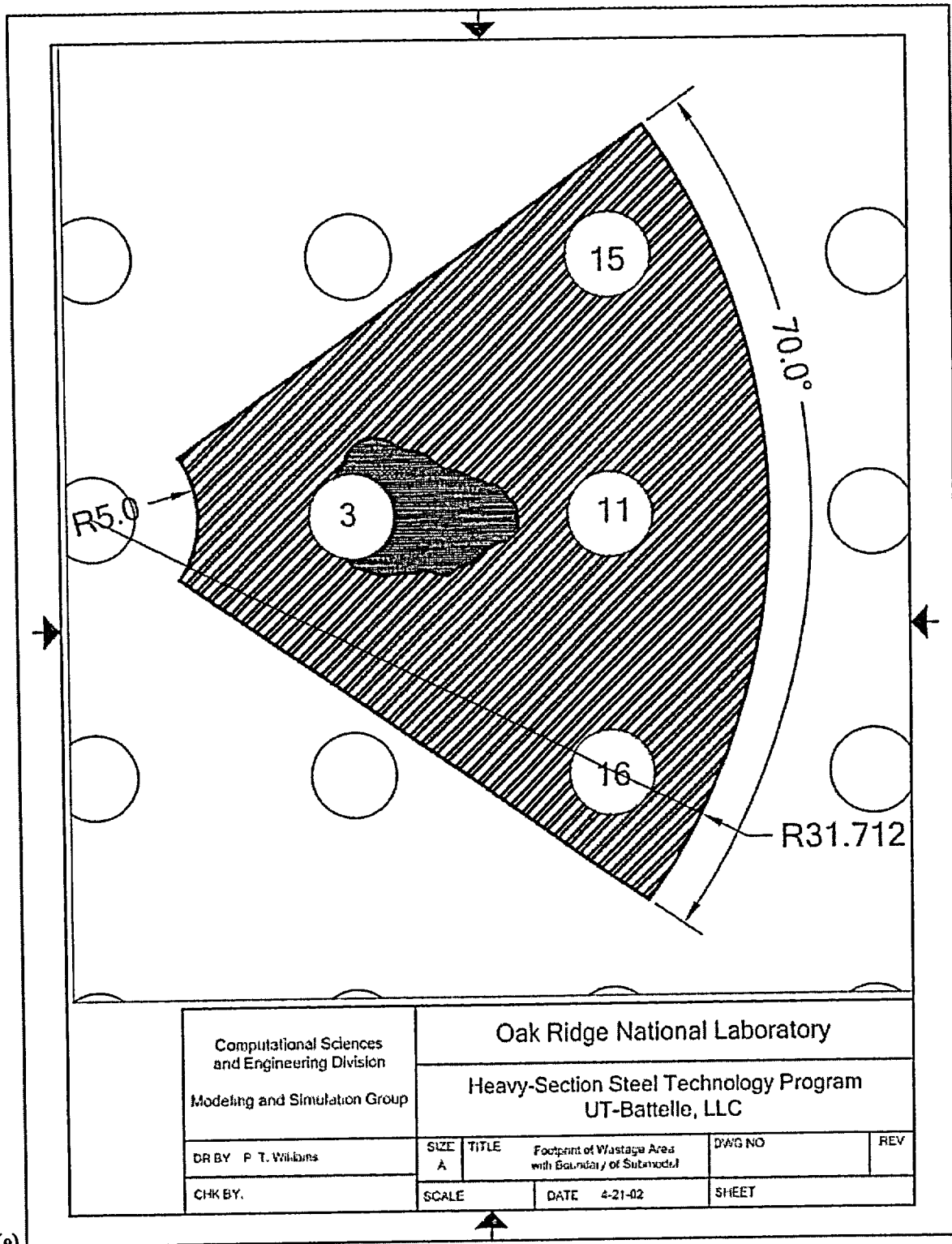


Fig 9. (continued) (e) geometry of submodel relative to Nozzles 3, 11, 15, and 16.

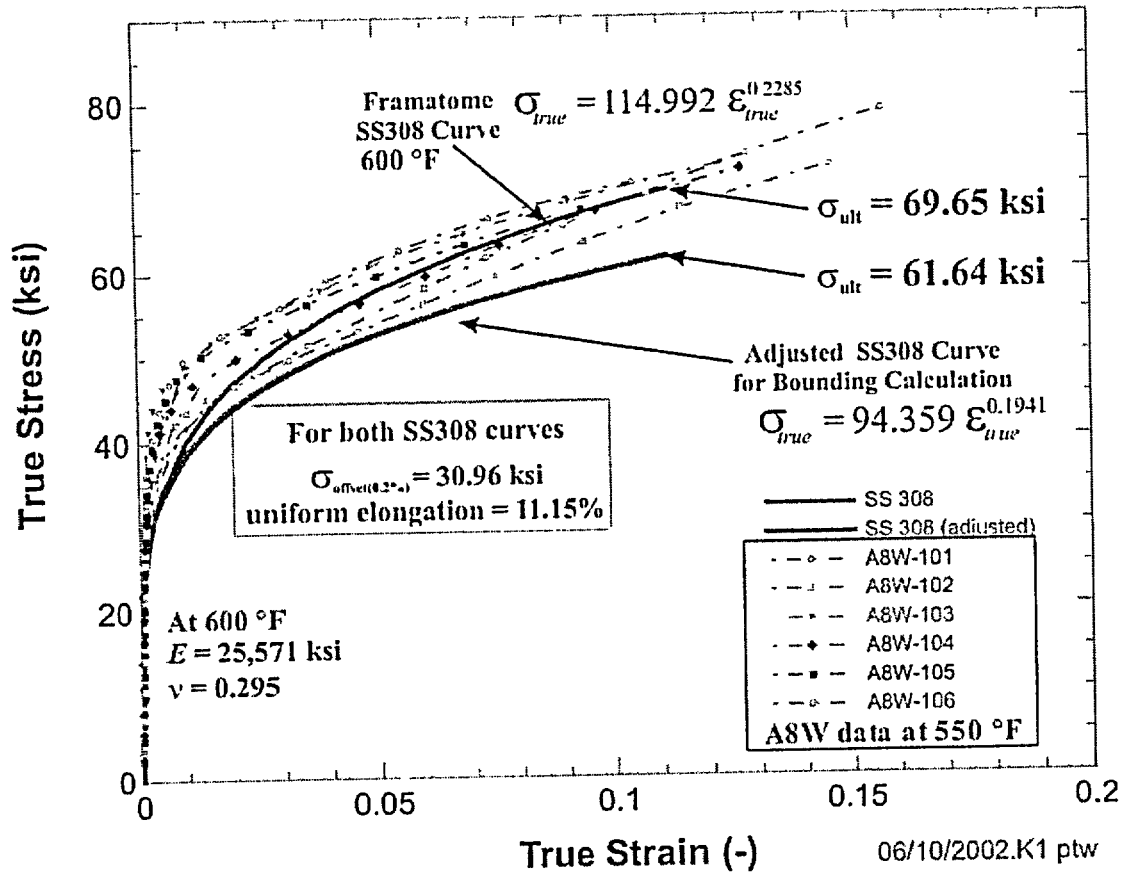
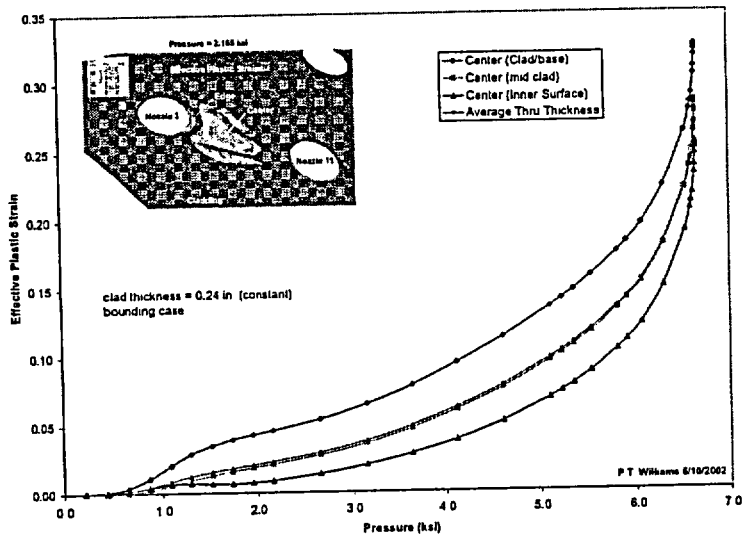
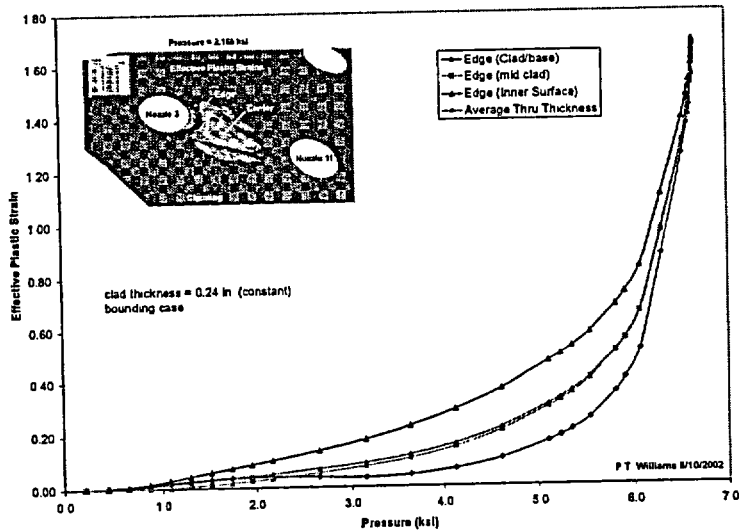


Fig. 10. Adjusted SS308 stress vs. strain curve used in the bounding-case calculations compared to curves from a range of A8W heats. Strain hardening in the adjusted curve was reduced to lower-bound all of the data. The offset yield strength and strain at ultimate strength were retained from the unadjusted SS308 curve received from Framatome.





(a)



(b)

Fig. 12. Effective plastic-strain histories at two high-strain locations in the wastage area: (a) near the center and (b) near Nozzle 3.

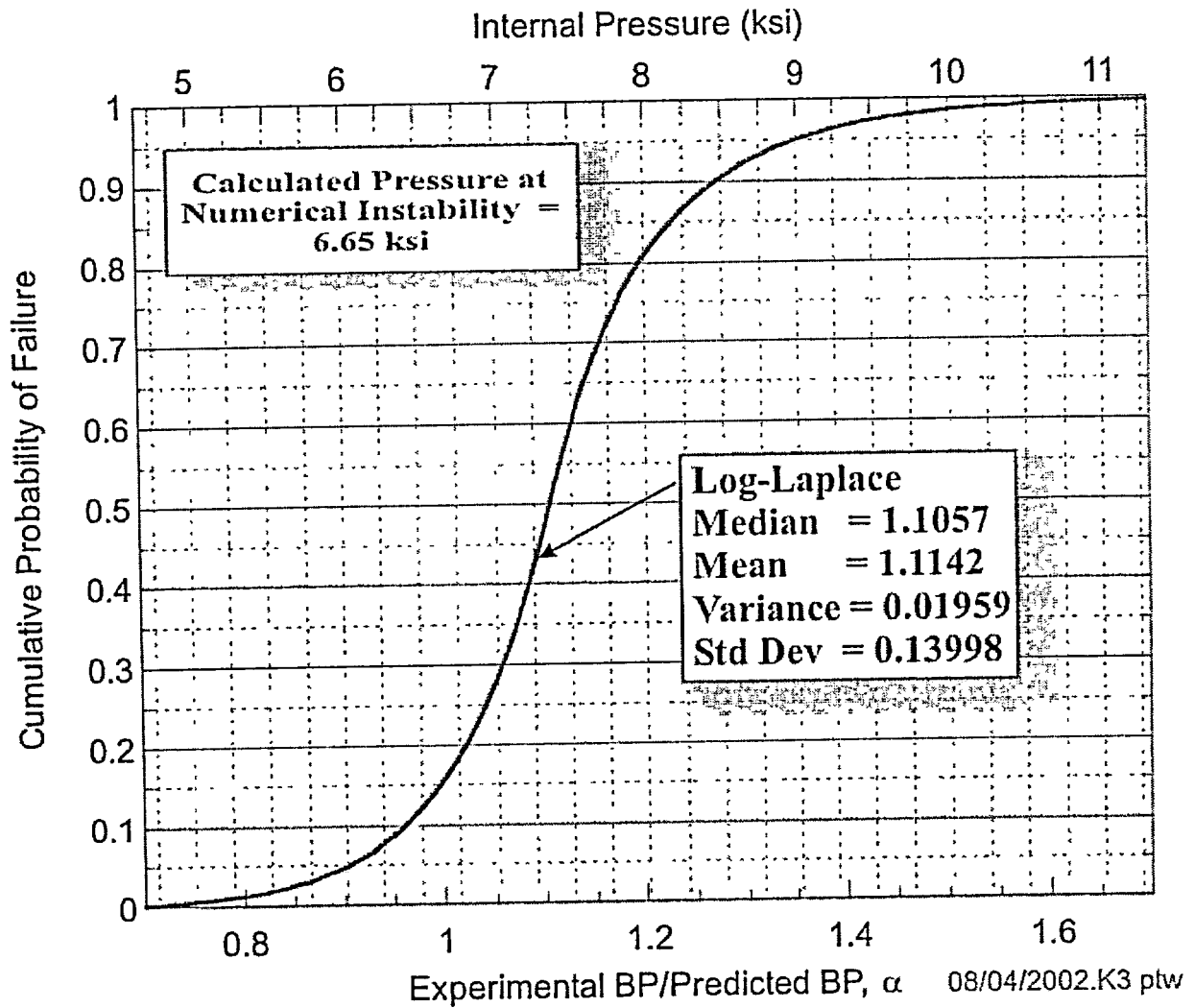


Fig. 13. Application of the failure statistical criterion produces a cumulative probability of failure (based on a Log-Laplace distribution) curve for the Bounding Case condition. Cumulative probability of failure as a function of internal pressure.

As discussed above, the “as-found” bounding calculation predicted a  $P_{NI}$  value of 6.65 ksi which has a cumulative probability of failure of 0.158 for the Log-Laplace model. Additional predicted burst pressure percentiles can be calculated including from Eq. (26):

$$\begin{aligned}
 1\% - BP_{0.01} &= 5.226 \text{ ksi} \\
 5\% - BP_{0.05} &= 6.015 \text{ ksi} \\
 50\% - BP_{0.50} &= 7.353 \text{ ksi} \\
 95\% - BP_{0.95} &= 8.990 \text{ ksi} \\
 99\% - BP_{0.99} &= 10.346 \text{ ksi}
 \end{aligned}$$

The Log-Laplace stochastic model also estimates a cumulative probability of failure of  $4.14 \times 10^{-7}$  at the operating pressure of 2.165 ksi and  $2.15 \times 10^{-6}$  at the safety-valve set-point pressure of 2.5 ksi. See Table 11 for additional estimates from all six models. For the six distributions in Tables 8 and 11, the average probability of failure is  $6.91 \times 10^{-8}$  at 2.165 ksi,  $3.60 \times 10^{-7}$  at 2.5 ksi, and 0.2155 at 6.65 ksi.

Note in Table 11, that as the internal pressure decreases from  $P_{NI}$  down to a nominal operating pressure, the variability in the failure probability estimates increases significantly. The standard deviation of the six estimates, when normalized by the sample mean, increases from 0.13 at 6.65 ksi to 2.44 at 2.165 ksi. The average values in Table 11 are dominated (at the lower tail) by the Log-Laplace distribution. For this reason, we recommend adopting the Log-Laplace model for future studies as the most appropriate distribution based on the available data. Note also that the Log-Laplace model produces the highest failure probabilities of the six candidates when extrapolating down into the lower tail of the distribution.

**Table 11. Estimated Cumulative Probability of Failures for the Bounding Calculation**

Distribution	Parameters	Point Estimator	Parameter Values	Relative Score	Failure Probability at Internal Pressure		
					2.165 ksi	2.5 ksi	6.65 ksi
Log-Laplace	Location	Default	0	98	4.14E-07	2.15E-06	0.1582
	Scale	ML estimate	1.1057				
	Shape	ML estimate	11.45441				
Beta	Lower endpoint	MOM estimate	0.61449	93	0	0	0.2340
	Upper endpoint	MOM estimate	1.78866				
	Shape #1	MOM estimate	7.95564				
	Shape #2	MOM estimate	11.38552				
Gamma	Location	Default	0	89	8.17E-19	1.50E-15	0.2236
	Scale	ML estimate	0.01444				
	Shape	ML estimate	76.01293				
Normal	Mean	ML estimate	1.09747	83.33	8.44E-10	8.90E-09	0.2234
	Standard Dev	ML estimate	0.12811				
Random Walk	Location	Default	0	75	0	0	0.2269
	Scale	ML estimate	0.92335				
	Shape	ML estimate	69.18788				
Inverse Gaussian	Location	Default	0	71	4.01E-29	1.79E-22	0.2269
	Scale	ML estimate	1.09747				
	Shape	ML estimate	82.23451				
Average=					6.91E-08	3.60E-07	0.2155
StdDev=					1.69E-07	8.77E-07	0.0283
StdDev/Average=					2.44	2.44	0.13

## 5. Summary and Conclusions

Six stochastic models of the probability of failure associated with a computational prediction of the plastic collapse of the exposed cladding in the wastage area of the Davis-Besse RPV head have been developed from the following technical bases:

- (1) *experimental data* obtained during disk-burst tests reported by Riccardella [2] with loadings, geometries, and materials relevant to the Davis-Besse pressure loading, wastage-area footprint, and cladding,
- (2) nonlinear, large-deformation, elastic-plastic *discrete-element analyses* of the disk-burst tests also reported in [2] (GAPL-3 discrete-element code[3]),
- (3) nonlinear, finite-strain, elastic-plastic *finite-element analyses* performed for the current study (ABAQUS finite-element code[4]) of the nine disk-burst test specimens reported in [2], and
- (4) a *theoretical criterion* for plastic instability in a circular diaphragm under pressure loading, due to Hill [5] (as cited in [7]), applied to the disk-burst tests.

Among the twenty-six continuous distributions investigated, six passed all of the heuristic and *Goodness of Fit* tests applied in the analysis. The six distributions ranked in relative order are: (1) Log-Laplace, (2) Beta, (3) Gamma, (4) Normal, (5) Random Walk, and (6) Inverse Gaussian. As an example of how the stochastic models may be applied to the Davis-Besse wastage area problem, the top-ranked Log-Laplace model has the scaled form of

$$\Pr[P_{BP(true)} \leq SP] = F_{LP}(SP | P_{NI}) = \begin{cases} \frac{1}{2} \left( \frac{SP}{1.1057 \times P_{NI}} \right)^{11.45441} & ; 0 < SP < 1.1057 \times P_{NI} \\ 1 - \frac{1}{2} \left( \frac{SP}{1.1057 \times P_{NI}} \right)^{-11.45441} & ; SP \geq 1.1057 \times P_{NI} \end{cases} \quad (27)$$

Given a computationally-determined *pressure at numerical instability*,  $P_{NI}$ , and service pressure,  $SP$ , the model gives an estimate of the cumulative probability of nonexceedance of the true but unknown burst pressure,  $P_{BP(true)}$ , i.e.,  $\Pr[P_{BP(true)} \leq SP]$ .

Due to the small sample size ( $n = 26$ ) used in the stochastic model development, no definitive claim can be made that one distribution is significantly superior to the other five; however, the Log-Laplace is shown to have the highest ranking given the available data, and it produces the highest failure probabilities when extrapolating to service pressures well below the range of the data, e.g., to the nominal

operating pressure or safety-valve set-point pressure. The Log-Laplace stochastic model is, therefore, the recommended candidate for future applications to the Davis-Besse wastage-area problem.

As an example application, estimates are provided for a bounding calculation of the “as-found” Davis-Besse wastage area. The bounding calculation predicted a  $P_M$  value of 6.65 ksi. From the Log-Laplace stochastic model, the corresponding median failure pressure is 7.35 ksi. Taking the average of the estimates from all six distributions produces a probability of failure of  $6.91 \times 10^{-8}$  at 2.165 ksi,  $3.60 \times 10^{-7}$  at 2.5 ksi, and 0.2155 at 6.65 ksi.

These results for the “as-found” Davis-Besse wastage area can be considered *bounding* due to the following factors:

- (a) The modeled wastage-area footprint is slightly larger than the exposed-cladding area reported in [12].
- (b) The minimum cladding thickness of 0.24 inches reported in [12] was used in this analysis.
- (c) A lower-bound stress-strain curve was constructed from the available tensile data for the cladding material.
- (d) The reinforcing effect of the *J*-groove weld was not included in the simulation.

## References

1. *Recent Experience with Degradation of Reactor Pressure Vessel Head*, NRC Information Notice 2002-11, United States Nuclear Regulatory Commission, Office of Nuclear Reactor Regulation, Washington, DC, March 12, 2002.
2. P. C. Riccardella, “Elasto-Plastic Analysis of Constrained Disk Burst Tests,” Paper No. 72-PVP-12, presented at the ASME *Pressure Vessels and Piping Conference*, September 17-21, 1972, New Orleans, LA.
3. A. L. Thurman, *GAPL-3-A Computer Program for the Inelastic Large Deflection Stress Analysis of a Thin Plate or Axially Symmetric Shell with Pressure Loading and Deflection Restraints*, WAPD-TM-791, Bettis Atomic Power Laboratory, Pittsburgh, PA, June 1969.
4. *ABAQUS/Standard User's Manual, v. 6.2*, Hibbit, Karlsson, and Sorensen, Inc., Pawtucket, RI, 2001.
5. R. Hill, “A Theory of the Plastic Bulging of a Metal Diaphragm by Lateral Pressure,” *Philos. Mag. (Ser. 7)* 41, (1950) 1133.
6. J. Chakrabarty and J. M. Alexander, “Hydrostatic Bulging of Circular Diaphragms,” *J. Strain Anal.* 5(3), (1970) 155-161.
7. A. R. Ragab and S. E. Bayoumi, *Engineering Solid Mechanics, Fundamentals and Applications*, CRC Press LLC, Boca Raton, FL, 1999.

8. W. E. Cooper, E. H. Kotteamp, and G. A. Spiering, "Experimental Effort on Bursting of Constrained Disks as Related to the Effective Utilization of Yield Strength," Paper No. 71-PVP-49, ASME *Pressure Vessels and Piping Conference*, May 1971.
9. A. M. Law, *Expert Fit<sup>®</sup> User's Guide*, Averill M. Law & Associates, Tuscon, Arizona, May 2002.
10. Personal communication with Computational Mechanics Corporation of Columbus, Columbus, OH, March 2002, Data from PIFRAC database.
11. *Nuclear Systems Materials Handbook*, Vol. 1, Design Data, Section 1A for 308/308L weld, Table II.
12. S. A. Loehlein, *Root Cause Analysis Report, Significant Degradation of Reactor Pressure Vessel Head*, CR 2002-0891, Davis-Besse Power Station, April 15, 2002.

Contract Program or  
Project Title:

Heavy-Section Steel Technology (HSST) Program

Subject of this Document:

Analysis of the Davis-Besse RPV Head Wastage Area and Cavity

Type of Document:

Letter Report

Authors:

P. T. Williams  
B. R. Bass

Date of Document:

September 2002

Responsible NRC Individual  
and NRC Office or Division

M. T. Kirk  
Division of Engineering Technology  
Office of Nuclear Regulatory Research

Prepared for the  
U. S. Nuclear Regulatory Commission  
Washington, D.C. 20555-0001  
Under Interagency Agreement DOE 1886-N653-3Y  
NRC JCN NoY6533

OAK RIDGE NATIONAL LABORATORY  
Oak Ridge, Tennessee 37831-8056  
managed and operated by  
UT-Battelle, LLC for the  
U. S. DEPARTMENT OF ENERGY  
under Contract No. DE-AC05-00OR22725

# **Analysis of the Davis-Besse RPV Head Wastage Area and Cavity**

P. T. Williams  
B. R. Bass

Oak Ridge National Laboratory  
Oak Ridge, Tennessee

Manuscript Completed – September 2002  
Date Published –

Prepared for the  
U.S. Nuclear Regulatory Commission  
Office of Nuclear Regulatory Research  
Under Interagency Agreement DOE 1886-N653-3Y

NRC JCN No. Y6533

OAK RIDGE NATIONAL LABORATORY  
Oak Ridge, Tennessee 37831-8063  
managed and operated by  
UT-Battelle, LLC for the  
U. S. DEPARTMENT OF ENERGY  
under Contract No. DE-AC05-00OR22725

**CAUTION**

This document has not been given final patent clearance and is for internal use only. If this document is to be given public release, it must be cleared through the site Technical Information Office, which will see that the proper patent and technical information reviews are completed in accordance with the policies of Oak Ridge National Laboratory and UT-Battelle, LLC.

This report was prepared as an account of work sponsored by an agency of the United States government. Neither the United States government nor any agency thereof, nor any of their employees, makes any warranty, express or implied, or assumes any legal liability or responsibility for the accuracy, completeness, or usefulness of any information, apparatus, product, or process disclosed, or represents that its use would not infringe privately owned rights. Reference herein to any specific commercial product, process, or service by trade name, trademark, manufacturer, or otherwise, does not necessarily constitute or imply its endorsement, recommendation, or favoring by the United States government or any agency thereof. The views and opinions of authors expressed herein do not necessarily state or reflect those of the United States government or any agency thereof.

# Analysis of the Davis-Besse RPV Head Wastage Area and Cavity

P. T. Williams and B. R. Bass  
Oak Ridge National Laboratory  
P. O. Box 2009  
Oak Ridge, TN, 37831-8056

## Abstract

In support of ongoing investigations by the United States Nuclear Regulatory Commission's (NRC) Office of Nuclear Regulatory Research, the Heavy-Section Steel Technology Program at Oak Ridge National Laboratory has carried out structural analyses of the damaged reactor pressure vessel (RPV) head located at the Davis-Besse Nuclear Power Station. This report presents the results of a finite-element analysis of the wastage area using submodeling techniques. A bounding case for the "as-found" condition of the cavity is developed and analyzed under static pressure loading conditions up to the point of failure. The specific failure mode addressed by this analysis is *incipient tensile plastic instability* (i.e., plastic collapse) of the cladding. Wastage-area growth scenarios are also postulated based on assumed *self-similar* and *ellipsoidal* growth patterns, and the amount of exposed cladding surface area required to produce failure down to the nominal reactor coolant system (RCS) operating pressure is estimated for each growth pattern. Comparisons are made between the finite-element computational results and the burst pressure predictions from a theoretical model (*center-membrane theory* of Chakrabarty and Alexander (1970)) of failure in circular diaphragms under lateral pressure loading. A stochastic model, presented in an earlier report [1], is also applied to provide probabilistic estimates of the predictive uncertainty of the computational results.

For the bounded "as-found" case, the median predicted burst pressure,  $BP_{0.5}$ , is 7.36 ksi for a cladding thickness of 0.24 in. and 5.73 ksi for a cladding thickness of 0.1825 in. For  $BP_{0.5}$  equal to the nominal operating pressure of 2.165 ksi, the *center-membrane theory* estimates a required diaphragm area of 498.9 in<sup>2</sup> with a cladding thickness of 0.24 in. The value of 0.24 in. is the minimum cladding thickness obtained from UT measurements of the wastage area based on a 1/2 inch grid.

Estimates of failure pressure with associated probabilities can be calculated for a broad range of exposed cladding areas from the theoretical treatment of circular diaphragms due to Chakrabarty and Alexander (1970) in conjunction with the stochastic model described in a previous report [1]. The thin-walled membrane assumptions applied in the theory appear to better approximate the conditions in the exposed cladding as the wastage area increases in size. It is also observed that the shape of the footprint approaches a second-order effect as the footprint area increases.

# 1 Introduction

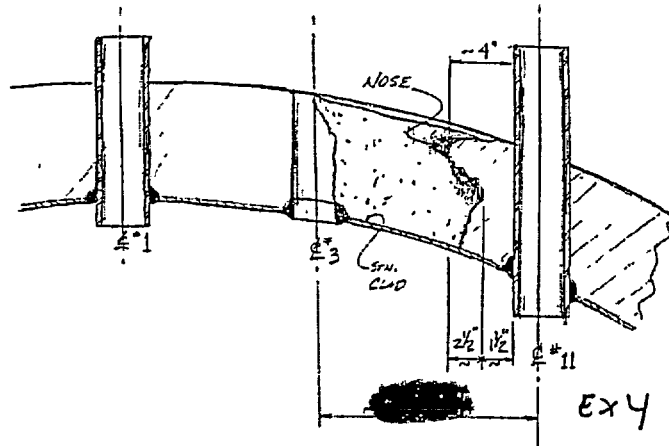
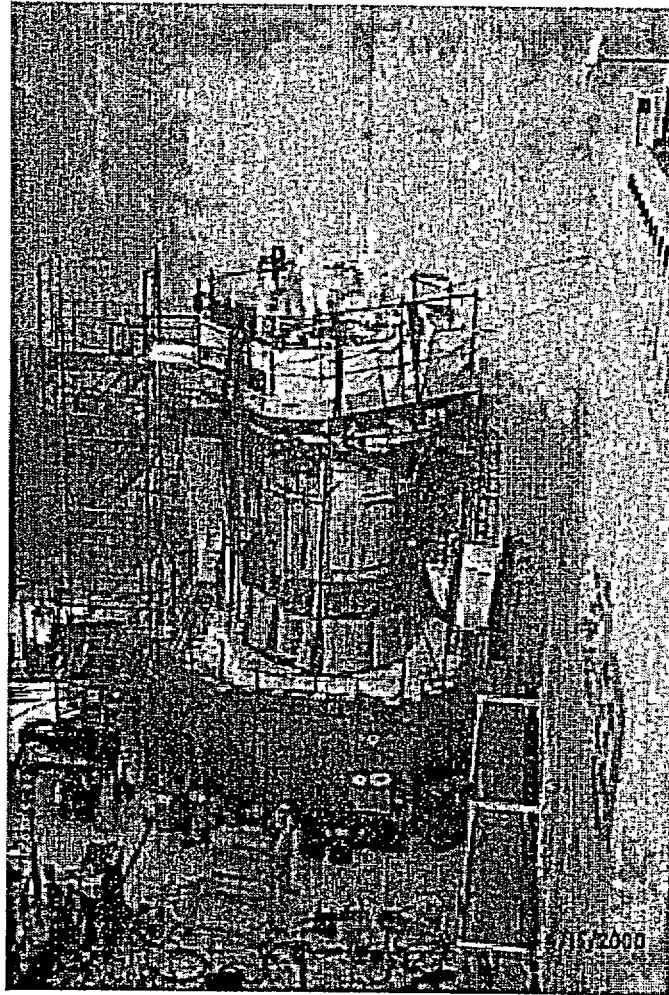
## 1.1 Objective

In support of ongoing investigations by the United States Nuclear Regulatory Commission's (NRC) Office of Nuclear Regulatory Research, the Heavy-Section Steel Technology Program at Oak Ridge National Laboratory has carried out structural analyses of the damaged reactor pressure vessel (RPV) head located at the Davis-Besse Nuclear Power Station. This report presents the results of a finite-element analysis of the wastage area using submodeling techniques. A stochastic model, presented in an earlier report [1], is also applied to provide probabilistic estimates of the predictive uncertainty of the computational results.

## 1.2 Background

Pursuant to the licensee's commitments to NRC Bulletin 2001-01 [2], the Davis-Besse Nuclear Power Station began a refueling outage [3] on February 16, 2002, that included inspection of the vessel head penetrations with an emphasis on the inspection of control rod drive mechanism (CRDM) nozzles. These inspections identified axial indications in three CRDM nozzles (Nozzles 1, 2, and 3, located near the center of the RPV head) that were experiencing pressure-boundary leakage. Upon completing boric acid removal on March 7, 2002, the licensee conducted a visual examination of the area and identified a large cavity in the RPV head on the downhill side of CRDM Nozzle 3. Followup characterization by ultrasonic testing (UT) indicated wastage of the low alloy steel RPV head material adjacent to the nozzle. The wastage area was found to extend approximately 5 inches downhill on the RPV head from the penetration for CRDM Nozzle 3, with a width of approximately 4 to 5 inches at its widest part.

See Fig. 1. for a photograph of the Davis-Besse RPV, a schematic of a typical nuclear power reactor showing the location of the CRDM nozzles relative to the RPV, and a sketch and photographs of the cavity and wastage area around Nozzle 3.



The above figure shows the Davis Besse reactor vessel head degradation between nozzle #3 and nozzle #11. This sketch was provided to the NRC by the Licensee.

Fig. 1. (a) Davis-Besse Nuclear Power Station RPV and (b) sketch of RPV head degradation.

## Typical Pressurized Water Reactor

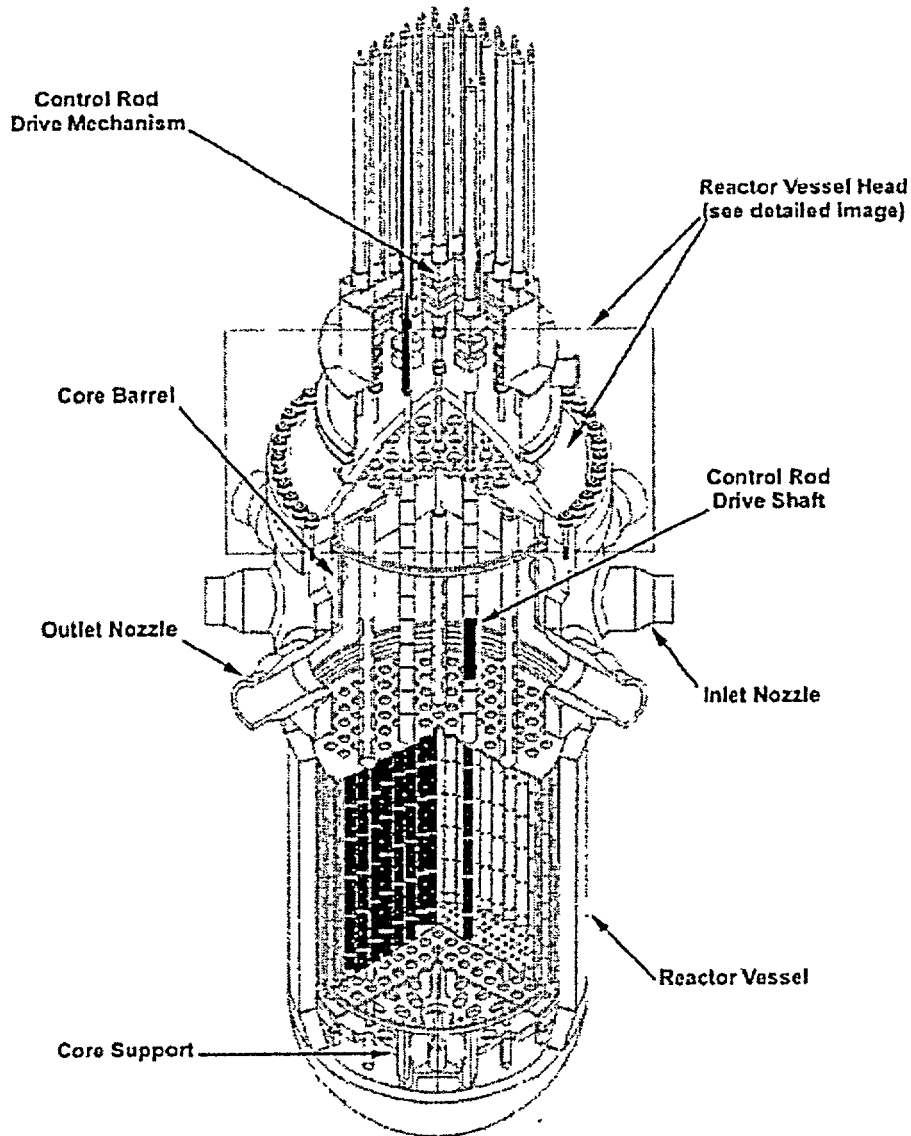


Fig. 1 (continued) (c) schematic of a typical nuclear power reactor showing the relationship of the CRDM nozzles to the RPV head.

### Reactor Vessel Head Degradation Location

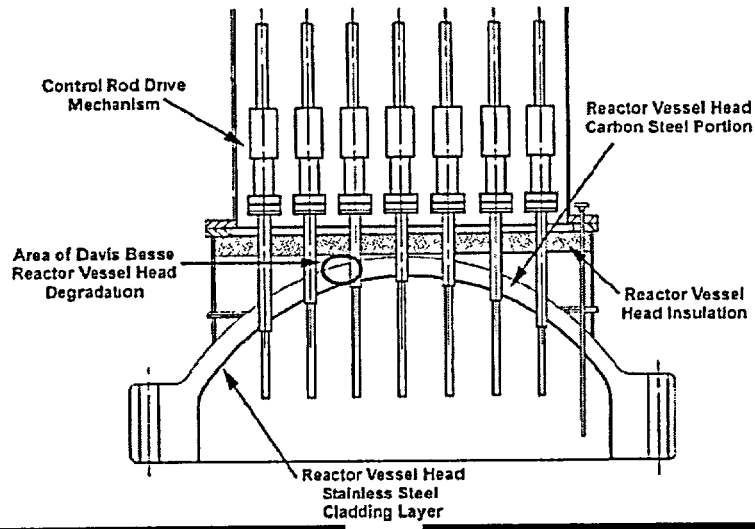


Fig. 1. (continued) (d) photographs of the wastage area and cavity with Nozzle 3 removed.

### **1.3 Scope**

Section 2 reviews the geometry and material properties used in the development of the finite-element global and submodels; Section 3 presents the algorithms used to estimate the growth patterns of the wastage-area footprint; Section 4 presents the results of both the bounding calculations for the “as found” condition of the wastage area and the growth-pattern results compared to the predictions of a theoretical treatment of failure in circular diaphragms; and Section 5 provides a summary and conclusions.

## 2 Geometry and Material Properties

### 2.1 “As-Found” Footprint Geometry

Tables 1 and 2 present the details of the “as-found” geometry of the wastage area. The figure in Table 2 was taken from Fig. 13 of the *Root Cause Analysis Report, Significant Degradation of Reactor Pressure Vessel Head*, CR 2002-0891 [4]. The “as-found” footprint in Table 2 was digitized with CorelDraw 10<sup>®</sup>. Additional details for the “as-found” case are given in [1].

### 2.2 Material Properties

Three materials are used in the construction of the finite-element submodel of the wastage area: (1) Alloy 600 for the CRDM tubes, (2) A533B for the base material of the vessel, and (3) SS308 for the subarc weld (SAW) cladding. Elastic properties [5] for these three materials are shown in Fig. 2 as a function of temperature. Figure 3 presents plastic properties [5] (effective stress as a function of effective plastic strain) for Alloy 600 and A533B pressure vessel steel. An adjusted SS308 stress vs. strain curve used in the bounding-case calculations is compared in Fig. 4 to curves from a range of A8W heats (SS304 pipe with SS308 weld from the PIFRAC database [5]) and the unadjusted stress vs. strain curve received from Framatome [6]. Strain hardening for the adjusted curve was reduced to lower-bound all of the data, where the offset yield strength and strain at ultimate strength were retained from the unadjusted SS308 curve. This adjusted stress/strain curve was applied in the “bounding” calculation for the “as-found” condition and all subsequent cavity growth cases.

### 2.3 Finite-Element Global and Submodels of Wastage Area and Cavity

The submodeling capabilities of the ABAQUS finite-element code [7] were employed in this analysis to focus the available computational resources on the region of interest located around the wastage area cavity at CRDM Nozzle 3. Submodeling can be used to investigate a portion of a model with a refined mesh. The boundary conditions of the *submodel* are driven by an interpolation of the displacement solution from an initial, relatively coarse, *global model*. The technique is primarily useful when it is necessary to obtain a refined, detailed solution in a local region, and the detailed modeling of that local region has a negligible effect on the global solution, i.e., solution information is passed in one direction only, from the global model to the submodel.

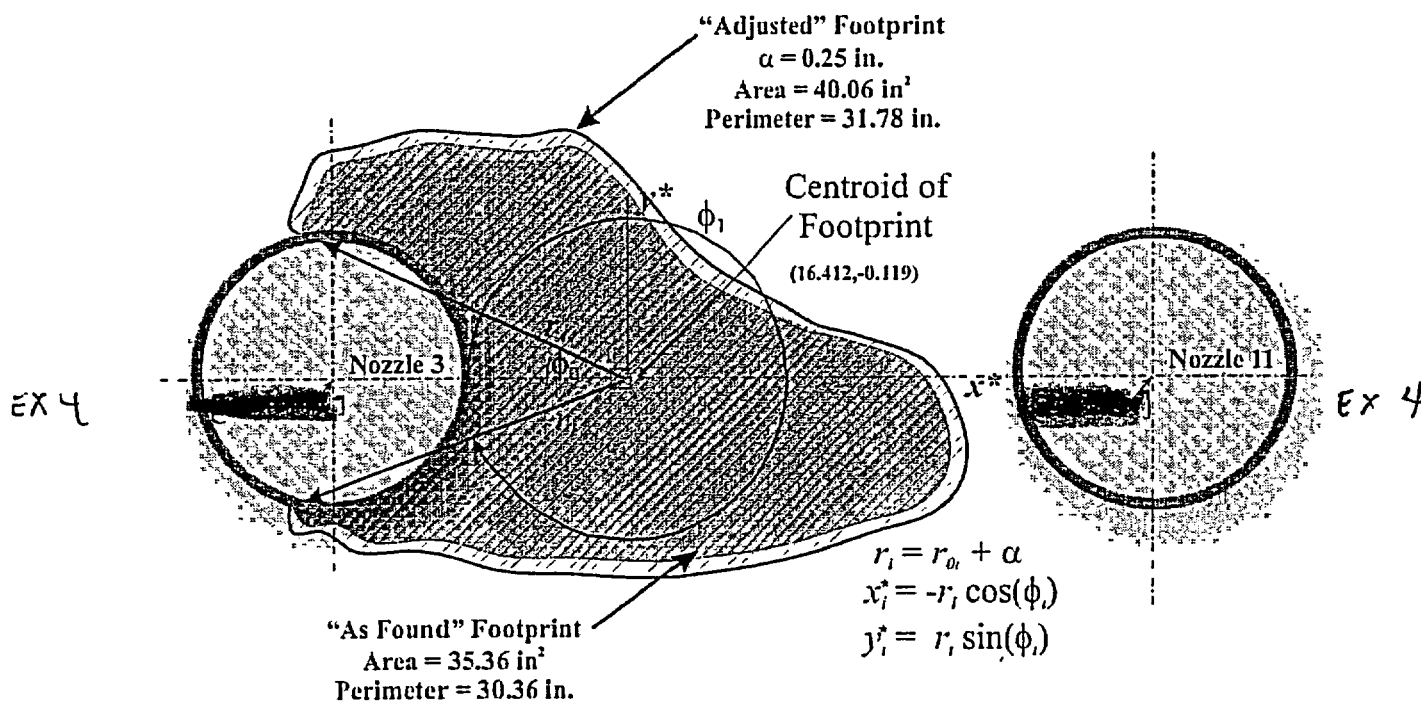
As shown in Figs. 5a and 6, the global model consists of the full RPV head (with all 69 penetrations) and closure flange. No cladding or CRDM nozzles are included in the global model. The submodel (see Fig. 5b) consists of the cladding (SS308), base (A533B), and CRDM Nozzles (A600) 3, 11, 15, and 16. The plan views of the RPV head in Fig. 7a and 7b indicate the position and geometry of the submodel

with respect to the global model. Figure 8 shows the ProEngineer® solid model of the submodel. This solid model was imported into MSC Patran® where the finite-element mesh was constructed.

**Table 1. Wastage-Area-Footprint Geometry Data**

Description	Scaling Factor	Area (in <sup>2</sup> )	Perimeter (in.)	Centroid of Wastage Area Footprint		Moments of Inertia About the Centroid			Eigenvalue Extraction for Principal Moments and Directions			
				$x_c$ (in.)	$y_c$ (in.)	$I_x$ (in <sup>4</sup> )	$I_y$ (in <sup>4</sup> )	$I_{xy}$ (in <sup>4</sup> )	Principal Moments		Principal Directions	
									$I_1$ (in <sup>4</sup> )	$I_2$ (in <sup>4</sup> )	$\langle n_x, n_y \rangle$	$\langle n_x, n_y \rangle$
As-Found Footprint	1	35.36	30.36	16.4122	-0.1194	98.89	9699.33	-117.16	75.26	197.41	$\langle 0.9004, -0.4351 \rangle$	$\langle 0.4351, 0.9004 \rangle$
Adjusted Footprint for Bounding Calculation	0.25 in	40.06	31.78	16.4301	-0.1255	129.02	11031.81	-141.35	99.00	245.71	$\langle 0.8943, -0.4476 \rangle$	$\langle 0.4476, 0.8943 \rangle$

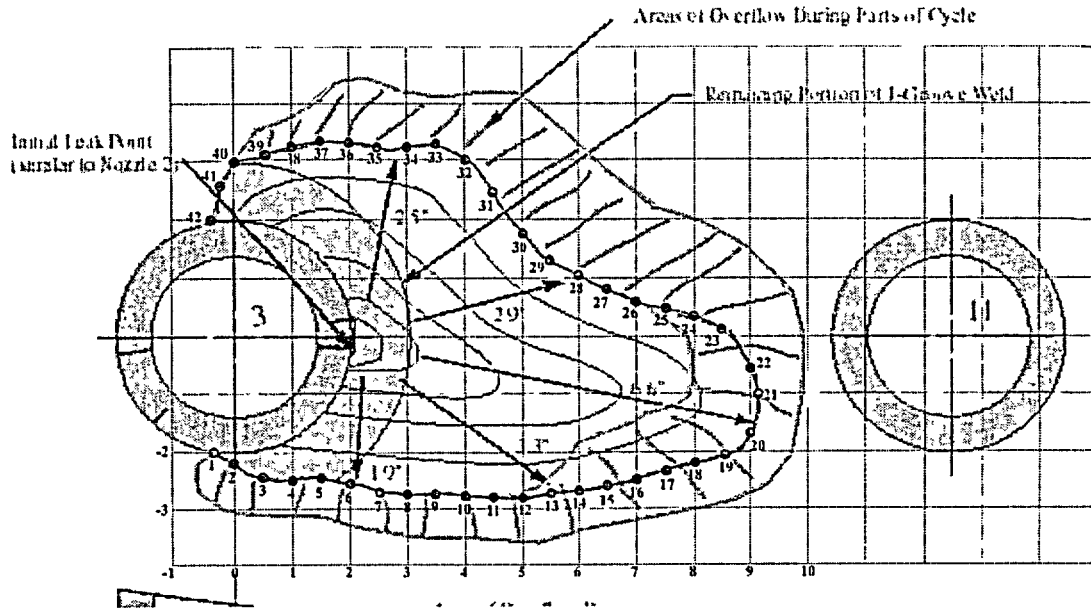
Footprint centroid is in global coordinates  
 Global coordinate system has its z-axis aligned with the vertical centerline of the vessel  
 The x-y plane of the global coordinate system is a horizontal plane  
 with the x-axis along the line between the centerlines of Nozzles 3 and 11



## 2.4 Loading and Constraint Conditions

Only mechanical loading due to the internal pressure of the coolant was considered in these analyses. The pressure load was applied to the inner surface of the vessel and the inside of the CRDM nozzles. Tied contact constraints were established between the cladding and base material interface and between the CRDM nozzles and the cladding and base. The J-groove weld attaching the nozzle to the vessel was not explicitly modeled. The vertical surfaces of the submodel were driven by the interpolated displacement solution obtained with the global model of the RPV head (see Fig. 5).

Table 2. Details of Wastage Area Footprint Before Adjustment for Bounding Calculation  
(Figure taken from Fig. 13 ref. [4])



Point	$x^*$	$y^*$	Point	$x^*$	$y^*$
0	-0.639	-1.895	24	8.000	0.334
1	-0.334	-2.280	25	7.500	0.483
2	0.000	-2.235	26	7.000	0.582
3	0.500	-2.492	27	6.500	0.829
4	1.000	-2.522	28	6.000	1.046
5	1.500	-2.482	29	5.500	1.303
6	2.000	-2.581	30	5.000	1.778
7	2.500	-2.730	31	4.500	2.460
8	3.000	-2.769	32	4.000	3.023
9	3.500	-2.759	33	3.500	3.300
10	4.000	-2.789	34	3.000	3.221
11	4.500	-2.819	35	2.500	3.250
12	5.000	-2.819	36	2.000	3.300
13	5.500	-2.759	37	1.500	3.349
14	6.000	-2.700	38	1.000	3.240
15	6.500	-2.621	39	0.500	3.122
16	7.000	-2.512	40	0.000	3.000
17	7.500	-2.364	41	-0.210	2.578
18	8.000	-2.216	42	-0.364	2.000
19	8.500	-2.087	43	-0.242	1.985
20	9.000	-1.712			
21	9.135	-1.000			
22	9.000	-0.555			
23	8.500	0.137			

Origin of local coordinate system located at centerline of Nozzle 3. (inches)

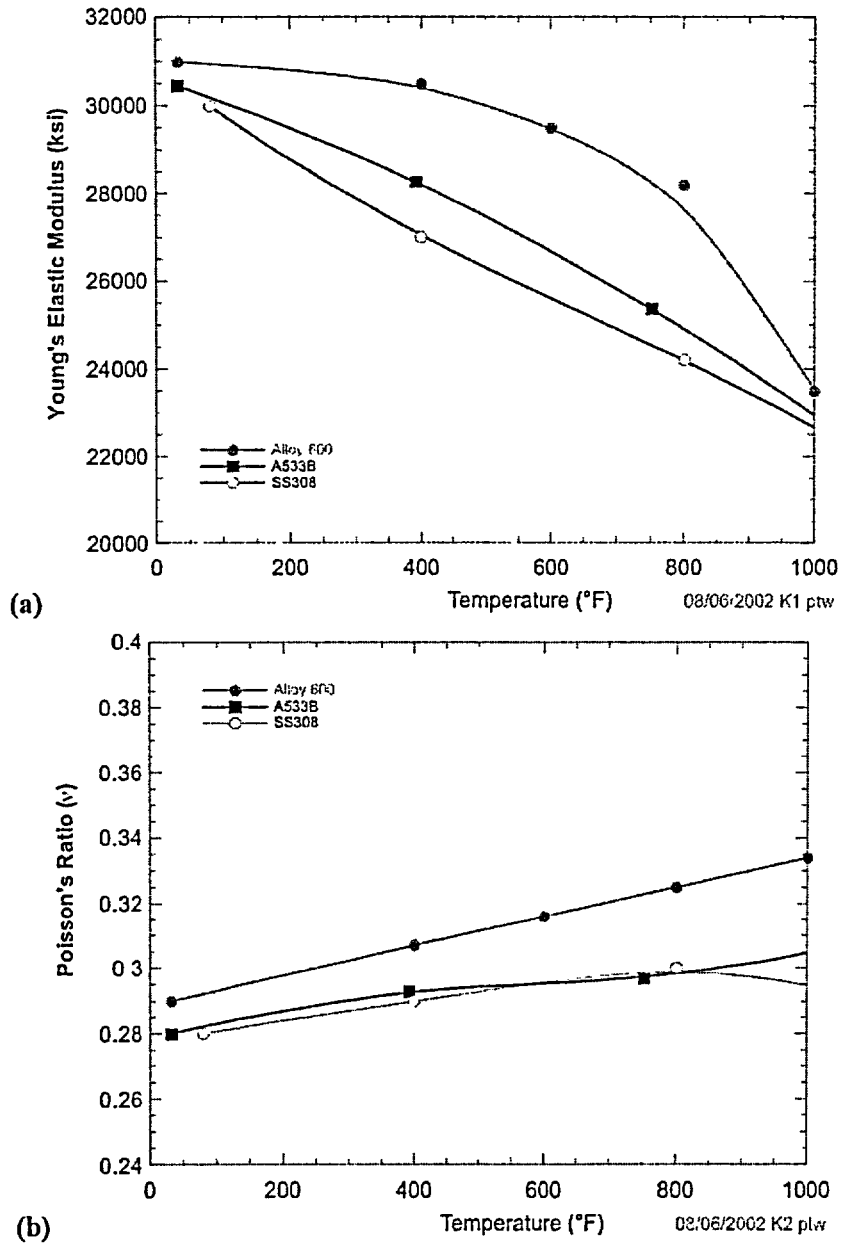


Fig. 2. Elastic properties [5] of the materials used in the finite-element models of the wastage area: (a) Young's elastic modulus and (b) Poisson's ratio.

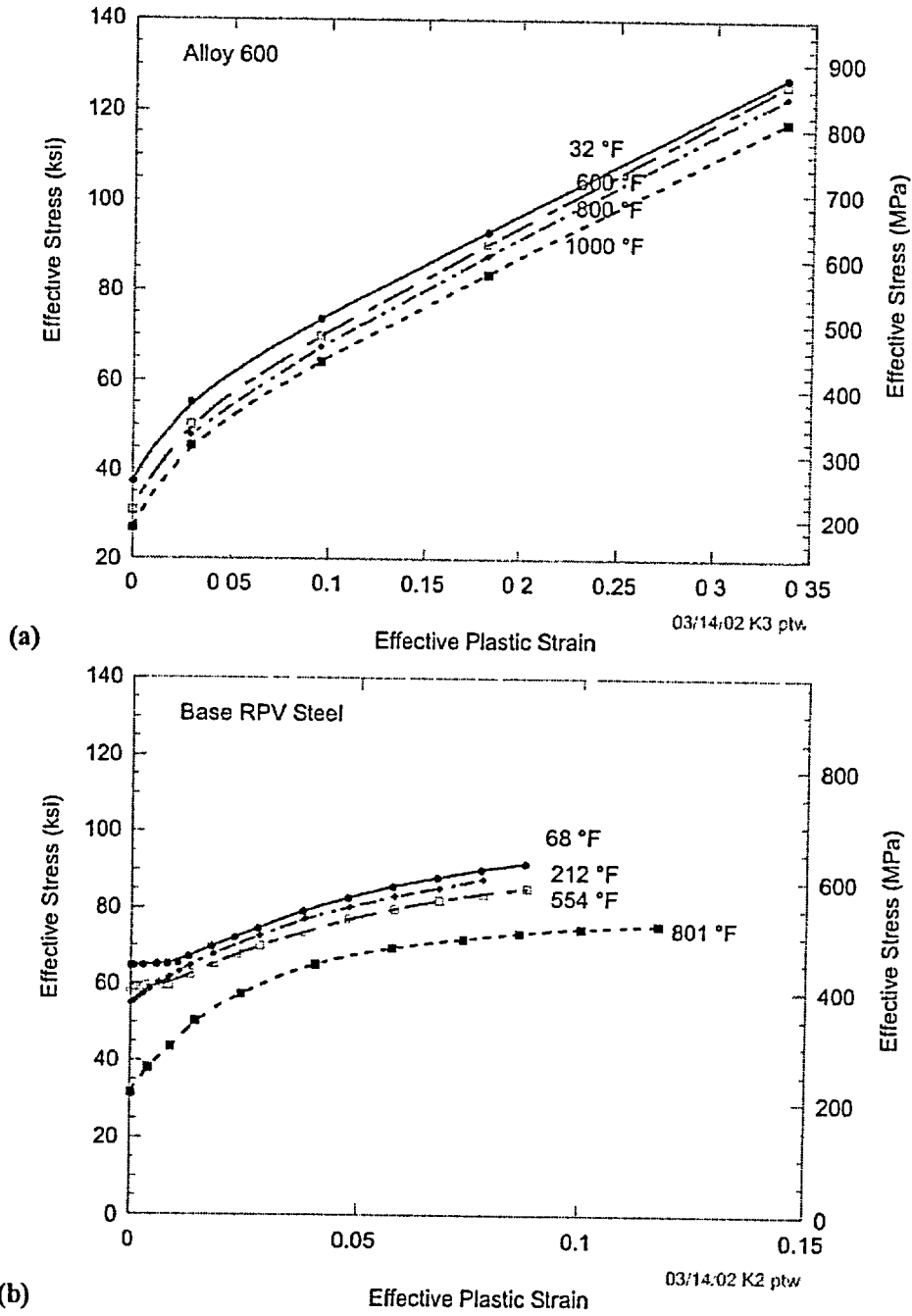


Fig. 3. Plastic property data [5] used in global and submodel: (a) Alloy 600 and (b) A533B pressure vessel steel.

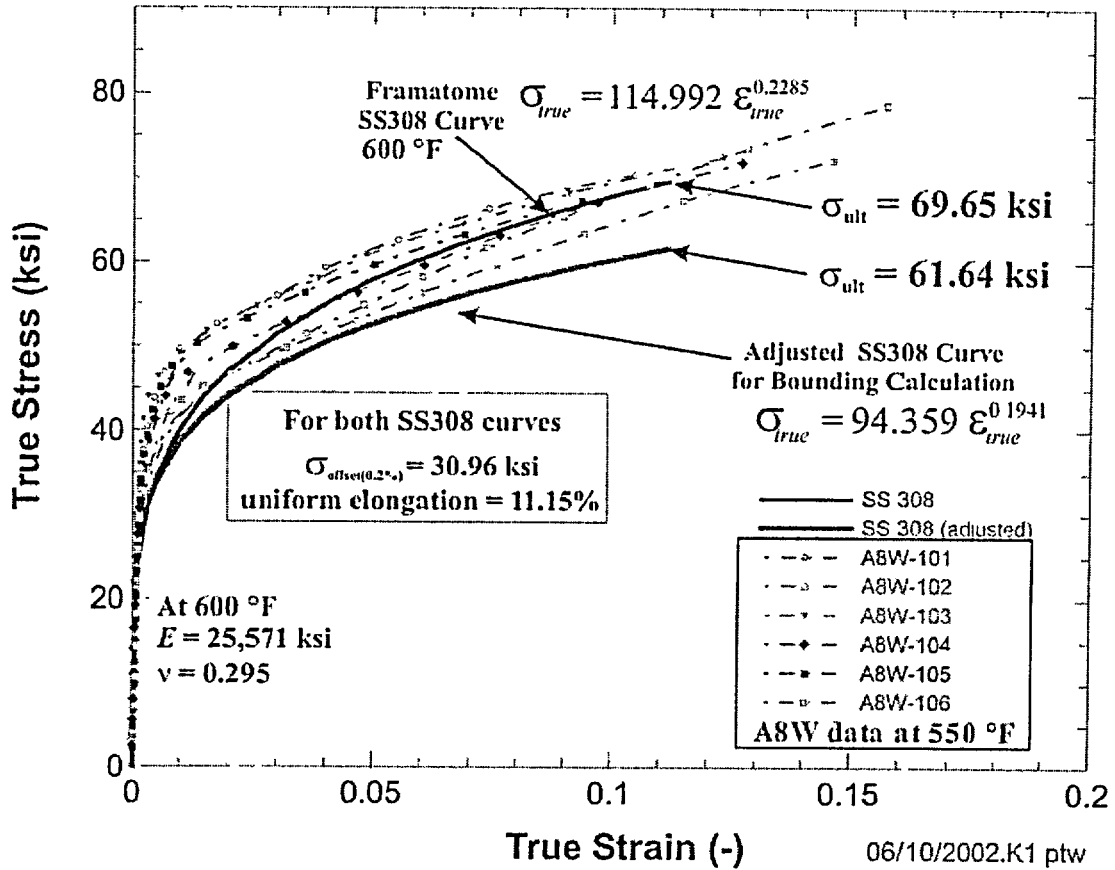


Fig. 4. Adjusted SS308 stress vs. strain curve used in the bounding-case calculations compared to curves from a range of A8W heats [5]. Strain hardening in the adjusted curve was reduced to lower-bound all of the data. The offset yield strength and strain at ultimate strength were retained from the unadjusted SS308 curve received from Framatome [6].

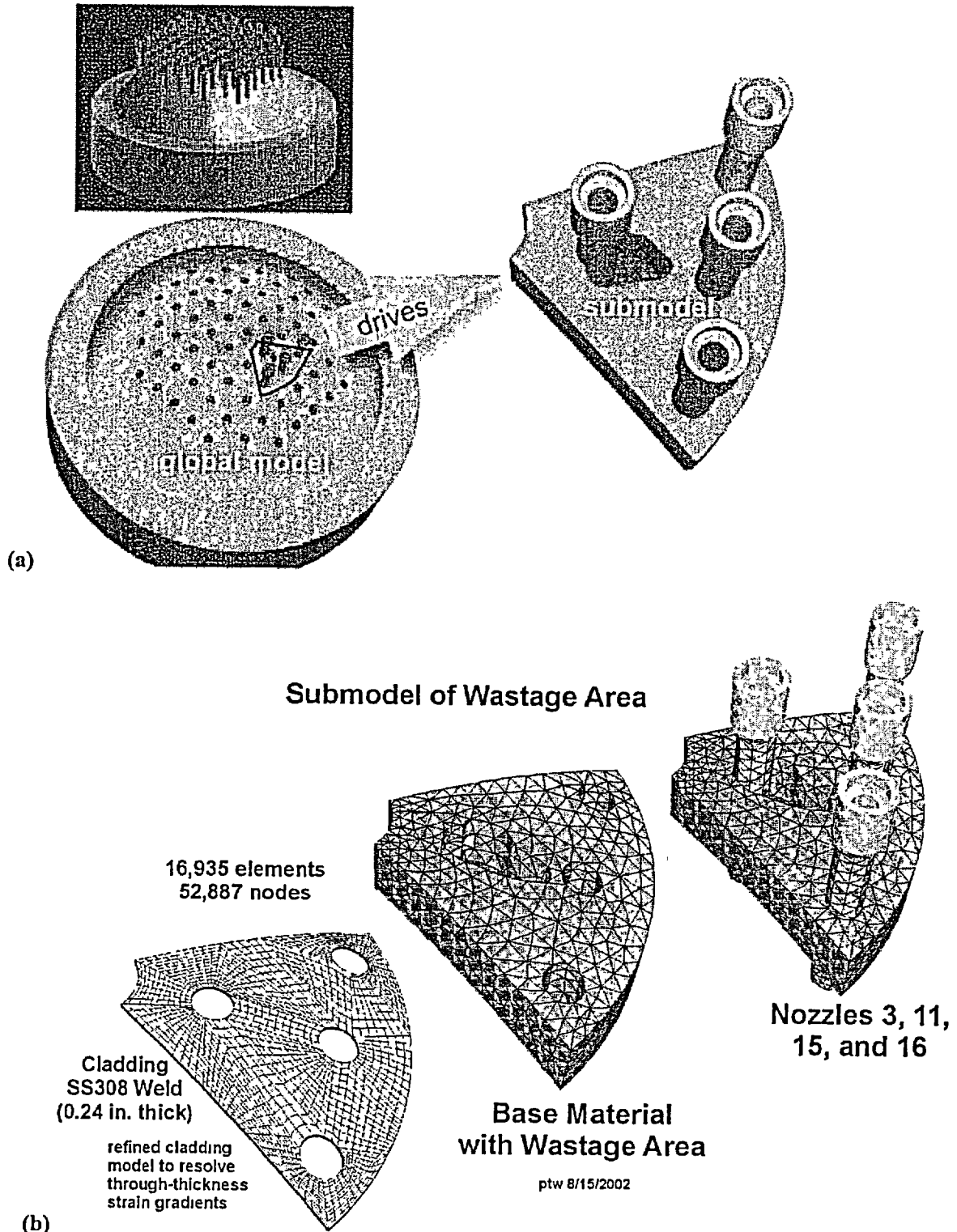
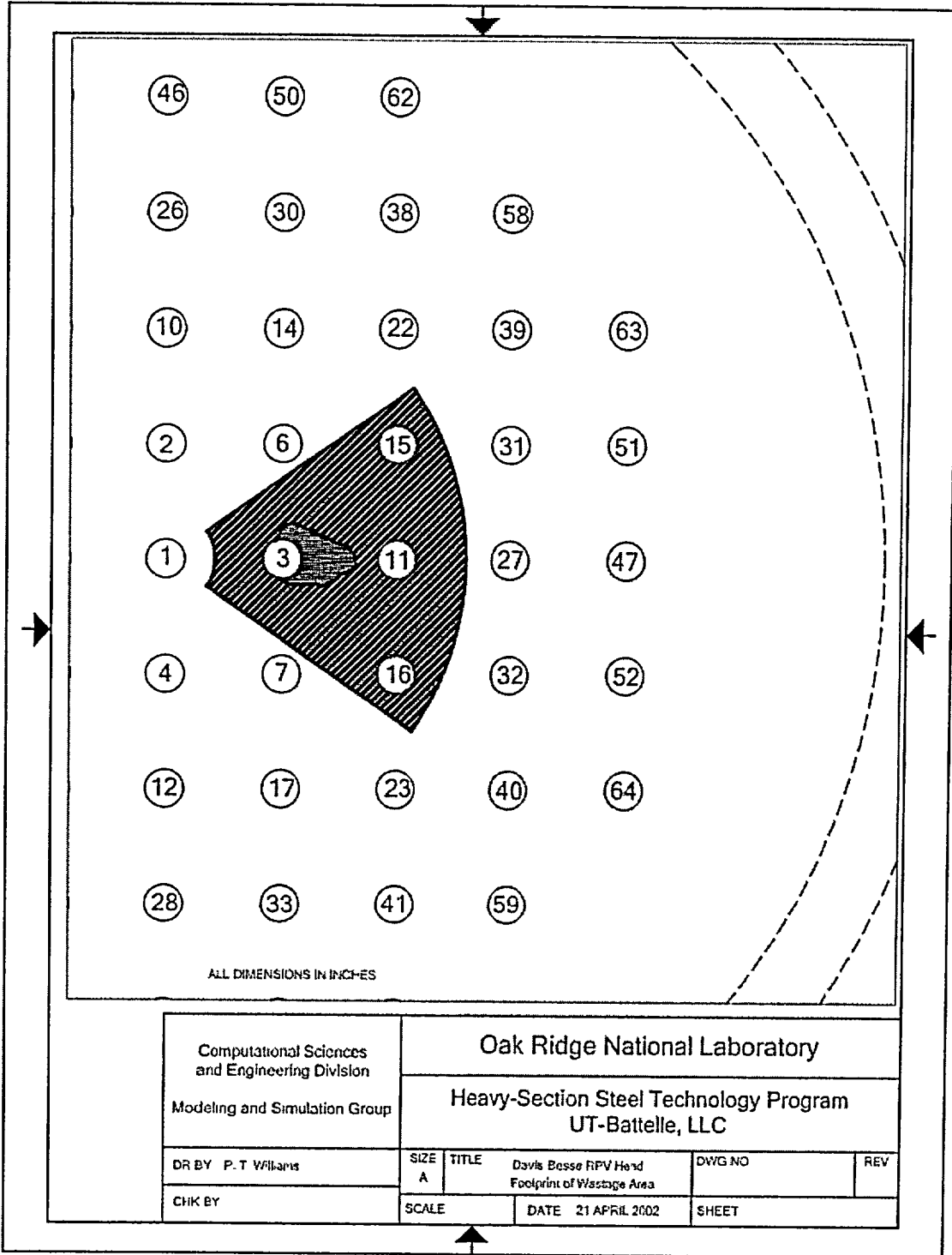


Fig. 5. Finite-element global and submodels of the Davis-Besse head and wastage area. The displacements at the vertical side boundaries of the submodel are driven by the global model. Both models are exposed to the same internal pressure loading.





(a)

Fig 7. (a) Relative location of submodel within full RPV head,

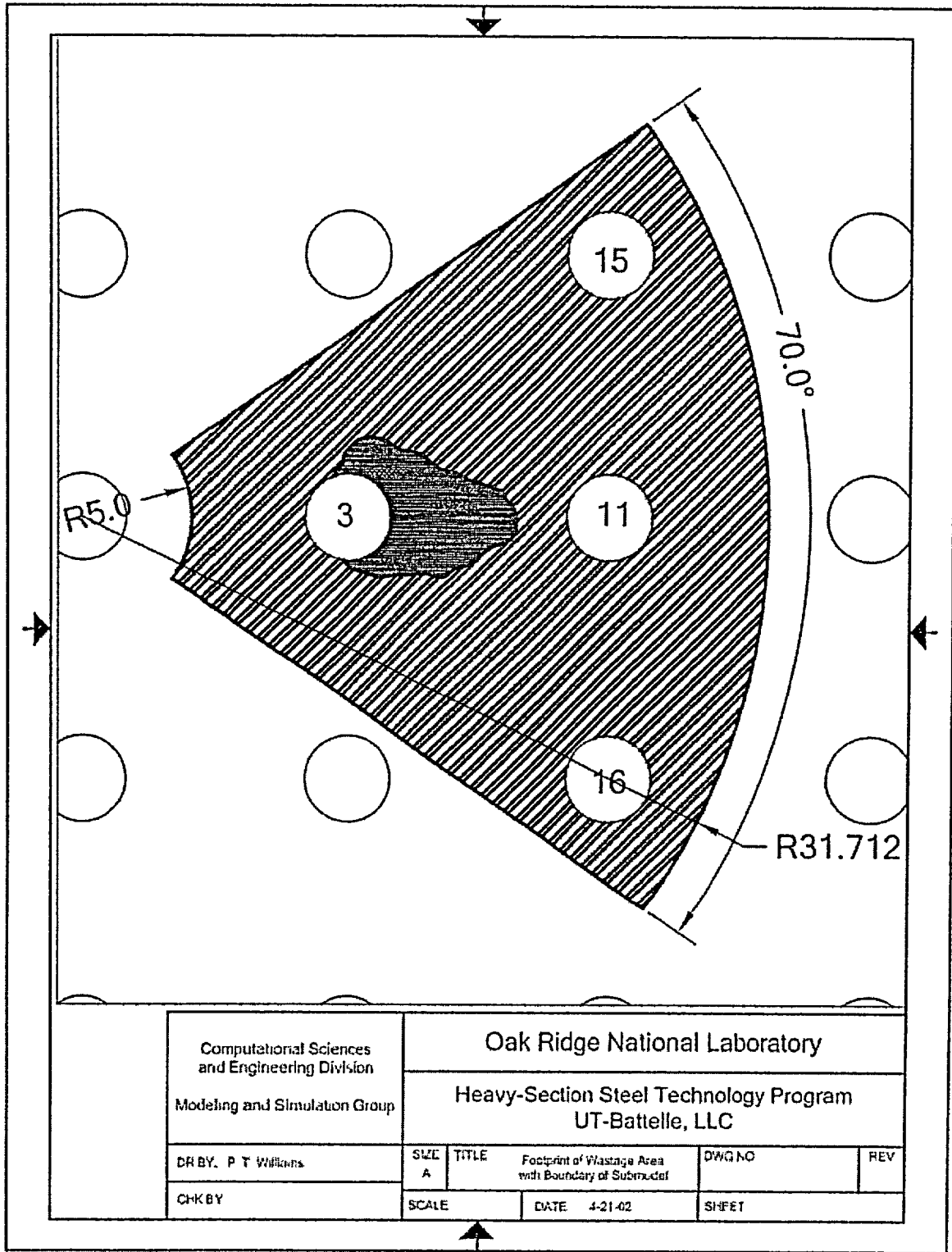


Fig. 7. (continued) (b) geometry of submodel relative to Nozzles 3, 11, 15, and 16.

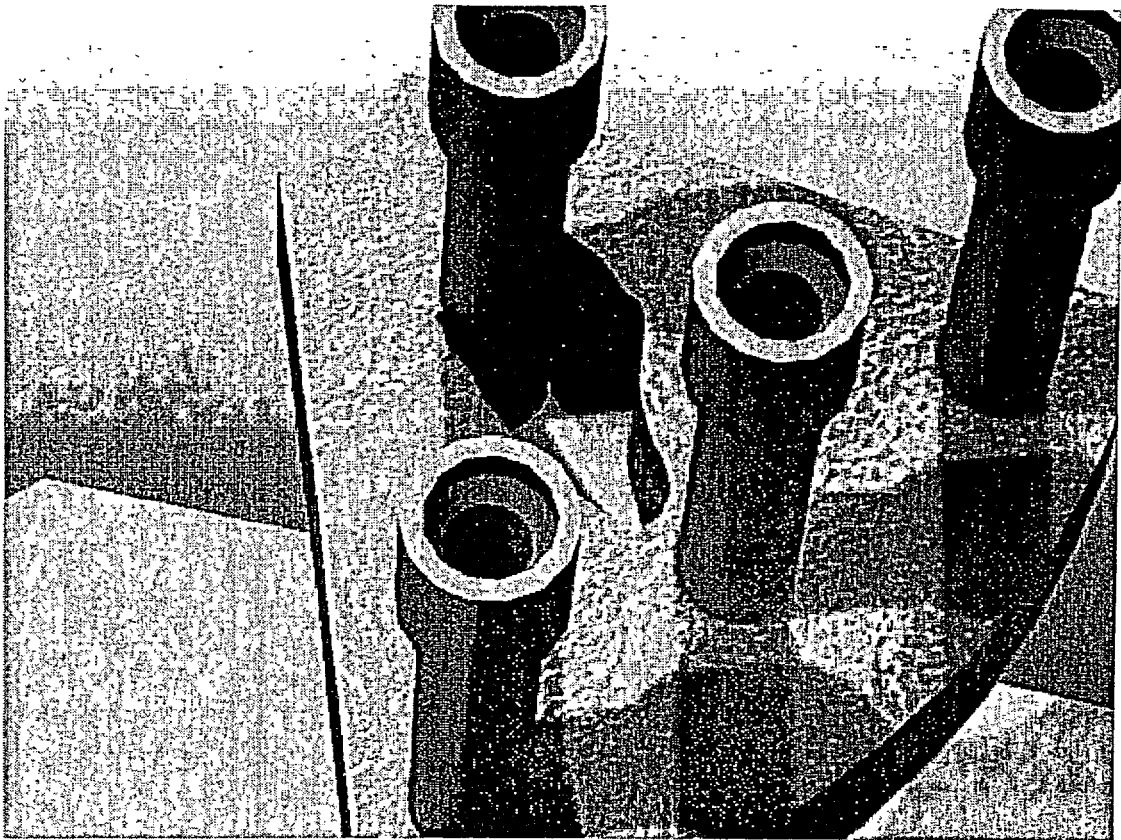
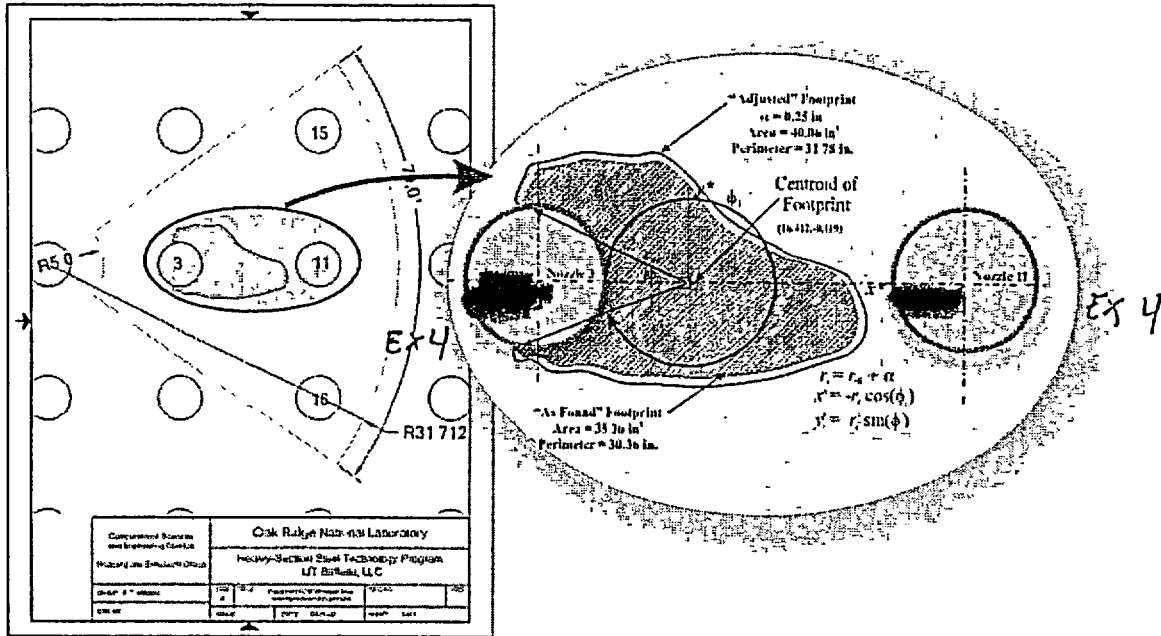


Fig. 8. Geometry of adjusted wastage area footprint. Lower figure is a Photoworks®-rendered image of the submodel with the adjusted “as-found” footprint.

### 3 Postulated Growth Patterns

#### 3.1 Self-Similar Growth Pattern

The *self-similar* growth-pattern scheme attempts to maintain, as closely as practicable, the general shape of the “as-found” cavity footprint. New growth footprints are scaled from a local coordinate system with its origin positioned at the centroid of the “as-found” footprint. A position vector,  $\bar{r}_0$ , tracks the profile of the footprint using the polar coordinates  $(r_i, \phi_i)$  at the 44 points defined in Table 2. At each point along the footprint, the magnitude of the position vector is increased by a constant scaling factor,  $\alpha$ , and then mapped back to the local rectangular Cartesian coordinate system by the following algorithm

$$\begin{aligned} &\text{for } i = 0, 43 \\ & r_{0i} = \sqrt{x_{0i}^2 + y_{0i}^2} \\ & r_i = \alpha \times r_{0i} \\ & x_i = -r_i \cos(\phi_i) \\ & y_i = r_i \sin(\phi_i) \end{aligned} \tag{1}$$

as shown in Fig. 9. This local coordinate system is subsequently mapped to the coordinate system used in the ABAQUS global model and submodels. Figure 10 shows the five growth patterns investigated for  $\alpha = \{1.6, 2.0, 2.8, 3.0, 3.4\}$ . The scaled footprint’s centroid, perimeter, area, and higher moments were calculated with AutoCad 2002 by converting a closed spline to a region and then applying AutoCad’s *Region Mass Properties* utility. These footprint details are given in Table 3. The exposed-cladding surface area ranged from 86 to 276 in<sup>2</sup>. Four of the five growth patterns (as indicated in Fig. 10) intercepted and were constrained by the outer boundaries of the submodel. A second growth-pattern scheme was developed to check the sensitivity of the results to this interaction with the submodel boundaries.

#### 3.2 Ellipsoidal Growth Pattern

In Fig. 11, the *ellipsoidal* growth-pattern scheme established a partially elliptical or ovalized footprint extending between Nozzles 3 and 11. The growth is parameterized by the variable  $\delta$  which serves as the transverse (initially minor) axis footprint extending between the two nozzles. The longitudinal (initially major) axis also varies. The exposed-cladding surface area ranges from 99 to 254 in<sup>2</sup> for the ellipsoidal growth patterns.

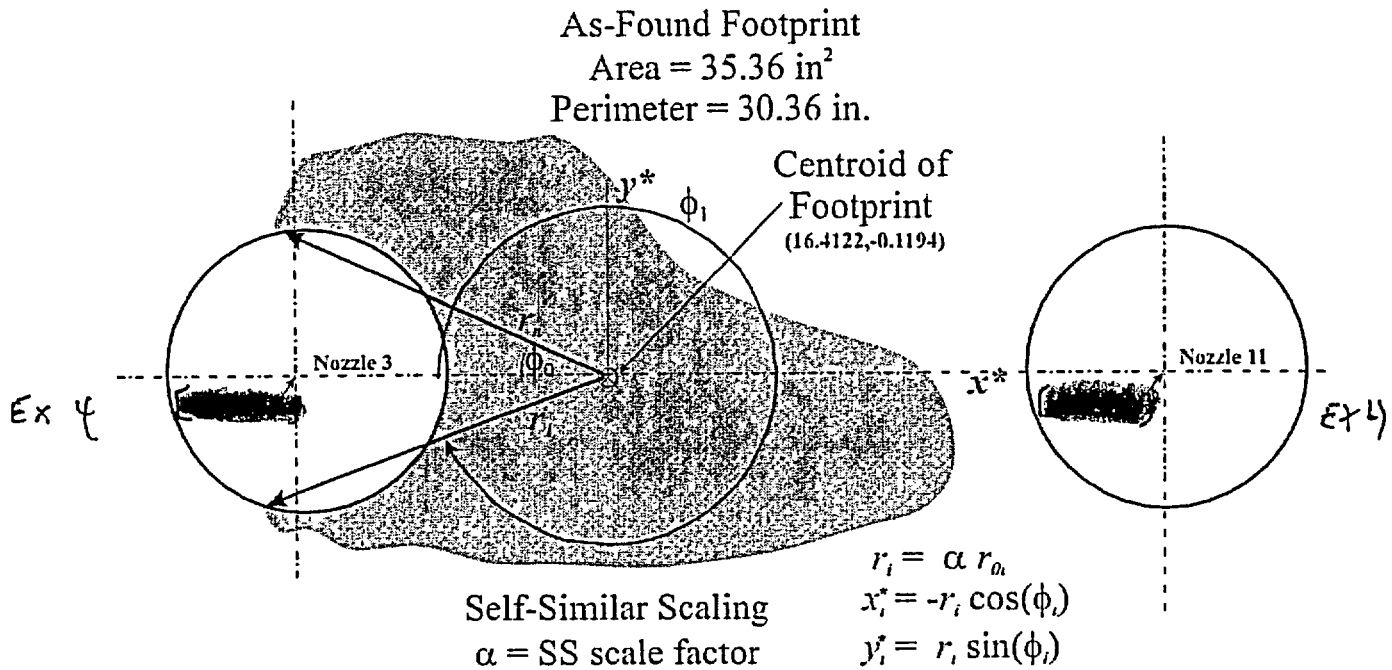


Fig. 9. Local coordinate system employed in *self-similar* growth patterns with scaling of footprint based on scale factor,  $\alpha$ .

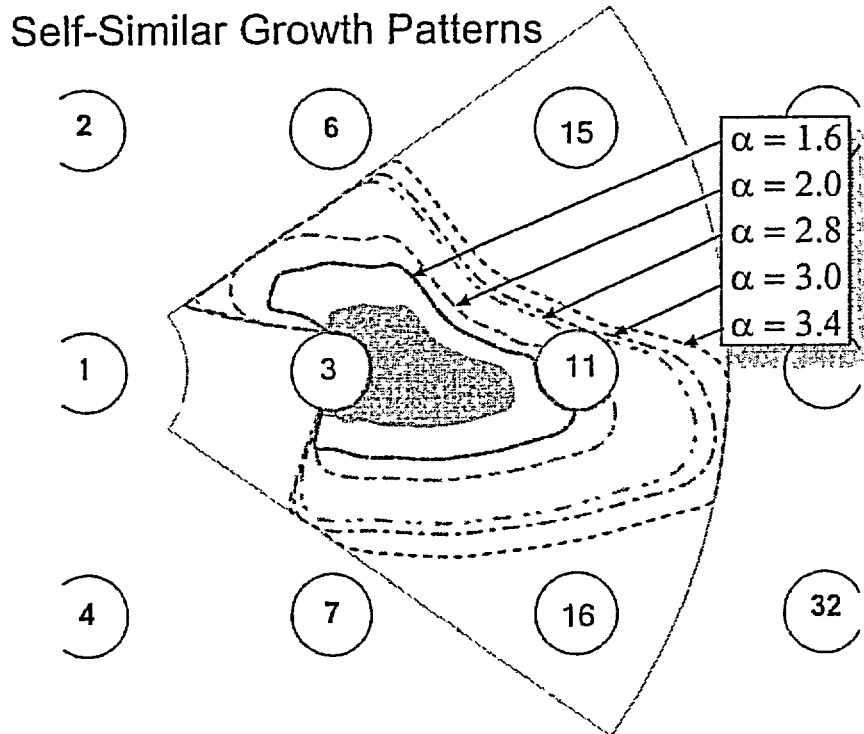


Fig. 10. Expansion of self-similar growth patterns constrained at submodel boundaries.